Crystalline and correlated phases in two-dimensional transition metal dichalcogenides

Thèse N° 9228

Présentée le 22 février 2019

à la Faculté des sciences de base
Chaire de physique numérique de la matière condensée
Programme doctoral en physique

pour l'obtention du grade de Docteur ès Sciences

par

Diego José PASQUIER

Acceptée sur proposition du jury

Prof. F. Mila, président du jury
Prof. O. Yazyev, directeur de thèse
Prof. C. Ederer, rapporteur
Prof. T. Wehling, rapporteur
Prof. L. Forró, rapporteur

2019

ÉCOLE POLYTECHNIQUE
FÉDÉRALE DE LAUSANNE

To my family…

Acknowledgements

Firstly, I would like to thank my thesis supervisor, Prof. Oleg Yazyev, for giving me the opportunity to work in his research group. Oleg had the openmindness of accepting me as a PhD student even though my background was not directly relevant to condensed matter physics or first-principles calculations. Oleg has shown great patience and has granted me with the freedom that I needed. Most of all, Oleg puts great trust in the members of his group for several aspects ranging from research to teaching.

Secondly, I wish to thank to the other members of the group for their help, knowledge and support. I am especially grateful to Dr. Vamshi Katukuri, particularly for his willingness to discuss any topic in physics, irrespective of his personal interests. I would also like to a give special thank to Dr. Quansheng Wu. While Quansheng joined the group near the end of my PhD, he has always been been willing to share his expertise and experience.

I would also like to thank Prof. Andras Kis and his research group for collaboration, all the students of the course Physique Numérique III (and other courses) for their insightful questions, the administrative staff of the institute for their professionalism, and all the members of the Jury of my thesis for their time.

Finally, I would like to thank my family and friends for their love and support, before, during, and after the course of my PhD.

Lausanne, Octobre 2018 D. P

Abstract

This thesis is dedicated to the study of various aspects of the electronic structure of two-dimensional transition metal dichalcogenides (TMDs) of chemical composition MX_2 (where M is a transition metal atom and X= S, Se, Te), using a combination of *ab inito* density-functional methods.

We first address the relative stability of the $1T$ and $1H$ phases of two-dimensional TMDs as a function of the column of the transition metal atom in the periodic table. Using a Wannier-function approach, we calculate crystal field and ligand field parameters for a broad range of members of this family of materials. Taking TaS_2 as an example, we show how the splitting of the d electron states arises from an interplay of electrostatic effects and hybridization with the ligands' s, p and d states. We show that the ligand field alone cannot explain the stabilization of the $1H$ polymorph for d^1 and d^2 TMDs, and that band structure effects are dominant. We present trends of the calculated parameters across the periodic table, and argue that these allow developing simple chemical intuition.

Secondly, we study the occurrence of charge density wave phases and periodic lattice distortion in metallic $1T$ transition metal dichalcogenides. The phonon dispersion and fermiology of representative examples with different d electron counts are studied as a function of doping. Two qualitatively different behaviours are found as a function of the filling of the t_{2g} subshell. We argue that away from half-filling, weak-coupling nesting arguments are a useful starting point for understanding, whereas closer to half-filling a strong-coupling real-space picture is more correct. Using Wannier functions, it is shown that strong metal-metal bonds are formed and that simple bond-counting arguments apply.

Thirdly, the recently synthesized $1T$ phase of $NbSe_2$, in monolayer form, is investigated from first principles. We find that $1T$-$NbSe_2$ is unstable towards the formation of an incommensurate charge density wave phase, whose periodicity can be understood from the Fermi surface topology. We investigate different scenarios for the experimentally observed superlattice and insulating behaviour, and conclude that the star-of-David phase is the most stable commensurate charge density wave phase. We study the electronic properties of the star-of-David phase at various levels of theory and confirm its Mott insulating character, as speculated and in analogy with TaS_2. The Heisenberg exchange couplings are found to be ferromagnetic, which suggests a parallel with the so-called flat-band ferromagnetism in certain multiband Hubbard models.

Finally, we address the possibility of the occurrence of the excitonic insulator phase in single-layer $TiSe_2$. The relative role of electron-electron and electron-phonon interactions in driving the charge density wave in layered and two-dimensional $TiSe_2$ has been disputed and is still unresolved. We calculate the electronic structure and finite-momentum exciton spectrum from hybrid density functional theory. We find that in a certain range of parameters, excitonic effects are strong and the material is close to a pure excitonic insulator instability. A possible necessary condition for the physical realization of a pure excitonic insulator is proposed.

Keywords: two-dimensional materials, transition metal dichalcogenides, first-principles calculations, density functional theory, dynamical mean-field theory, Wannier functions, crystal field, charge density wave, lattice distortion, Mott insulator, ferromagnetism, excitonic insulator

Résumé

Cette thèse est consacrée à l'étude de divers aspects de la structure électronique des dichalcogénures de métaux de transition bidimensionnels (TMDs) de composition chimique MX_2 (où M est un métal de transition et X=S, Se, Te), en utilisant une combinaison de méthodes *ab inito* basés sur la théorie de la fonctionnelle de la densité.

Nous abordons d'abord la stabilité relative des phases $1T$ et $1H$ des TMDs bidimensionnels en fonction de la colonne de l'atome de métal de transition dans le tableau périodique. En utilisant une approche à fonction de Wannier, nous calculons les paramètres du champ cristallin et du champ de ligands pour un large éventail de membres de cette famille de matériaux. En prenant TaS_2 comme exemple, nous montrons comment la division des états électroniques de charactère d résulte d'un jeu d'effets électrostatiques et d'hybridation avec les états s, p et d des ligands. Nous montrons que le champ de ligands ne peut à lui seul expliquer la stabilisation du polymorphe $1H$ pour les matériaux d^1 et d^2, et que les effets de structure de bande sont dominants. Nous présentons les tendances des paramètres calculés à travers le tableau périodique et montrons que ceux-ci permettent de développer une intuition chimique simple.

Deuxim̀ement, nous étudions la survenue de phases d'ondes de densité de charge et de distorsion périodique du réseau dans les dichalcogénures de métaux de transition $1T$. La dispersion des phonons et la fermiologie d'exemples représentatifs avec différents nombres d'électrons d sont étudiées en fonction du dopage. Nous trouvons deux comportements qualitativement différents en fonction du remplissage de la sous-couche t_{2g}. Nous soutenons donc que, lorsque le remplissage de la sous-couche est loin de la moitié, les arguments de couplage faible de nesting de la surface de Fermi sont un point de départ utile pour la compréhension. En revanche, lorsque le remplissage est plus proche de la moitié, il est plus correct d'utilisé une image dans l'espace réel à fort couplage. En utilisant les fonctions de Wannier, il est montré que des liaisons métal-métal fortes sont formées et que de simples arguments de comptage des liaisons sont applicables.

Troisièmement, la phase $1T$ récemment synthétisée de $NbSe_2$, sous forme monocouche, est étudiée à partir des principes premiers. Nous trouvons que $1T$-$NbSe_2$ est instable face à la formation d'une phase d'onde de densité de charge incommensurable, dont la périodicité peut être comprise à partir de la topologie de la surface de Fermi. Nous étudions différents scénarios pour le charactère isolant et le super réseau observés expérimentalement. Nous concluons que la phase étoile de David est la phase d'onde de densité de charge commensurable la plus stable. Nous étudions les propriétés électroniques de la phase étoile de David à différents niveaux de théorie et confirmons son caractère isolant de Mott, tel que spéculé et analogue avec TaS_2. Les

paramètres de couplage d'échange de Heisenberg se révèlent ferromagnétiques, ce qui suggère un parallèle avec le ferromagnétisme dit à bande plate dans certains modèles de Hubbard multibandes.
Enfin, nous examinons la possibilité de la réalisation de la phase d'isolant excitonique dans le $TiSe_2$ bidimensionnel. Le rôle relatif des interactions électron-électron et électron-phonon dans le mécanisme responsable de l'onde de densité de charge dans le $TiSe_2$ en couches et en deux dimensions a été débatu et n'a toujours pas été résolu. Nous calculons la structure électronique et le spectre des excitons quantité de mouvement finie á partir de la théorie de la densité fonctionnelle hybride. Nous trouvons que dans une certaine gamme de paramètres, les effets excitoniques sont forts et que le matériau est proche de la pure instabilité d'un isolant excitonique. Une condition nécessaire possible pour la réalisation physique d'un isolant excitonique pur est proposée.

Mots-clés : matériaux bidimensionnels, dichalcogénures de métaux de transition, calculs à partir de principes premiers, théorie de fonctionnelle de la densité, théorie du champ moyen dynamique, fonctions de Wannier, champ cristallin, onde de densité de charge, distorsion du réseau, isolant de Mott, ferromagnétisme, isolant excitonique

Contents

Acknowledgements **v**

Abstract (English/French) **vii**

List of figures **xii**

List of tables **xv**

1 Introduction **1**

1.1 2D transition metal dichalcogenides 1

1.2 The Peierls instability 3

1.3 Outline 5

2 Methodology **7**

2.1 Density functional theory 7

2.2 Density-functional perturbation theory 14

2.3 Dynamical mean-field theory 16

2.4 Quasiparticle and excitonic effects 19

3 Crystal field effects in two-dimensional transition metal dichalcogenides **23**

3.1 Introduction 24

3.2 Methodology 26

3.2.1 Wannierization and crystal field parameters 26

3.2.2 Computational details 28

3.3 The case of TaS_2 29

3.3.1 spd, pd, and d models 29

3.3.2 Semi-core and high-energy states 37

3.3.3 Spin-orbit coupling 38

3.4 Crystal field and the relative stability of the $1T$ and $1H$ phases 39

3.5 Trends accross the periodic table 44

3.6 Relation to previous work 47

3.7 Conclusion 48

3.8 Appendix 49

3.8.1 Higher-energy bands of $1T$-TaS_2 49

3.8.2 Band structures of the considered materials 50

4 A unified picture for lattice instabilities in metallic octahedral transition metal dichalcogenides 57

4.1 Appendix 65
  4.1.1 Computational methodology 65
  4.1.2 Wannier functions for $1T'$-WS_2 65
  4.1.3 Wannier functions for $1T''$-ReS_2 66
  4.1.4 Fermi surface for $1T$-WS_2 67

5 Charge density wave phase, Mottness, and ferromagnetism in two-dimensional $1T$-$NbSe_2$ 69

5.1 Introduction 70
5.2 Computational methodology 71
5.3 Charge-density-wave phases 72
5.4 Mottness in the Star-of-David phase 74
5.5 Magnetic phases 77
5.6 Conclusions 79
5.7 Appendix 79
  5.7.1 Assessment of the effect of spin-orbit coupling 79
  5.7.2 Investigation of the 4 × 4 CCDW phase 80
  5.7.3 Type II Wannier functions 80

6 Excitonic effects in two-dimensional $TiSe_2$ from hybrid density functional theory 83

6.1 Computational details 91

7 After-thoughts, conclusions, and outlook 93

Bibliography 112

Curriculum Vitae 113

List of Figures

1.1 Periodic table summarizing the properties of transition metal dichalcogenides . 2

3.1 Ball-and-stick representation of the $1T$ and $1H$ phases of two-dimensional TaS_2. . 27
3.2 Band structure and projected density of states of two-dimensional TaS_2. 30
3.3 Isovalue plots of the d-like Wannier functions for two-dimensional $1T$-TaS_2. 31
3.4 Isovalue plots of the d-like Wannier functions for two-dimensional $1H$-TaS_2. . . . 31
3.5 Aligned crystal field and ligand field energy diagrams of two-dimensional $1T-$ and $1H$-TaS_2. 32
3.6 Band structure of monolayer $1T$-TaS_2 with orbital weight of the Wannier functions. 35
3.7 Band structure of monolayer $1H$-TaS_2 with orbital weight of the Wannier functions. 36
3.8 Aligned ligand field energy diagrams of $1T$- and $1H$-TaS_2, including the spin-orbit coupling. 38
3.9 Calculated total energy difference, per formula unit, between the $1T$ and $1H$ phases of $4d$ and $5d$ disulfides, as a function of the formal number of d electrons. 39
3.10 Modified ligand field energy diagrams of two-dimensional TaS_2, including interorbital hybridization. Plot of the hybridized d'_{z^2} Wannier function of $1H$-TaS_2. . . . 42
3.11 Band structure of two-dimensional HfS_2, ReS_2, and PtS_2 in both the $1T$ and $1H$ phases. 43
3.12 Evolution of the calculated ligand field parameters as a function of the column, in the periodic table, of the transition metal for $4d$ and $5d$ disulfides in the $1T$ and $1H$ phases. 44
3.13 Evolution of the calculated lattice constant as a function of the column, in the periodic table, of the transition metal for $4d$ and $5d$ disulfides in the $1T$ and $1H$ phases. 46
3.14 Evolution of the calculated ligand field parameters as a function of the row, in the periodic table, of the transition metal for $1T$ and $1H$ d^1 disulfides. Evolution of the calculated ligand field parameters as a function of the chalcogen atom (X =S, Se, Te) for $1T$ and $1H$ TaX_2. 47
3.15 Bands for the 27-band $spddsp$ model of monolayer $1T$-TaS_2 with the orbital weight of the d Wannier functions as a color code. 50
3.16 Band structure calculated from first principles for monolayers of ZrS_2, NbS_2, and MoS_2, in the $1T$ and $1H$ phases. 51

3.17 Band structure calculated from first principles for monolayers of TcS_2, RuS_2, and RhS_2, in the $1T$ and $1H$ phases. 52
3.18 Band structure calculated from first principles for monolayers of PdS_2 in the $1T$ and $1H$ phases. 52
3.19 Band structure calculated from first principles for monolayers of WS_2, OsS_2, and IrS_2, in the $1T$ and $1H$ phases. 53
3.20 Band structure calculated from first principles for monolayers of VS_2, NbS_2, and TaS_2, in the $1T$ and $1H$ phases. 54
3.21 Band structure calculated from first principles for monolayers of TaS_2, $TaSe_2$, and $TaTe_2$, in the $1T$ and $1H$ phases. 55

4.1 Electronic structure, doping-dependent bare susceptibility, and doping-dependent phonon softening calculated from first principles for monolayers of $1T$-TaS_2, $1T$-WS_2 and $1T$-ReS_2. 59
4.2 Fermi surface of monolayer $1T$-TaS_2 for the undoped and doped cases. 60
4.3 Ball-and-stick representation of the $1T'$ phases of monolayer WS_2. Isovalue plot of a bonding t_{2g} Wannier function. Aligned ligand field and modified ligand field energy diagrams of the $1T$ and $1T'$ phases of monolayer WS_2. Band structure of monolayer $1T'$-WS_2 with orbital weight of bonding and antibonding t_{2g} Wannier functions. 61
4.4 Ball-and-stick representation of the $1T''$ phases of monolayer ReS_2. Isovalue plot of a bonding t_{2g} Wannier function. Aligned ligand field and modified ligand field energy diagrams of the $1T$ and $1T''$ phases of monolayer ReS_2. Band structure of monolayer $1T''$-ReS_2 with orbital weight of bonding and antibonding t_{2g} Wannier functions. 62
4.5 Isovalue plots of nonbonding t_{2g}, antibonding t_{2g}, and e_g Wannier functions for monolayer $1T'$-WS_2. 66
4.6 Isovalue plots of bonding t_{2g}, antibonding t_{2g}, and e_g Wannier functions for monolayer $1T''$-ReS_2. 67
4.7 Fermi surface of monolayer $1T$-WS_2 for the undoped and doped cases. 67

5.1 Band structure and Fermi surface of monolayer $1T$-$NbSe_2$ calculated from first principles. Ball-and-stick representation of the undistorted $1T$ phases. Isovalue plot of one of the three equivalent t_{2g} Wannier functions. 73
5.2 Phonon dispersion and bare susceptibility of monolayer $1T$-$NbSe_2$ calculated from first principles. 74
5.3 Electronic structure of monolayer $NbSe_2$ in the star-of-David phase at the GGA and GGA+U level. 74
5.4 Ball-and-stick representation of the star-of-David phase of monolayer $NbSe_2$. Simplified 3-band model for monolayer $NbSe_2$ in the star-of-David phase. Isovalue plot of the correlated type I Wannier functions. Spectra calculated from DMFT for different values of U. 76

5.5 Spin polarization density of monolayer $\mathrm{NbSe_2}$ in the star-of-David phase with ferromagnetic ordering. 78
5.6 Effect of the spin-orbit coupling on the electronic structure of monolayer $1T$-$\mathrm{NbSe_2}$. 80
5.7 Effect of the spin-orbit coupling on the electronic structure of monolayer $\mathrm{NbSe_2}$ in the star-of-David phase. 81
5.8 Ball-and-stick representation and electronic structure of the 4×4 CCDW phase of monolayer $1T$-$\mathrm{NbSe_2}$. 82
5.9 Isovalue plot of the uncorrelated type II Wannier functions of monolayer $\mathrm{NbSe_2}$ in the star-of-David phase. 82

6.1 Atomic structure, GGA electronic structure, Fermi surface, and phonon dispersion of monolayer $1T$-$\mathrm{TiSe_2}$. 86
6.2 Quasiparticle band structure of monolayer $1T$-$\mathrm{TiSe_2}$ calculated from hybrid density functional theory. Comparison with ARPES. 87
6.3 Calculated quasiparticle indirect bandgap and exciton binding energy as a function of the mixing parameter of hybrid DFT for monolayer $\mathrm{TiSe_2}$. Exciton band structure along the $\Gamma - M$ direction. 88

List of Tables

3.1 Calculated structural parameters for the undistorted $1T$ and $1H$ phases of TaS_2. . . 30
3.2 Summary of the different models of $1T$- and $1H$-TaS_2. 33

5.1 Calculated Heisenberg exchange couplings of monolayer $NbSe_2$ in the star-of-David phase. 77

1 Introduction

1.1 2D transition metal dichalcogenides

Layered materials have been the subject of significant interest due to the high anisotropy of their properties, rendering them quasi-two-dimensional. Graphene, first exfoliated by Geim and Novoselov using the Scotch tape method, is the first example of a truly two-dimensional crystal [1]. Graphene is a fascinating and intensely-studied material. It consists of an hexagonal lattice of carbon atoms robustly bound together by covalent sigma bonds [2], making it one of the most stable materials known. However, its applications in electronic devices are limited due to the absence of a sizeable bandgap, motivating the study of other families of 2D materials beyond graphene. A multitude of other two-dimensional materials have been synthesized or have been predicted to exist [1, 3, 4, 5]. Among them, the arguably most important family of two-dimensional materials is that of the transition metal dichalcogenides (TMDs) [6].

The family of transition metal dichalcogenides is particularly interesting because of the rich variety of the properties of its materials, as summarized in Fig. 1.1 [1]. Two-dimensional TMDs of chemical MX_2 consist of a triangular lattice of a transition metal M, sandwiched between two layers of chalcogen atoms (X=S, Se, Te). The transition metal ion can have either broken octahedral or trigonal prismatic coordination, leading to two polymorphs referred to as $1T$ and $1H$, respectively. The structural and electronic properties of these two phases will be discussed in details in Chapter 3.

Let us now make a few observations based on the inspection of the periodic table of transition metal dichalcogenides (Fig. 1.1), which will motivate the different research projects undertaken in this thesis and presented in the following chapters. The first observation is that the trigonal prismatic phase is realized for group V and group VI TMDs. Group V and group VI TMDs are characterized by a formal electronic configuration of the transition metal ion of d^1 and d^2, respectively. The stabilization of the trigonal prismatic phase for d^1 and d^2 TMDs is often been explained in terms of ligand field arguments [7]. This observation has led to the first project

---

[1] In this thesis, we will restrict ourselves to the materials adopting either the $1T$ or $1H$ crystalline phases (or derived from the latter). We shall not consider materials with unrelated structures as members of the family.

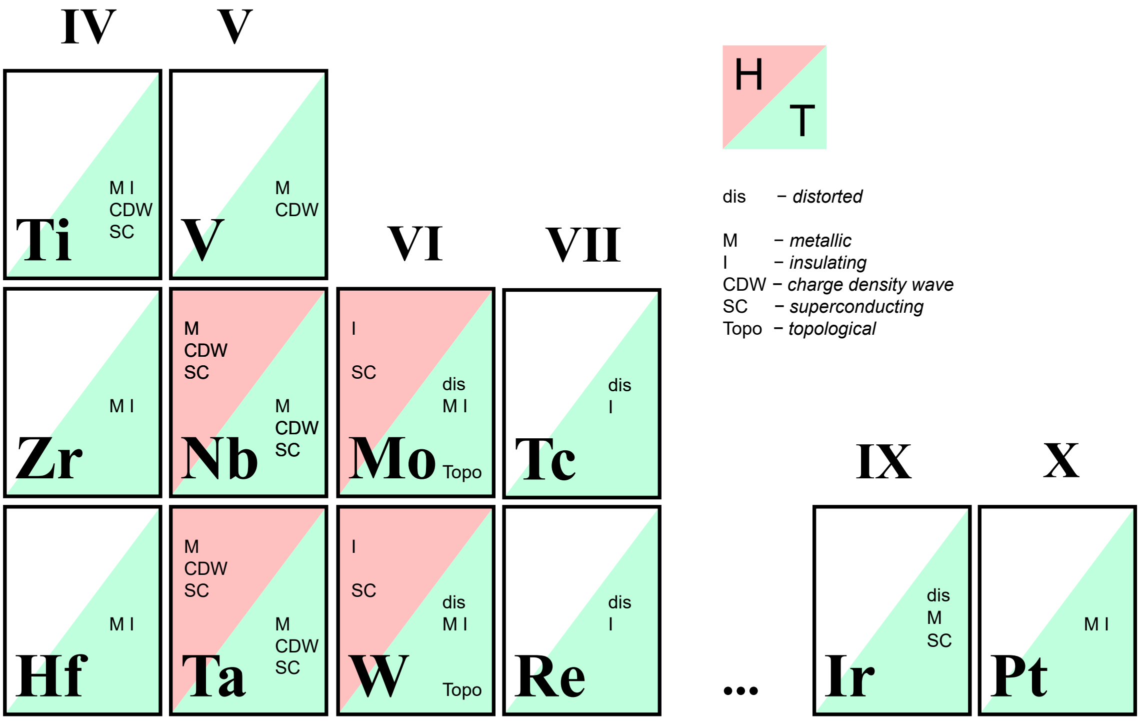
IV
V
VI
VII
IX
X
H
T
dis – distorted
M – metallic
I – insulating
CDW – charge density wave
SC – superconducting
Topo – topological
Ti
M I
CDW
SC
V
M
CDW
Zr
M I
Nb
M
CDW
SC
M
CDW
SC
Mo
I
SC
dis
M I
Topo
Tc
dis
I
Hf
M I
Ta
M
CDW
SC
M
CDW
SC
W
I
SC
dis
M I
Topo
Re
dis
I
...
Ir
dis
M
SC
Pt
M I

Figure 1.1 – Periodic table summarizing the experimentally observed crystalline and electronic phases of layered and two-dimensional transition metal dichalcogenides. The T symbol corresponds to the octahedral coordination, while the H symbol denotes the trigonal prismatic one. Adapted from Ref. [6].

of this thesis presented in Chapter 3, where we show a systematic study of crystal and ligand field parameters from *ab initio* density functional calculations, for a broad range of materials, in order to assess the validity of this argument. Before proceeding further, let us point out certain interesting properties of the trigonal prismatic TMDs. In the metallic case (i.e. group V TMDs or doped group VI TMDs), most of these materials are superconducting. Incidentally, $1H$-NbSe$_2$ was one of the first materials where truly 2D superconductivity was observed [8]. On the other hand, undoped group VI TMDs such as $1H$-MoS$_2$ are semiconducting, rendering them good candidates for integration of 2D materials in electronic devices [9]. Another interesting aspect of trigonal prismatic TMDs is that in the single-layer limit, inversion symmetry is absent. Combined with the strong spin-orbit coupling experienced by these materials, due to the heavy transition metal ions, this leads to giant spin-orbit-induced spin splitting of the bands [10]. This giant splitting has appealing consequences, such as the so-called Ising superconductivity [11] or the possibility to engineer spin polarization in nanoscale devices [12].

Another observation is the recurrence of various forms of lattice instabilities in metallic TMDs. In group V TMDs, almost all the materials, and for both polymorphs, experience a weak to moderate periodic lattice distortion at low temperature. Originally, it was assumed that these materials realize the Peierls instability in two dimensions [13], so the distortions are commonly referred to as charge density wave (CDW) transitions. For group VI and group VII TMDs, the ideal undistorted $1T$ polymoph is metallic and highly unstable with respect to a strong lattice distortion, leading to the so-called $1T'$ phase with 2 × 1 periodicity and $1T''$ phase with 2 × 2 periodicity for group VI and group VII TMDs, respectively [14]. Because of the controversy regarding the actual role of nesting in group V TMDs, and because of the several different proposal to explain the distortions in group VI and group VII TMDs, we have taken a new look at this problem, which will be presented in Chapter 4. The periodic lattice distortions in $1T$ TMDs have several interesting collateral consequences. The most intensely-discussed consequence concerns the topological properties of the group VI TMDs in the $1T'$ phase [15]. Another known consequence is the emergence of a correlated phase in the CDW phase of bulk TaS_2, with intriguing magnetic properties [16]. The possibility of a similar correlated phase in the recently-synthesized monolayer $1T$-$NbSe_2$ [17] will be the topic of study presented in Chapter 5.

The last observation we would like to make concerns group IV TMDs, characterized by a formal electronic configuration of the transition metal ion of d^0. These materials are either semimetallic or semiconducting, depending on whether the top of the chalcogen's p-like bands and the bottom of the transition metal's d-like bands overlap in energy or not. As one can see in Fig. 1.1, CDW instabilities are not universal for group IV TMDs. Indeed, $TiSe_2$ is the only known group IV TMD that experiences a CDW transition in bulk form [18]. Very recently, it was found that $TiTe_2$ in the single-layer limit also experiences such transition [19]. This suggests that the observed CDW transitions in these materials necessitate some fine-tuning of the electronic structure and interactions. Moreover, simple semilocal functionals fail qualitatively for several of the materials in this group, suggesting that electron-electron interactions play an important role. These considerations have led to the last part of this thesis, presented in Chapter 6, where we address the old conjecture [18] of the possible realization of an excitonic phase [20, 21] in $TiSe_2$.

1.2 The Peierls instability

One of the central concepts in this thesis is that of Peierls instability, so we shall succinctly review it in the following. An intriguing result due to Peierls is that a metallic system of noninteracting electrons in one space dimension is unstable with respect to a small periodic distortion of the underlying lattice, of periodicity $2k_F$, where k_F is the Fermi momentum. The original argument of Peierls can be found in Ref. [22], and has been reproduced in many references. Therefore, it is of little interest to repeat it here, so we shall instead follow a slightly different version of the argument due to Wilczek [23], which highlights an elegant analogy between the Peierls instability and the Coleman-Weinberg mechanism [24] in relativistic quantum field theory.

Let us consider a one-dimensional chain of atoms with one orbital per site, occupied by one electron. Assuming nearest-neighbour hopping only, the noninteracting one-electron dispersion is given by

$$\epsilon(k) = 2t\cos(ka) , \qquad (1.1)$$

where t is the nearest-neighbour hopping parameter, a is the spacing between nearest-neighbour atoms, and k is a pseudomentum. If each atom contributes one electron, the Fermi momentum is given by

$$k_F = \frac{\pi}{2a} \,. \tag{1.2}$$

If one is interested in the physics at energy $E \ll t$, one can linearize the dispersion around the two Fermi points $\pm k_F$, yielding two Weyl fermions (one right-moving and one left-moving) with dispersions $\epsilon(k \pm k_F) = \pm v_F(k - k_F)$. The two Weyl fermions $\psi_{R/L}$ thus obey the equations (in units where $v_F = 1$) :

$$\left(\frac{\partial}{\partial t} - \frac{\partial}{\partial x}\right)\psi_R = 0 \tag{1.3}$$

and

$$\left(\frac{\partial}{\partial t} + \frac{\partial}{\partial x}\right)\psi_L = 0 \,. \tag{1.4}$$

Defining the Dirac fermion $\psi \equiv (\psi_R, \psi_L)^T$ and the Dirac matrices $\gamma = (\sigma_2, i\sigma_1)^T$, we obtain the Dirac equation in 1+1 dimensions:

$$i\gamma \cdot \psi = 0 \,. \tag{1.5}$$

Let us now assume that the direct Coulomb interaction between electrons can be neglected, and that the electrons interact weakly with a displacement field ϕ of momentum π/a (phonon).

With these assumptions, we are left with the following effective Lagrangian for electrons

$$\mathscr{L}_{el} = \bar{\psi}(i\gamma \cdot \psi - g\phi)\psi \,, \tag{1.6}$$

where g is the electron-phonon coupling. The problem is now mapped to that of relativistic quantum field theory in 1+1 dimension, so one can make use of all the machinery of Feynman diagrams to analyse it. Let us consider the effective potential for the classical field $\phi_{cl} \equiv < \phi >$. At one-loop, the most singular contribution is proportional to

$$V^{(1)}_{eff}(\phi_{cl}) \propto \int^{\Lambda} \mathrm{d}^2 k \frac{Tr(\gamma \cdot k)^2}{(k^2 + g^2\phi_{cl}^2)^2} \propto g^2\phi_{cl}^2 \log\left(\frac{\Lambda^2}{g^2\phi_{cl}^2}\right) \,, \tag{1.7}$$

where Λ is an ultraviolet cutoff, introduced because the linearization of the electronic dispersion is only valid for energies $E << t$. The one-loop contribution should be compared to the Hook's law contribution, which is proportional to ϕ^2_{cl}. Because of the logarithmic term in the one-loop contribution, the minimum of the effective potential will always be for $\phi_{cl} \neq 0$, since at small ϕ_{cl} the logarithm diverges. Therefore, no matter how small the electron-lattice interaction g is, the system will spontaneously break the translational symmetry. In the language of solid-physics, one says that the breaking of the symmetry opens a gap at the Fermi level, so that the energy of the occupied state is decreased, while that of the unoccupied state is increased. In the language of relativistic quantum field theory, one speaks instead of mass generation ($m^2 = g^2\phi^2_{cl}$) by radiative corrections [23], as first discussed by Coleman and Weinberg [24].

The argument does not depend on the exact form of the electronic dispersion relation, nor on the Fermi momentum k_F. However, it depends crucially on the dimensionality. Indeed, the Peierls argument implies that in one dimension, a phonon mode at $2k_F$ should soften for any non-zero value of the electron-phonon coupling, because the Fermi surface consists of the two Fermi points and is therefore perfectly nested. In higher dimension, as derived by Chan and Heine [25], a soft phonon mode requires either some fine-tuned nested Fermi surface, and/or a strong electron-phonon coupling. In Chapter 4 and 5, we shall argue that the lattice distortions in d^1 $1T$ TMDs share some features of a $2k_F$ effect similar to the one-dimensional Peierls model described above. On the other hand, we shall also show that for d^2 and d^3 TMDs in the $1T$ phase, this is not the case.

1.3 Outline

The remainder of this thesis is organized as follows. In Chapter 2, we briefly review the different formalisms and computational methods adopted throughout this thesis. Chapter 3 is a pre-print version of an article devoted to the study of crystal field and ligand field effects in the $1T$ and $1H$ phases of transition metal dichalcogenides. In particular, the relevance of crystal field arguments to explain the stabilization of the $1H$ polymorph in d^1 and d^2 TMDs is discussed. Chapter 4 is a pre-print version of a letter, where we address the problem of lattice instabilities in metallic $1T$ TMDs. The relevance of nesting and bonding arguments is discussed. Chapter 5 is post-print version of an article dedicated to the study of the newly-synthesized $1T$ phase of $NbSe_2$ from first principles. The charge density wave instability, structural properties, correlation effects and magnetism are discussed. Chapter 6 is a pre-print version of an article where excitonic effects in two-dimensional $TiSe_2$ are estimated from hybrid density functional theory. The consequences of the results regarding a possible excitonic phase in this material are discussed. Chapter 7 offers a summary of the developments achieved in this thesis, as well as possible further developments and speculations.

2 Methodology

In this chapter, we succinctly introduce several aspects of the theory underlying the methodology adopted in this thesis. We first introduce the Hohenberg-Kohn theorem and the Kohn-Sham formulation of density functional theory. We discuss the local-density approximation (LDA) and its improvements, i.e. the inclusion of gradient corrections (GGA), the LDA+U method, and hybrid functionals. A survey of the use of density-functional perturbation theory for calculating vibrational properties of solids from first principles is provided. We briefly review the basics of dynamical mean-field theory (DMFT). Finally, we introduce the calculation of quasiparticle and excitonic effects in semiconductors and insulators, and how hybrid DFT provides an *estimate* of these effects.

2.1 Density functional theory

Using the Born-Oppenheimer approximation in which ions are treated as fixed classical particles, solid-state physics deals with the issue of solving the N-electron Schrödinger equation with $N \sim 10^{23}$ for an extended solid. Solving directly the Schrödinger for the many-body wave function $\psi(r_1, \cdots, r_N)$ would require to much computational resources, hence one must find clever approximations. The main approach to this problem is to consider a collection of weakly interacting dressed electrons. The original strong interactions between the electrons are absorbed in the definition of the dressed electrons. One can therefore, as a first approximation, consider the dressed electrons as independent, communicating uniquely via the Pauli exclusion principle.

Another approach is to view the interacting electron gas problem as that of a classical liquid, with the electron density $n(r)$ as the fundamental quantity [26]. Arguably the most important result in this representation is due to Hohenberg and Kohn [26], and has led to the development of density functional theory. Condider a system of interacting electrons in an external potential $v(r)$, usually resulting from the electron-ion interaction. The Hohenberg-Kohn (HK) theorem states that

1. The external potential $v(r)$ is a unique functional of the ground state density of the electronic system $n_0(r)$. In other worlds, if $v'(r)$ yields the same ground state density $n_0(r)$, then $v(r)$ and $v'(r)$ must be equal up to a constant term, i.e. $v(r) - v'(r) = \text{const}$.
2. There exists a universal functional of the electron density $F[n(r)]$, independent of the external potential $v(r)$, such that the density $n_0(r)$ of the ground state corresponds to the minimum of the functional $E_v[n(r)] = F[n(r)] + \int \mathrm{d}r\, v(r) n(r)$, under the constraint that $\int \mathrm{d}r\, n(r) = N$.

The HK theorem suggests that, if a good approximation to the universal functional $F[n(r)]$ is known, and if it is not computationally too demanding to evaluate, the problem of finding the ground state of an interacting electron gas is greatly simplified. Indeed, one needs only keeping track of the classical variable $n(r)$ and not of the many-body wave function. Hohenberg and Kohn originally considered two limiting cases, i.e. that of a nearly-uniform gas and that of a slowly-varying gas, for which simple expressions for F can be found.

The Kohn-Sham ansatz

In order to develop useful approximations for the universal functional, Kohn and Sham [27] suggested to introduce an auxiliary system of independent particles, described by the single-particle orbitals $\psi_i(r)$, that yield the same ground state density as the system considered. Let us write:

$$n(r) = \sum_{i=1}^{N} \psi_i^*(r)\psi_i(r)\,, \tag{2.1}$$

where N is the number of electrons. We can rewrite the universal functional as

$$E_v[n] = \int \mathrm{d}r\, v(r) n(r) + T[n] + E_H[n] + E_{xc}[n]\,, \tag{2.2}$$

where $T[n]$ is the kinetic energy of the auxiliary system of Kohn-Sham orbitals

$$T[n] = -\frac{1}{2}\sum_{i=1}^{N}\int \mathrm{d}r \nabla\psi_i^*(r)\nabla\psi_i(r)\,, \tag{2.3}$$

$E_H[n]$ is the Hartree contribution, given by

$$E_H[n] = \frac{1}{2}\int \mathrm{d}r\mathrm{d}r' \frac{n(r)n(r')}{|r-r'|}\,, \tag{2.4}$$

and $E_{xc}[n]$ is the *exchange-correlation* functional, whose exact form is unknown. The minimum condition of the energy functional therefore yields a set of equations for the Kohn-Sham orbitals:

$$H_{KS}[n]\psi_i(r) = \left(-\frac{1}{2}\nabla^2 + v_{KS}(r)\right)\psi_i(r) = \epsilon_i\psi_i(r)\,, i = 1, \cdots N\,, \tag{2.5}$$

where $v_{KS}(r) = v(r) + v_H(r) + v_{xc}(r)$, with

$$v_H(r) = \int \mathrm{d}r' \frac{n(r')}{|r - r'|} , \tag{2.6}$$

and

$$v_{xc}(r) = \frac{\delta E_{xc}}{\delta n(r)} . \tag{2.7}$$

In practice, Eqs. 2.5 are solved iteratively until self-consistency. One starts with an initial guess for the Kohn-Sham orbitals, derives the corresponding Kohn-Sham Hamiltonian $H_{KS}[n]$, find its N lowest eigenvalues, and compares the corresponding density $n(r)$ obtained with that of the initial guess. The procedure is then iterated until self-consistency is achieved, i.e. until the input and output charge densities are equal.

The local-density approximation

The Kohn-Sham equations resemble closely the Hartree-Fock ones, with the exchange-correlation potential $v_{xc}(r)$ replacing the Fock exchange term. The power of the Kohn-Sham DFT scheme is that all the unknown many-body effects are put in the exchange-correlation potential, and that simple but yet accurate approximations to $v_{xc}(r)$ can be developed.

The crudest approximation would be to simply neglect the exchange-correlation part and to set $v_{xc}(r) = 0$. In that case, one recovers the Hartree approximation. An improvement consists in including including the Fock exchange term, i.e. choosing

$$E_{xc}^{HF} \equiv E_x = -\frac{1}{2} \sum_{i,j=1}^{N} \int \mathrm{d}r\mathrm{d}r' \frac{1}{|r - r'|} \psi_i^*(r)\psi_j^*(r')\psi_j(r)\psi_i(r') . \tag{2.8}$$

The Hartree-Fock approximation does not perform very well for most systems. In solid-state physics, this approximation systematically strongly overestimates the bandgap for insulators, and gives too large bandwidths for metals. Moreover, the evaluation of the Fock exchange term is relatively demanding computationally.

In principle, one could use many-body perturbation theory to include higher order terms in the exchange-correlation term. Another approach, that lies at the heart of the successes of density functional theory, is the so-called *local-density approximation* (LDA). The assumption of the LDA is that the exchange-correlation term takes the form:

$$E_{xc}^{LDA}[n] = \int \mathrm{d}r \epsilon_{xc}^{HOM}(n(r)) , \tag{2.9}$$

where ϵ_{xc}^{HOM} (where HOM stands for homogeneous) is a simple function depending on the local charge density, given by the exchange-correlation energy density of the homogeneous electron gas with the same density. The exchange-correlation density for the homogeneous electron gas is known from precise Monte-Carlo simulations [28]. In solid-state systems, the actual charge density is often far from a homogeneous electron gas. Hence, it is quite surprising that the LDA works rather well for most materials, given the seemingly crude uncontrolled approximations. A generalization of the LDA for magnetic systems is known as the *local spin-density approximation* (LSDA), for which the exchange-correlation term takes the form:

$$E_{xc}^{LSDA}[n_\alpha, n_\beta] = \int \mathrm{d}r \epsilon_{xc}(n_\alpha(r), n_\beta(r)) \,, \tag{2.10}$$

where $\epsilon_{xc}(n_\alpha, n_\beta)$ is a simple function depending on the two spin densities n_α and n_β.

The LDA is the basis of most applications of density functional theory in solid-state physics and chemistry. More sophisticated functionals can be thought of as the local-density approximation with added corrections. The next level of sophistication in the design of functionals consists in including density gradient corrections, i.e. replacing in Eq. 2.9 the function $\epsilon_{xc}^{HOM}(n(r))$ by a more complicated function that depends not only on the local charge density, but also on its gradient. This class of functionals is known as the generalized gradient approximation (GGA) and is characterized by an exchange-correlation energy taking the form

$$E_{xc}^{GGA}[n] = \int \mathrm{d}r f(n, \nabla n) \tag{2.11}$$

where $f(n, \nabla n)$ is a simple function. The most commonly used parametrization of the GGA is due to Perdew, Burke, and Ernzerhof [29], and is referred to as the PBE functional.

Hybrid functionals

An important class of functionals, known as *hybrid functionals,* are built by mixing the LDA and/or GGA functionals with Hartree-Fock exchange. Note that, while for LDA and GGA the exchange-correlation functional depends on the charge density only, the Fock exchange term E_x depends explicitly on the orbitals. Therefore, density functional theory with hybrid functionals belongs to the so-called *generalized Kohn-Sham schemes*[30]. One of the motivations for doing so is to cure the so-called bandgap problem and is based on the following observation. For semiconductors and insulators, Hartree-Fock strongly overestimate the gap, while the LDA and GGA functionals underestimate it, typically by $50-100$ %. Hence, by introducing a parameter that continuously connects the LDA/GGA functionals to Hartree-Fock, one can smoothly interpolate between the underestimation of LDA/GGA and the overestimation of Hartree-Fock. There are several ways to define hybrid functionals.

One simple and popular way to define a hybrid functional is to mix the exchange energy of PBE E_x^{PBE} with that of Hartree-Fock E_x, while keeping the correlation part of PBE E_c^{PBE}, yielding

$$E_{xc}^{PBE0} = \alpha E_x + (1-\alpha) E_x^{PBE} + E_c^{PBE} \,, \tag{2.12}$$

where α is the *mixing parameter* that takes values between 0 and 1. The choice of $\alpha = 1/4$ leads to the PBE0 functional [31, 32].

The PBE0 functional with $\alpha = 1/4$ yields bandgaps in relatively good agreement with experiments for medium-gap systems (~ 2−5 eV). However, for large-gap systems, PBE0 underestimates the gap, while for small-gap systems the gap is overestimated. This can be cured by changing the value of α, using either α as a free parameter or estimating it [33, 34]. Choosing the mixing parameter as the inverse of the dielectric constant $1/\epsilon_\infty$ yields good agreements with experiments for a broad range of systems [33, 34]. The functional defined in Eq. 2.12 with a generic value of α different from 1/4 is sometimes referred to as PBE0(α). In Chapter 6, where we present calculations using hybrid functionals, we shall refer to it simply as PBE0.

Another important subclass of hybrid functionals was introduced by Heyd, Scuseria, and Ernzerhof (HSE) [35]. HSE functionals are built by mixing the PBE exchange with a screened Fock exchange term $E_x(\mu)$

$$E_{xc}^{HSE} = \alpha E_x^{SR}(\mu) + (1-\alpha) E_x^{PBE,SR} + E_x^{PBE,LR} + E_c^{PBE} \,, \tag{2.13}$$

where SR/LR stand for short-range and long-range, and μ is the *range-separation* parameter. The screened short-range exchange term $E_x^{SR}(\mu)$ corresponds to the Fock exchange, defined in Eq. 2.8, evaluated with a Coulomb potential screened by the complementary error function, i.e. by making the replacement

$$\frac{1}{|r|} \to \frac{1}{|r|} \mathrm{erfc}(\mu |r|) \,. \tag{2.14}$$

The choice of parameters $\alpha = 1/4$ and $\mu = 0.3$ Å^{-1} ($\mu = 0.2$ Å^{-1}) yields the so-called HSE03 (HSE06) functionals [35, 36]. Note that PBE0 is a special case of HSE, corresponding to the choice $\mu = 0$. In Chapter 6, we shall use the HSE functional with the range-separation parameter of HSE06 and a variable mixing parameter α. For simplicity, we shall refer to it as HSE06.

The LDA+U method

The LDA+U method was introduced to extend the applicability of density functional theory to Mott insulators [37]. Mott insulators are materials that are predicted to be metallic according to band theory but are insulating because of strong correlations. The LSDA and spin-polarized GGA fail to capture the strong local correlations, associated e.g. with $3d$ electrons in transition metal oxides, and therefore often fail qualitatively for Mott insulators, wrongly predicting them to be metallic.

The LDA+U method is based on the Hubbard model and consists in adding explicitly to the exchange-correlation functional an energy penalty (parametrized by the Hubbard term U) for double occupancy of a chosen set of localized orbitals. The LDA+U functional takes the form

[38]:

$$E_{LDA+U} = E_{LDA}[n(r)] + E_{Hub}[n^{I\sigma}_{mm'}] - E_{DC}[n^{I\sigma}] , \tag{2.15}$$

where E_{Hub} describes interactions between the correlated electrons and E_{DC} is the double-counting energy. The double-counting term corresponds to the part in E_{LDA} that describes the interactions that are to be replaced by E_{Hub}. The Hubbard term depends on the occupancy matrix $n^{I\sigma}_{mm'}$, where I refers to an atomic site, σ is a spin index, and m, m' are state indices. The double-counting term depends only on:

$$n^{I\sigma} = \sum_m n^{I\sigma}_{mm} . \tag{2.16}$$

There are several formulations of the LDA+U method. In Chapter 5, the simplified formulation of Cococcioni and de Gironcoli [39] was used. In this formulation, the Hubbard part of the functional reads:

$$E_U = E_{Hub} - E_{DC} = \frac{U}{2} \sum_{I,i,\sigma} \lambda^{I\sigma}_i (1 - \lambda^{I\sigma}_i) , \tag{2.17}$$

where $\lambda^{I\sigma}_i$ is the occupation of the correlated orbital described by indices i, I, σ and takes values between 0 and 1.

There are several approaches to choose the Hubbard parameter U. One possibility is to treat U as a free parameter and to choose it to obtain agreement with experiments. It is also possible to estimate the U from the underlying LDA calculation. In Chapter 5, we have estimated U for niobium $4d$ electrons in NbSe$_2$ using the linear response approach of Cococcioni and de Gironcoli [39].

Note that the LDA+U method is called in such a way for historical reasons, but nowadays the GGA functional is usually used instead of LDA.

Plane-wave basis set

In order to solve the Kohn-Sham equations for realistic systems on a computer, such as molecules or periodic crystals, one needs to introduce a finite basis set. There are different possibilities for doing so. For periodic systems, a natural choice consists in using a plane-wave basis set. In this thesis, the density functional calculations have been performed using two different codes, Quantum ESPRESSO [40] and VASP [41, 42, 43], both of which use plane waves.

With periodic boundary conditions, one can make use of Bloch's theorem and label the Kohn-Sham orbitals $\psi_{nk}(r)$ with the band index n and pseudomomentum k, and expand it in terms of plane waves:

$$\psi_{nk}(r) = \sum_{G} c_{nk}(G) e^{i(k+G)r} \ , \tag{2.18}$$

where G is a vector of the reciprocal lattice. The Kohn-Sham potential expressed in the reciprocal space as:

$$v_{KS}(G,G') = \frac{1}{\Omega}\int_{u.c} \mathrm{d}r e^{-i(G-G')r} v_{KS}(r) \ , \tag{2.19}$$

where the integral is carried over the unit cell and Ω is its volume. In this basis, the Kohn-Sham equations read:

$$\left(\frac{1}{2}(k+G')^2\delta_{GG'} + v_{KS}(G,G')\right) c_{nk}(G') = \epsilon_{nk} c_{nk}(G) \ . \tag{2.20}$$

One can truncate the expansion in Eq. 2.18, including only G vectors so that the kinetic energy is smaller than a chosen cutoff E_{cut}, i.e.

$$\frac{1}{2}(k+G)^2 < E_{cut} \ . \tag{2.21}$$

One of the advantages of a plane-wave basis set is that one can systematically converge the desired calculated quantities with respect to the basis set by increasing the cutoff until the desired accuracy is reached.

Pseudopotentials

The pseudopotential approximation allows to significantly reduce the basis set size in Eq. 2.20, diminishing the computational cost. The idea of the pseudopotential approximation is that core-electron states are unaffected by the environment of an ion as they do not participate to chemical bonding. Therefore, one can freeze them and mimic their effect on valence electrons by modifying the Coulomb potential of the ion.

There are different types of pseudopotentials used in *ab initio* electronic-structure calculations. Norm-conserving pseudopotentials [44] are the simplest and are obtained by :

- Performing an all-electron calculation on an isolated atom.
- Separating the electronic levels in core and valence levels.
- Imposing that the all-electron wave function and the pseudo wave function of valence states are identical beyond a cutoff radius r_c.
- Imposing that the norms of the all-electron and pseudo wave functions inside the radius r_c are identical.

The last condition can be relaxed for ultrasoft pseudopotentials [45]. Using norm-conserving pseudopotentials, the form of the Kohn-Sham equations (Eq. 2.5) keep the same form. The difference is the appearance of an extra additive a term in the Kohn-Sham potential, i.e. $v_{KS}(r) \rightarrow v_{KS}(r) + v_{ps}(r)$, with $v_{ps}(r)$ being repulsive close to the ions.

2.2 Density-functional perturbation theory

Density functional theory permits the calculation of the ground state total energy and charge density of a given system. Many interesting properties of many-electrons systems are related to the derivatives of the total energy and charge density with respect to some external perturbation, and density-functional perturbation theory (DFPT) is a powerful tool to calculate these from first principles [46].

A good example in solid-state systems is that of phonons, that are related to the second order derivatives of the total energy with respect to the displacement of the atoms. Calculating the phonon properties from first principles is important because it allows, e.g. predicting the thermodynamic stability of a structure and calculating superconducting properties for metallic systems. In this thesis, the calculation of phonon dispersion curves will play a central role in Chapters 4 and 5.

Using the Born-Oppenheimer approximation, the lattice dynamics is governed by the following Schrödinger equation [47]

$$\left(-\frac{1}{2}\sum_I \frac{\partial^2}{\partial R_I^2} + E(R)\right)\Phi(R) = \epsilon\Phi(R)\ , \tag{2.22}$$

where R_I is the position vector of an ion I of mass M_I, $R \equiv (\{R_I\})$, and $E(R)$ is the ground-state energy of a system of interacting electrons in the potential generated by the ions. The Born-Oppenheimer energy surface $E(R)$ can be obtained by finding the ground-state (e.g. using DFT) of the Born-Oppenheimer Hamiltonian

$$H_{BO}(R) = -\frac{1}{2}\sum_i \frac{\partial^2}{\partial r_i^2} + \frac{1}{2}\sum_{i\neq j}\frac{1}{|r_i - r_j|} - \sum_{iI}\frac{Z_I}{|r_i - R_I|} + E_N(R)\ , \tag{2.23}$$

where r_i is the coordinate of electron i, Z_I is the atomic number of the ion I, and $E_N(R)$ is the Coulomb repulsion between the ions:

$$E_N(R) = \frac{1}{2}\sum_{I\neq J}\frac{Z_I Z_J}{|R_I - R_J|}\ . \tag{2.24}$$

The forces acting on the ion I can be obtained by calculating the first derivative of the Born-

Oppenheimer energy $E(R)$, i.e.

$$F_I = -\frac{\partial E(R)}{\partial R_I} \,. \tag{2.25}$$

The forces must all vanish at equilibrium. According to the Hellmann-Feynman theorem, the first derivatives of the eigenvalues of a Hamiltonian that depends on a parameter λ are given by the expectation value of the derivative Hamiltonian

$$\frac{\partial E_\lambda}{\partial \lambda} = \langle \Psi_\lambda | \frac{\partial H_\lambda}{\partial \lambda} | \Psi_\lambda \rangle \,. \tag{2.26}$$

It follows that the forces at configuration R of the nuclei can be obtained from the knowledge of the corresponding ground-state charge density $n_R(r)$

$$F_I(R) = -\frac{\partial E_N(R)}{\partial R_I} - \int \mathrm{d}r \, n_R(r) \frac{\partial V_R(r)}{\partial R_I} \,, \tag{2.27}$$

where $V_R(r)$ is the potential created by the nuclei

$$V_R(r) = \sum_I \frac{Z_I}{|r - R_I|} \,. \tag{2.28}$$

On the other hand, the vibration frequencies ω are obtained from the second derivatives of $E(R)$ according to

$$\det \left| \frac{1}{\sqrt{M_I M_J}} \frac{\partial^2 E(R)}{\partial R_I \partial R_J} - \omega \right| = 0 \,. \tag{2.29}$$

Evaluating the Hessian in Eq. 2.29 requires knowledge of the ground charge density $n_R(r)$ *and* its linear response:

$$\frac{\partial^2 E(R)}{\partial R_I \partial R_J} = \frac{\partial^2 E_N(r)}{\partial R_I \partial R_J} + \int \mathrm{d}r \, n_R(r) \frac{\partial^2 V_R(r)}{\partial R_I \partial R_J} + \int \mathrm{d}r \frac{\partial n_R(r)}{\partial R_I} \frac{\partial V_R(r)}{\partial R_J} \,. \tag{2.30}$$

A possible approach to calculate the Hessian matrix consists in introducing finite displacements δR of the ions, evaluating the Born-Oppenheimer energy $E(R)$ and $E(R+\delta R)$ from DFT, and approximating the derivatives with finite differences methods. In a periodic solid, this approach can be inconvenient as it requires introducing possibly large supercells. A more powerful approach consists in evaluating $n_R(r)$ from DFT and the last term in Eq. 2.30 from first-order perturbation theory.

The variation of the charge density $\Delta n(r)$ can be expressed in terms of the variation of the Kohn-Sham orbitals

$$\Delta n(r) = 2 \sum_{i=1}^{N} \psi_i^*(r) \Delta \psi_i(r) \,, \tag{2.31}$$

with the operator Δ acting as

$$\Delta n(r) = \sum_i \frac{\partial n(r)}{\partial \lambda_i} \Delta \lambda_i \ , \tag{2.32}$$

where $\{\lambda_i\}$ are the parameters of the Born-Oppenheimer Hamiltonian (i.e. the ions' coordinates in the present case). Eq. 2.32 defines the action of the operator Δ on $n(r)$ and can be easily generalized to any quantity that depends on the parameters $\{\lambda_i\}$. The variation of the Kohn-Sham wave functions obey the equation

$$\left(-\frac{1}{2}\frac{\partial^2}{\partial r^2} + v_{KS} - \epsilon_i\right) |\Delta\psi_i\rangle = -\left(\Delta v_{KS} - \Delta\epsilon_i\right) |\psi_i\rangle \ . \tag{2.33}$$

In Eq. 2.33, the variation of the Kohn-Sham potential Δv_{ks} is a functional of the variation of the charge density Δn and can be expressed as

$$\Delta v_{KS}(r) = \Delta v(r) + \int \mathrm{d}r' \frac{\Delta n(r')}{|r-r'|} + \left.\frac{\partial v_{xc}}{\partial n(r)}\right|_{n(r)} \Delta n(r) \ . \tag{2.34}$$

The above-equations (2.31-2.34) are to be solved self-consistently, similarly to the Kohn-Sham equations, and allow calculating the linear response of the electronic charge density with respect to an external perturbation.

2.3 Dynamical mean-field theory

As discussed in Sec. 2.1, the LDA+U method extends the applicability of density functional theory to Mott insulators. In LDA+U, the exchange-correlation functional is inspired by the Hubbard model. The Hubbard model is the canonical model to study strongly correlated electrons on a lattice and is given by, in its one-band form

$$H_{Hub} = \sum_{i,\sigma} \epsilon_{id\sigma} c^\dagger_{id\sigma} c_{id\sigma} + U \sum_i n_{id\uparrow} n_{id\downarrow} + \sum_{ij\sigma} t_{ij} c^\dagger_{id\sigma} c_{jd\sigma} \ , \tag{2.35}$$

where $c^\dagger_{id\sigma}$ is the creation operator of a correlated d electron at lattice site i in spin state σ, U is the on-site repulsion Hubbard parameter, t_{ij} are the hopping terms, $n_{id\uparrow/\downarrow}$ is the occupation operator at site i in up/down spin state, and $\epsilon_{id\sigma}$ are the on-site energies. Despite its simplicity, the one-band Hubbard model is solvable only in special cases. In the LDA+U method, the LDA part of the functional describes the uncorrelated electrons and the kinetic part of the correlated electrons, while the U term models the on-site repulsion of the correlated electrons.

As argued by Anisimov, Zaanen and Andersen in their seminal paper [37], mean-field theory (or Hartree-Fock decoupling) can also be successful when the coupling is strong, especially at half-filling, so that the mean-field treatment in LDA+U makes sense. The mean-field decoupling consists in neglecting the fluctuation of the occupation numbers around their mean values, replacing the second term in Eq. 2.35 by [37]

$$H_U^{HF} = U\sum_i \left(n_i(n_{i\uparrow} + n_{i\downarrow}) - m_i(n_{i\uparrow} + n_{i\downarrow}) - \frac{1}{4}(n_i^2 - m_i^2) \right) , \tag{2.36}$$

where $n_{i\uparrow,\downarrow} = \langle n_{id\uparrow,\downarrow} \rangle$, $n_i = n_{i\uparrow} + n_{i\downarrow}$, and $m_i = n_{i\uparrow} - n_{i\downarrow}$. Therefore, in the limit where the Hubbard U is much larger than the kinetic parameters t_{ij}, the minimum of H_U^{MF} is obtained when the correlated band is fully spin-polarized, with a gap $\sim U$ between the spin-minority and spin-majority bands (or upper and lower Hubbard bands). The mean-field decoupling of Eq. 2.36 works best in limiting cases, i.e. either in the independent-electrons limit (i.e. $U \ll t$) or in the fully localized one (i.e. $U \gg t$ and at half-filling).

The dynamical mean-field theory [140] provides an alternative and more generic route towards solving the Hubbard model. DMFT is more universal and works for both the two limiting cases discussed above *and* for intermediate cases. Moreover, because of the Hartree-Fock decoupling, LDA+U can only describe a Mott insulator in the spin polarized regime. On the other hand, DMFT correctly describes the paramagnetic insulating behaviour of Mott insulators above the magnetic transition temperature.

In DMFT, the Hubbard model is mapped onto an Anderson impurity model on a lattice

$$H_a = \sum_{k\sigma} \epsilon_{k\sigma} c_{k\sigma}^\dagger c_{k\sigma} + \sum_\sigma \epsilon_d d_\sigma^\dagger d_\sigma + U n_{d\uparrow} n_{d\downarrow} + \sum_{k\sigma} V_{k\sigma}(c_{k\sigma}^\dagger d_\sigma + d_\sigma^\dagger c_{k\sigma}) . \tag{2.37}$$

In this equation, the first term describes the lattice electrons (c-electrons, with dispersion ϵ_k), the second and third terms describe the local impurity electron (d-electron), and the last term represents the interaction of the impurity electron with the bath of lattice electrons via the hybridization coupling V. The Anderson impurity model can be solved numerically, e.g. with Quantum Monte Carlo methods, so that the impurity Green's function G_{imp} can be calculated. In imaginary time, the impurity Green's function is defined as

$$G_{imp}(\tau) = -\left\langle T d(\tau) d^\dagger(0) \right\rangle , \tag{2.38}$$

where T is a time-ordering operator. In this expression and from now on, we shall drop the spin index σ. In imaginary frequency space, we have

$$G_{imp}(i\omega_n) = \int_0^\beta \mathrm{d}\tau e^{i\omega_n \tau} G_{imp}(\tau) , \tag{2.39}$$

where β is the inverse temperature. The impurity self-energy Σ_{imp} is defined as

$$\Sigma_{imp}(i\omega_n) = G_{0,imp}^{-1} - G_{imp}(i\omega_n)^{-1} , \tag{2.40}$$

where $G_{0,imp}^{-1}$ is defined as

$$G_{0,imp}^{-1}(i\omega_n) = i\omega_n + \mu + \epsilon_d - \Delta(i\omega_n) , \tag{2.41}$$

where μ is the chemical potential. In this equation, the last term is the dynamical mean-field and is given by the expression

$$\Delta(i\omega_n) = \sum_k \frac{V_k}{i\omega_n - \epsilon_k} \, . \tag{2.42}$$

The lattice Green's function reads

$$G_{lat}(k, i\omega_n) = \frac{1}{i\omega_n - \mu - \epsilon_k - \Sigma_{lat}(k, i\omega_n)} \, . \tag{2.43}$$

The approximation of DMFT consists in equalizing the lattice self-energy to that of the impurity, i.e. $\Sigma_{lat}(k, i\omega_n) = \Sigma_{imp}(i\omega_n)$. The equations of DMFT are to be solved self-consistently. The condition for self-consistency is that the Green's function of the impurity is the same as the local lattice Green's function. The latter is defined as

$$G_{lat,loc}(i\omega_n) = \sum_k \frac{1}{i\omega_n - \mu - \epsilon_k - \Sigma_{imp}(i\omega_n)} \, . \tag{2.44}$$

One then proceeds as usual for solving self-consistently a set of equations. One makes an initial guess for the self-energy, from which the local lattice Green's function $G_{lat,loc}$ is calculated. From $G_{lat,loc}$, one can extract the mean field Δ as

$$\Delta(i\omega_n) = i\omega_n + \mu - G^{-1}_{lat,loc}(i\omega_n) - \Sigma_{imp}(i\omega_n) \, . \tag{2.45}$$

The corresponding Anderson impurity problem is then solved, and the new self-energy is compared with the guessed self-energy. The procedure is iterated until the input and output self-energies are the same.

Note that in the preceding discussion we have expressed the different quantities in the imaginary-frequencies domain, because the Anderson impurity problem is more conveniently solved on the imaginary axis. From the knowledge of the self-energy $\Sigma_{lat}(k, i\omega_n)$, one can extract the quasiparticle weight Z, defined as

$$\frac{1}{Z} = \left(1 - \left. \frac{\partial \Sigma(\omega)}{\partial \omega} \right|_{\omega \to 0} \right) \, . \tag{2.46}$$

The derivative in this equation can be calculated from the imaginary-frequency self-energy thanks to the identity

$$\left. \frac{\partial \Sigma(\omega)}{\partial \omega} \right|_{\omega \to 0} = \left. \frac{\Sigma(i\omega_n)}{i\omega_n} \right|_{\omega_n \to 0} \, . \tag{2.47}$$

For weakly correlated metals, the self-energy is small and the quasiparticle weight is close to one, whereas for a Mott insulator the quasiparticle weight vanishes due to a divergence of the self-energy. One of the advantages of DMFT is that it can smoothly interpolate between a weakly interacting metal and a Mott insulator, depending on the quasiparticle weight that can take any value between zero and one. This is particularly important for strongly correlated metals, for which the quasiparticle weight is small but does not vanish.

There are several ways to combine DFT with DMFT to calculate the properties of strongly correlated materials from first principles. In Chapter 5, the approach used is to derive an effective tight-binding model in the basis of Wannier functions for the bands close to the Fermi level from a GGA calculation. The choice of correlated Wannier functions is then an educated guess and the Hubbard parameter U is treated as a free parameter.

2.4 Quasiparticle and excitonic effects

In linear-response theory, the key quantity to be calculated is the charge susceptibility χ, defined as the change of the electronic charge density δn upon an external perturbation δv_{ext}

$$\chi(r,t,r',t') = \frac{\delta n(r,t)}{\delta v_{ext}(r',t')} \, . \tag{2.48}$$

The charge susceptibility is related to the inverse dielectric function ϵ^{-1}. In frequency space, we have

$$\epsilon^{-1}(r,r',\omega) = \delta(r-r') + \int \mathrm{d}r'' v_c(r'',r)\chi(r'',r',\omega) \, , \tag{2.49}$$

where v_c is the Coulomb potential. Knowledge of the full charge susceptibility is important as it can be measured, e.g. in optical absorption experiments.

Let us define the independent-particle susceptibility χ_0, which can be expressed in terms of single-particle wave functions ψ_i (e.g. Kohn-Sham wave functions in DFT) and energies ϵ_i as

$$\chi_0(r,r',\omega) = \sum_{c,v} \frac{\psi_v^*(r)\psi_c(r)\psi_c^*(r')\psi_v(r')}{\omega - (\epsilon_c - \epsilon_v) - i0^+} - \frac{\psi_v(r)\psi_c^*(r)\psi_c(r')\psi_v^*(r')}{\omega + (\epsilon_c - \epsilon_v) + i0^+} \, , \tag{2.50}$$

where c refers to unoccupied conduction band states and v refers to occupied valence band states (an insulator is assumed). Note that the poles of χ_0 correspond to the independent-particle excitation energies. The full susceptibility contains poles at the real excitation (i.e. excitons for insulators) energies of the system.

The full interacting susceptibility χ is related to χ_0 via a Dyson equation [48]

$$\chi = \chi_0 + \chi_0(v_c + f_{xc})\chi_0 + \chi_0(v_c + f_{xc})\chi_0(v_c + f_{xc})\chi_0 + \cdots = \chi_0 + \chi_0(v_c + f_{xc})\chi \, , \tag{2.51}$$

where $v_c + f_{xc}$ is the *kernel*. The crudest approximation is to set $f_{xc} = 0$, and is known as the random phase approximation (RPA). The next level of approximation is the adiabatic local-density approximation (ALDA), in which f_{xc} is local in time and in space

$$f_{xc}(r,t,r',t') = \delta(t-t')\delta(r-r')\frac{\delta^2 E_{xc}^{LDA}[n]}{\delta n(r)\delta n(r')} . \tag{2.52}$$

The RPA and ALDA fail to capture the long-range electron-hole attraction, that is responsible for the reduction of the excitation energies compared to the independent-particle picture (excitonic effects). Eq. 2.51 is in principle exact, and the challenge of time-dependent density functional theory (TDDFT) is to find good approximations for the kernel.

Within TDDFT, instead of solving the Dyson equation for the charge susceptibility χ, an alternative approach to calculate excitation energies consists in solving the Casida equation [48, 49]

$$\begin{pmatrix} A & B \\ B & A \end{pmatrix}\begin{pmatrix} X \\ Y \end{pmatrix} = \Omega \begin{pmatrix} -1 & 0 \\ 0 & 1 \end{pmatrix}\begin{pmatrix} X \\ Y \end{pmatrix} . \tag{2.53}$$

In the commonly-used Tamm-Dancoff approximation, one sets $B = 0$. The matrix A is given by

$$A_{ia,jb}(\omega) = \delta_{ij}\delta_{ab}(\epsilon_a - \epsilon_i) + K_{ia,jb}^{Hxc}(\omega) . \tag{2.54}$$

In this equation, i, j refer to occupied Kohn-Sham orbitals with energies $\epsilon_{i,j}$, while a, b identify unoccupied Kohn-Sham orbitals of energies $\epsilon_{a,b}$. The matrix $K_{ia,jb}^{Hxc}(\omega)$ is the Hartree-exchange-correlation kernel. It is frequency independent in the adiabatic approximation. It is given by

$$K_{ia,jb}^{Hxc} = \int \mathrm{d}r\mathrm{d}r' \psi_i^*(r)\psi_a(r) f^{Hxc}(r,r')\psi_j(r')\psi_b(r') . \tag{2.55}$$

Solving Eq. 2.53 yields the excitation energies of the system, given by the eigenvalues Ω, and the optical spectrum can be calculated from the vectors X and Y.

The Casida equation is analogous to the Bethe-Salpeter equation (BSE). In the Casida equation, the kernel takes the form $K^{Hxc} = K^H + K^{xc}$, where K^H is the Hartree contribution. In the Bethe-Salpeter equation the exchange-correlation part is replaced by the screened exchange, i.e. $K^{BSE} = K^H + K^W$, with

$$K_{ia,jb}^{W}(r,r') = -\int \mathrm{d}r\mathrm{d}r' \psi_a^*(r)\psi(r)_b W(r,r',0)\psi_j^*(r')\psi_i(r') , \tag{2.56}$$

where W is the screened Coulomb interaction, given by

$$W(r,r',0) = \int \mathrm{d}r'' \epsilon^{-1}(r,r'',0) v_c(r'',r') . \tag{2.57}$$

As discussed before, adiabatic semilocal approximations to the kernel of TDDFT, such as ALDA, fail to capture excitonic effects. This is can be understood from the fact that the dominant term in the BSE, yielding excitonic effects, is the K^W kernel, and is associated with the long-range exchange interaction, screened by the inverse dielectric matrix. The long-range exchange interaction is missing in LDA and GGA but it is included in Hartree-Fock (unscreened) and in hybrid functionals, where the screening is taken into account via the mixing and range-separation parameters (in HSE). As discussed in Ref. [50], this suggests that excitonic effects are *approximately* described within hybrid DFT, and that one can solve the Casida equation with a fraction of the bare Fock exchange (possibly calculated with the modified Coulomb interaction as in HSE) in the kernel. This approach is implemented in the VASP code [41, 42, 43]. Note that in the VASP code, the module that solves the Casida and Bethe-Salpeter equation is the same. When using Hartree-Fock or hybrid functional kernels, the only difference is the exact form of the exchange term. In Chapter 6, we shall calculate the exciton energies for single-layer $TiSe_2$ from hybrid functionals using the VASP code. Because of the analogies discussed above, we shall refer to the equation yielding the exciton spectrum as the Bethe-Salpeter equation.

The Bethe-Salpeter equation is often used in combination of the GW approximation to calculate the optical absorbtion spectra of semiconductors and insulators from first principles [51]. In the GW approximation, the quasiparticle wave functions ϕ_i obey the equations [52]

$$\left(-\frac{1}{2}\frac{\partial^2}{\partial r^2}+v(r)+v_H(r)\right)\phi_i(r)+\int \mathrm{d}r\Sigma(r,r',\omega=E_i)\phi_i(r')=E_i\phi_i(r)\ , \tag{2.58}$$

where Σ is the self-energy. Note that Eq. 2.58 is analogous to the Kohn-Sham equations, except that the exchange-correlation potential v_{xc} in Eq. 2.5 is replaced by the self-energy term. For semiconductors and insulators, the bandgaps within GW are larger than within Kohn-Sham DFT with LDA or GGA. The differences in the single-particle energies are referred to as *quasiparticle effects*.

The static Coulomb Hole plus Screened Exchange (COHSEX) approximation [53] of GW corresponds to setting $\Sigma(r,r',\omega)=\Sigma_{COH}(r,r',\omega=0)+\Sigma_{SEX}(r,r',\omega=0)$, with

$$\Sigma_{COH}(r,r',\omega=0)=\frac{1}{2}\delta(r-r')+(W(r,r',\omega=0)-v_c(r,r'))\ , \tag{2.59}$$

and

$$\Sigma_{SEX}(r,r',\omega=0)=\sum_{i,\text{occupied}}\phi_i(r)\phi_i^*(r')W(r,r',\omega=0)\ . \tag{2.60}$$

In this approximation, the SEX part closely resembles the (non-local) exchange-correlation potential $v_{xc}(r,r')$ in Hartree-Fock

$$v_{xc}^{HF}(r,r')=\sum_{i,\text{occupied}}\psi_i^*(r)\psi_i(r')v_c(r,r')\ , \tag{2.61}$$

the only difference being that an unscreened Coulomb potential v_c is used in Hartree-Fock. If the inverse dielectric matrix is approximated by a single element, the screened Coulomb potential W can be expressed as

$$W(r,r',\omega=0)=\int \mathrm{d}r''\epsilon^{-1}(r,r'',\omega=0)\,v_c(r'',r')\approx\frac{1}{\epsilon_\infty}v_c(r,r')\,. \tag{2.62}$$

From the discussion above, we see that there is a close analogy between hybrid density functional theory and the static COHSEX approximation of GW. In hybrid DFT, the static SEX part of the self-energy is modelled by the fraction of Fock bare exchange, with the mixing parameter α playing the role of $1/\epsilon_\infty$ in Eq. 2.62. The COH part of the self-energy, as well as frequency-dependent contributions, are on the other hand approximated by the local part of the exchange-correlation potential, modelled e.g. by the PBE approximation [34]. This discussion also explains why the PBE0 functional with a fraction of exchange fixed to $1/4$ fails quantitatively for large-gap and small-gap systems [34]. Indeed, large-gap insulators have a small dielectric constant, so the optimal mixing parameter should be large than $1/4$. On the other hand, small-gap semiconductors are characterized by larger dielectric constants, so $\alpha = 1/4$ is too large and the PBE0 functional with fixed fraction of exchange *overestimates* the gap.

In Chapter 6, we shall approximate quasiparticle and excitonic effects in $TiSe_2$ from hybrid DFT. Since $TiSe_2$ is a two-dimensional material, we shall not calculate $1/\epsilon_\infty$ but use the mixing parameter α as a free parameter. From the discussion presented in this section, we will indeed interpret α as a material-dependent quantity that describes the effective screening environment rather than a number fixed to $1/4$.

3 Crystal field effects in two-dimensional transition metal dichalcogenides

Chapter 3 is a pre-print version [54] of an Article submitted to:

Pasquier, Diego; Yazyev, Oleg V. *2D Materials* **submitted**

Two-dimensional transition metal dichalcogenides (TMDs) exist in two polymorphs, referred to as $1T$ and $1H$, depending on the coordination sphere of the transition metal atom. The broken octahedral and trigonal prismatic symmetries lead to different crystal and ligand field splittings of the d electron states, resulting in distinct electronic properties. In this work, we quantify the crystal and ligand field parameters of two-dimensional TMDs using a Wannier-function approach. We adopt the methodology proposed by Scaramucci *et al.* [A. Scaramucci *et al.*, J. Phys.: Condens. Matter 27, 175503 (2015)]. that allows to separate various contributions to the ligand field by choosing different manifolds in the construction of the Wannier functions. We discuss the relevance of the crystal and ligand fields in determining the relative stability of the two polymorphs as a function of the filling of the d-shell. Based on the calculated parameters, we conclude that the ligand field, while leading to a small stabilizing factor for the $1H$ polymorph in the d^1 and d^2 TMDs, plays mostly an indirect role and that hybridization between different d orbitals is the dominant feature. We investigate trends across the periodic table and interpret the variations of the calculated crystal and ligand fields in terms of the change of charge-transfer energy, which allows developing simple chemical intuition.

3.1 Introduction

With the advent of two-dimensional (2D) materials [1], layered transition metal dichalcogenides (TMDs) [55] have gained a great revival of interest due to their rich variety of properties of relevance to both applications and fundamental research [56, 57, 6, 15, 9]. Two-dimensional TMDs of chemical composition MX_2 consist of a triangular lattice of a transition metal atom (M = Mo, W, Re, etc.) sandwiched between two layers of a chalcogen element (X = S, Se, Te). The local coordination sphere of the transition metal atom can have either trigonal antiprismatic (or distorted octahedral) or trigonal prismatic symmetry, leading to two families of polymorphs, referred to as $1T$ and $1H$, respectively. The two polymorphs have distinct electronic properties. For instance, $1H$-MoS_2 is a semiconductor with promising applications [9], $1T$-MoS2 is metallic, and the distorted $1T'$-MoS_2 is predicted to be a topological insulator [15]. In a simplified ionic picture, one assigns formal charges 4+ and 2− to the transition metal and chalcogen ions, respectively [58]. In such a picture, the formal electronic configuration of the chalcogen atoms is $n_X s^2 n_X p^6$ (with n_X = 3, 4, 5 for X = S, Se, Te), while that of the transition metal M is $n_M d^n$ ($n_M = 3,4,5$), with n depending on the column where M stands in the periodic table ($n = 0$ for group IV TMDs such as HfS_2, $n = 1$ for group V TMDs such as TaS_2, and so on).

The electronic properties of the TMDs are therefore governed by the d-like bands and their filling [56]. The presence of the ligands splits the d-electrons levels due to a combination of different effects. The crystal field splitting originates from the electrostatic interaction between the orbitals and the ligands, leading to a higher energy for orbitals pointing towards negatively charged ions. The ligand field splitting results from hybridization with ligands' orbitals and is expected to be dominant in covalent systems.

According to crystal field theory, in an octahedral environment ($1T$ polymorph), the d-shell splits into a low-energy triplet (t_{2g}) and a high-energy doublet (e_g). In a trigonal prismatic geometry ($1H$), the low-energy triplet further splits into a doublet and a singlet, usually assumed to be lower in energy.

In the literature, ligand field arguments are often given as simple intuitive starting points to understand several properties of the TMDs. In particular, a longstanding problem in the field of dichalcogenides is that of the relative stability between the two polymorphs [7, 58], which is controlled by the column of the transition metal M in the periodic table, i.e. by the electron filling of the d-like bands. Indeed, d^0 TMDs are found in nature in the $1T$ polymorph, that is also predicted to be energetically more favourable by first-principles calculations. TMDs with formal occcupation d^1-d^2 are more stable in the $1H$ polymorph, while the $1T$ polymorph is metastable in a distorted form [59]. TMDs with $n = 3$ are most stable in a strongly distorted $1T$ phase with 2×2 periodicity [55, 58, 14, 60, 61], but the $1H$ polymorph is predicted to be lower in energy than the undistorted $1T$ one. Finally, TMDs in the $d^4 - d^6$ range are lower in energy in the $1T$ phase compared to the $1H$. Note that for some materials, unrelated pyrite structures are in certain cases the most stable phases [62].

A natural explanation for this trend is as follows [63]. For $n < 2$ d electrons, the $1H$ phase becomes more and more stable with respect the the $1T$ phase as the filling of the low-energy singlet increases. On the other hand, for $n > 2$ the $1H$ polymorph becomes less and less favourable with increasing the number of electrons because the higher-energy doublet gets filled. While being elegant and often invoked in the recent literature [63, 64], several authors have argued that it is likely too simplistic because of the complexity of the actual band structure [65, 58, 66].

The purpose of this paper is twofold. Firstly, we provide a systematic estimate of crystal and ligand field parameters across the family of materials from first-principles calculations, focusing on the case of monolayers. By constructing *ab initio* Wannier tight-binding Hamiltonians for different sets of bands, we estimate the bare crystal field coming from the electrostatic repulsion with the positively charged ions, as well as contributions stemming from hybridization with various ligands' states. Secondly, in light of the calculated parameters, we discuss the problem of the relative stability of the $1H$ and $1T$ materials as a function of the column of the transition metal M in the periodic table. We show that the singlet low-energy state in the $1H$ polymorph is close in energy to the t_{2g} triplet in the $1T$ polymorph, meaning that the ligand field alone plays a minor if any role in determining the relative stability. However, we also argue that, taking into account interorbital hybridization in the $1H$ case, resulting from nearest-neighbor hoppings between orbitals of different character, the calculated energy diagrams can provide a simple picture for the calculated relative stability of the two phases.

This paper is organized as follows. In Sec. 3.2, we review the methodology adopted and provide computational details of our calculations. In Sec. 3.3, a detailed study of TaS_2 is given as an example. In Sec. 3.4, we discuss the relevance of the crystal and ligand field in determining the relative stability of the $1H$ and $1T$ phases, taking again TaS_2 as a representative example. In Sec. 3.5, we present trends in the calculated parameters across the periodic table. In Sec. 3.6, we put our study in perspective with previous work, and Sec. 3.7 offers conclusions and outlook.

3.2 Methodology

3.2.1 Wannierization and crystal field parameters

We begin by briefly reviewing the methodolgy proposed in Ref. [67] that we have embraced in order to calculate the crystal field and ligand field parameters. Given a set of n isolated bands, one can define a corresponding set of n Wannier functions (WFs) [68] as follows

$$|\mathscr{W}_{R\alpha}\rangle = \frac{1}{\sqrt{N}} \sum_{k,\alpha'} e^{-ikR} U_{\alpha'\alpha}(k) \left|\psi_{k\alpha'}\right\rangle , \tag{3.1}$$

where $\left|\mathscr{W}_{R,\alpha}\right\rangle$ denotes the Wannier function of character α centered in the lattice site R, N is the number of points in the discretized Brillouin zone, k is a pseudomentum, $U_{\alpha'\alpha}(k)$ is the gauge-fixing matrix, and the $\left|\psi_{k\alpha}\right\rangle$ are Bloch eigenstates. In this work, the Bloch eigenstates $\left|\psi_{k\alpha}\right\rangle$ are calculated from density functional theory (DFT) at the level of the generalized gradient approximation (GGA) and correspond to the Kohn-Sham states. The corresponding Bloch Hamiltonian can be expressed in the basis of the Wannier functions:

$$H = \sum_{k,\alpha} \epsilon_{k\alpha} \left|\psi_{k\alpha}\right\rangle \left\langle\psi_{k\alpha}\right| = \sum_{R,R',\alpha,\alpha'} H_{\alpha\alpha'}^{R-R'} |\mathscr{W}_{R\alpha}\rangle \langle\mathscr{W}_{R'\alpha'}| , \tag{3.2}$$

where the $\epsilon_{k\alpha}$ are the single-electron eigenenergies (i.e. the Kohn-Sham energies in a standard DFT calculation) and the matrix elements in the Wannier basis $H_{\alpha\alpha}^{RR'}$ can be interpreted as the on-site energies (for $R = R'$ and $\alpha = \alpha'$) and hopping parameters of a tight-binding model.

The construction of Wannier functions contains a high degree of arbitrariness in the choice of the set of bands and the gauge-fixing matrix $U_{\alpha\alpha'}$. A common choice for the gauge is that minimizing the spread functional Ω, leading to Maximally Localized Wannier Functions (MLWF) [69, 68] :

$$\frac{\delta\Omega[U]}{\delta U} = 0 \tag{3.3}$$

where the spread functional Ω is defined as :

$$\Omega = \sum_{\alpha} \left(\langle\mathscr{W}_{0\alpha}|\, r^2 \left|\mathscr{W}_{0\alpha}\right\rangle - |\langle\mathscr{W}_{0\alpha}|\, r \,|\mathscr{W}_{0\alpha}\rangle|^2\right) , \tag{3.4}$$

where r is the position operator. The advantages of MLWFs are numerous : the constructed Wannier functions are real and atomic-like, the minimization of the spread leads to a minimal overlap between different Wannier functions and therefore optimal interpolation power, and in principle no *a priori* knowledge of the orbital character of the bands is required. Although MLFWs were adopted as the most useful choice in Ref. [67], we have found it more convenient for the materials considered to use Projector Wannier Functions (PWFs), defined by using

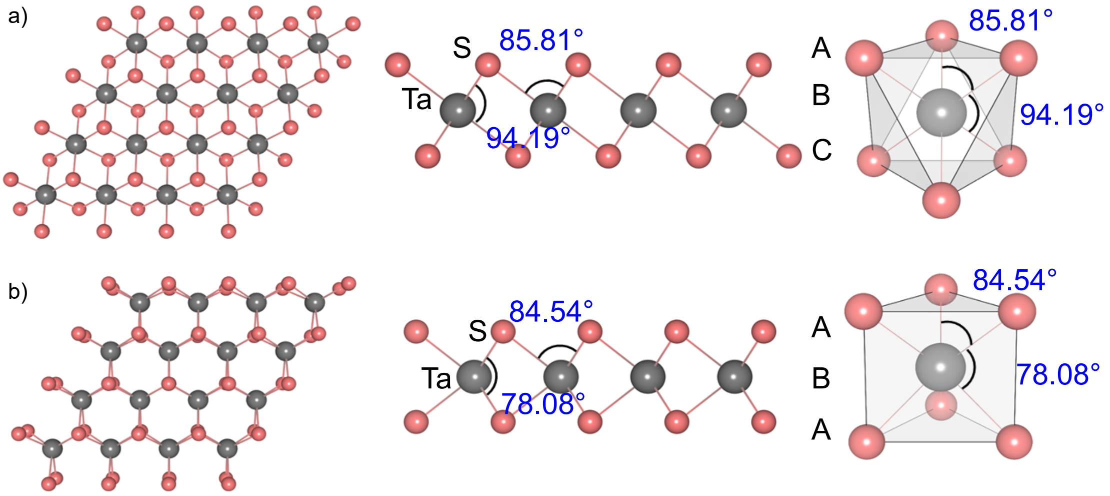

Figure 3.1 – Ball-and-stick representation of (a) the $1T$ polymorph, and (b) the $1H$ polymorph of two-dimensional TaS_2. The S-Ta-S angles are indicated and the coordination polyhedra for the two phases are displayed in the right panel.

orthogonalized Löwdin projections of the Bloch eigenstates on hydrogen-like atomic wave functions. This corresponds to fixing

$$U_{\alpha'\alpha}(k) = \sum_{\alpha''} (S^{-1/2}(k))_{\alpha''\alpha} \left\langle \psi_{k\alpha'} \middle| g_{\alpha''} \right\rangle , \tag{3.5}$$

where S is the overlap matrix, defined as $S_{\alpha\alpha'}(k) = \sum_n \left\langle g_\alpha \middle| \psi_{kn} \right\rangle \left\langle \psi_{kn} \middle| g_{\alpha'} \right\rangle$, and the $\left| g_\alpha \right\rangle$ are a set of localized trial orbitals. This choice allows for a better control of the orbital character of the Wannier functions, that is sometimes lost during the localization procedure. We shall explain this choice in more details in the next section, and argue that the calculated parameters are consistent with those obtained using MLWFs.

Another degree of freedom one has when constructing Wannier functions is the choice of the set of bands considered. In Ref. [67], it was suggested to use this freedom to estimate different contributions to the ligand field splitting of a given set of orbitals. For instance, if one is interested in the splitting of the valence d orbitals of a transition metal ion, one can construct Wannier functions by considering only the five bands with predominant d character, provided that those bands constitute an isolated manifold. In that case, the obtained MLWFs (or PWFs) correspond in general to molecular orbitals with some weight on the ligands due to hybridization. Therefore, the calculated splitting contains contributions both from the electrostatic interaction with the negatively charged ligand ions (crystal field), and from hybridization with various ligands' orbitals (ligand field). The ligand field can be read on the on-site part of the tight-binding Hamiltonian, i.e. on the diagonal of the matrix $H^{R=R'}_{\alpha\alpha'}$. For a meaningful interpretation of the differences of on-site energies as the ligand field, it is necessary that the matrix $H^{R=R'}_{\alpha\alpha'}$ is diagonal (or at least nearly-diagonal). In the following, this will be achieved in two ways. We will ensure that $H^{R=R'}_{\alpha\alpha'}$ is nearly diagonal by choosing appropriately the direction of the quantization axis z. Small off-diagonal terms, due to the deviation from perfect octahedral symmetry of $1T$ TMDs as well as due to the spin-orbit coupling in both polymorphs, lead to further splittings that we calculate by diagonalizing the matrix.

On the other hand, if a sufficiently large number of bands is included, the d-like Wannier functions do not contain tails on the ligands and are atomic-like, so that the extracted splitting can be interpreted as the bare crystal field. In order to separate different contributions to the ligand field, one can consider intermediate models by including in the wannierization procedure a set of ligand-derived bands with a certain orbital character, say p character, in addition to the d-like bands. In that case, the d-like Wannier functions do not contain any p-like tails on the ligands, but could contains tails coming from hybridization with other states. The obtained splitting contains therefore no contribution from hybridization with the p-states.

A further complication can arise if the bands of interest are entangled with another manifold. This complication arises, for instance, in late-group TMDs where the d-like and p-like manifolds overlap in energy. In that case, in order to obtain a Wannier Hamiltonian for the desired bands, we perform the disentanglement procedure of Souza, Marzari and Vanderbilt [70]. In order to derive n Wannier functions from $m > n$ bands in a certain energy window, one needs a criterion to extract an optimal subspace at each k-point of the discretized Brillouin zone. A possible prescription consists in using orthogonalized projections on a set of trial localized functions with desired orbital character. This corresponds to a choice of gauge-fixing matrix defined as in Eq. 3.5, except that the matrix is rectangular. Another choice consists in refining the subspace selection via projection by imposing optimal smoothness of the Hilbert space, through the minimization of the gauge-invariant part of the spread functional :

$$\Omega_I = \sum_{\alpha} \left(\langle \mathscr{W}_{0\alpha} | \, r^2 \, | \mathscr{W}_{0\alpha} \rangle - \sum_{R\alpha'} | \langle \mathscr{W}_{R\alpha'} | \, r \, | \mathscr{W}_{0\alpha} \rangle |^2 \right). \tag{3.6}$$

In the following, we shall adopt the optimal smoothness prescription whenever disentanglement is required.

3.2.2 Computational details

Density functional calculations are performed using the QUANTUM ESPRESSO package [40]. The exchange-correlation functional is approximated by the generalized gradient approximation of Perdew, Burke, and Erzernhof (PBE) [29]. Optimized norm-conserving Vanderbilt pseudopotentials [71, 72, 73], from the SG15 library [71, 72, 74], are used to described the interaction between valence and core electrons. The transition metals' s and p semi-core states are explicitly treated as valence electrons, as well as f states in the case hafnium. A plane-wave cutoff of 100 Ry is used for all the materials considered. For tantalum disulfide, we have also used ultrasoft pseudopotentials from the pslibrary [75, 76] for the calculation of the projected density of states.

We have checked that the band structures calculated with the two sets of pseudopotentials are identical. Brillouin zone integration is carried out using a mesh of 24×24 k-points and a Marzari-Vanderbilt smearing [77] of 10 mRy. The structure of each material is obtained by fully relaxing the lattice constant and atomic positions until all the Hellman-Feynman forces are smaller than 10^{-4} Ry/Bohr and the pressure is smaller than 0.1 Kbar. About 13 Å of vacuum is inserted between periodic replicas to simulate a monolayer. Wannierization is carried out on a grid of 12×12 k-points using the Wannier90 code [78].

3.3 The case of TaS$_2$

3.3.1 spd, pd, and d models

As an example, we focus our attention on tantalum disulfide (TaS$_2$), a material existing in both polymorphs (in bulk and monolayer forms [55, 79, 80]) and well known for its exotic phase diagram in the $1T$ case, that includes several charge density wave (CDW) transitions and a Mott (or possibly Anderson) insulating phase [81, 82, 16]. TaS$_2$ is a convenient case to study because the five d-like bands are separated in energy from the lower energy sulfur p-like bands, so that there is no need in disentangling the two manifolds. Moreover, this will allow us to compare our results with the early estimate of Mattheiss [65] in Sec. 3.6.

TaS$_2$ belongs to the group V TMDs, so that the formal electronic configuration of Ta^{4+} is $5d^1 6s^0$. The crystal structures of the $1T$ and $1H$ phases are shown in Fig. 3.1. The unit cell in the two phases contains one formula unit. As one can see in Fig. 3.1, the $1T$ and $1H$ phases are characterized by ABC and ABA stackings of the S-Ta-S atomic planes, leading to distorted octahedral (or trigonal antiprismatic) and trigonal prismatic coordinations. The calculated lattice constants $a_{1T/1H}$, tantalum-sulfur distances $d_{1T/1H}$, and S-Ta-S angles are summarized in Table 3.1. From the calculated S-Ta-S angles $\theta_{1T} = 94.19°(85.81°)$ and $\theta_{1H} = 78.08°$ $(84.54°)$, as shown in Fig. 3.1, we notice small deviations from a perfect octahedron ($\theta = 90°$) and a perfect trigonal prism with equal edges ($\theta \approx 80.8°$), respectively. In Fig. 3.2, we show the calculated PBE band structures and density of states. We have highlighted in color the sulfur s- and p-like bands, as well as the tantalum d-like bands. As the projected density of state plot shows, there is strong hybridization, especially between the Ta-d and S-p states, indicating the covalent nature of the Ta-S bond. Nevertheless, throughout this work, we shall continue referring to the five bands shown in red in Fig. 3.2 as the d bands, to the six bands shown in blue as the p bands, and to the two bands shown in purple as the s bands. We also note that the purple s bands contain non-negligible d character, suggesting that hybridization between s and d states also contributes to the ligand field splitting of the d-like states.

The band structure suggests that three natural models can be considered to describe valence electrons, that is a 13-band spd model, an 11-band pd model, and a 5-band d model. Let us first consider the 13-band spd model. We construct Wannier functions, as well as the corresponding Wannier Hamiltonian, as described in Sec. 3.2, by including simultaneously the s, p and d bands.

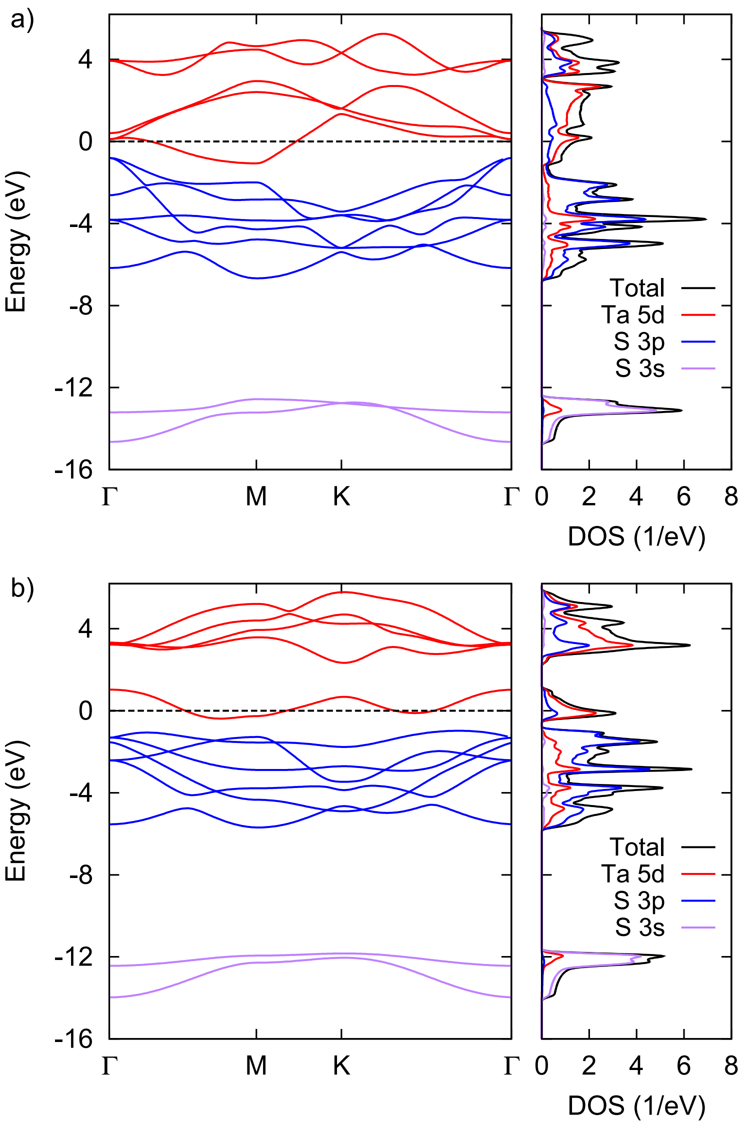

Figure 3.2 – Band structure along high-symmetry directions and projected density of states for (a) $1T$-TaS$_2$, and (b) $1H$-TaS$_2$. The d-like bands are shown in red, the p-like bands in blue, and the s-like bands in purple. The dashed line corresponds to the Fermi level, set to zero.

Table 3.1 – Calculated structural parameters for the undistorted $1T$ and $1H$ phases of TaS$_2$.

	a (Å)	d (Å)	θ (°)
$1T$	3.38	2.48	94.19
$1H$	3.34	2.48	78.08

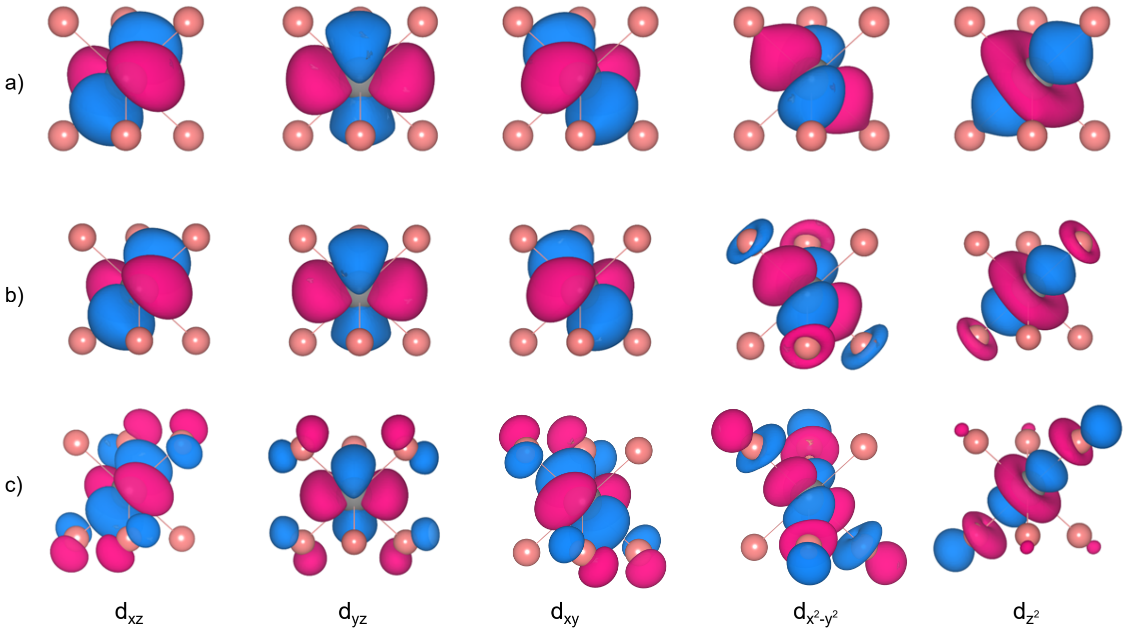
a)
b)
c)
d_{xz}
d_{yz}
d_{xy}
$d_{x^2-y^2}$
d_{z^2}

Figure 3.3 – Isovalue plots of the five d Wannier functions of $1T$-TaS$_2$ in the (a) spd model, (b) pd, and (c) d models.

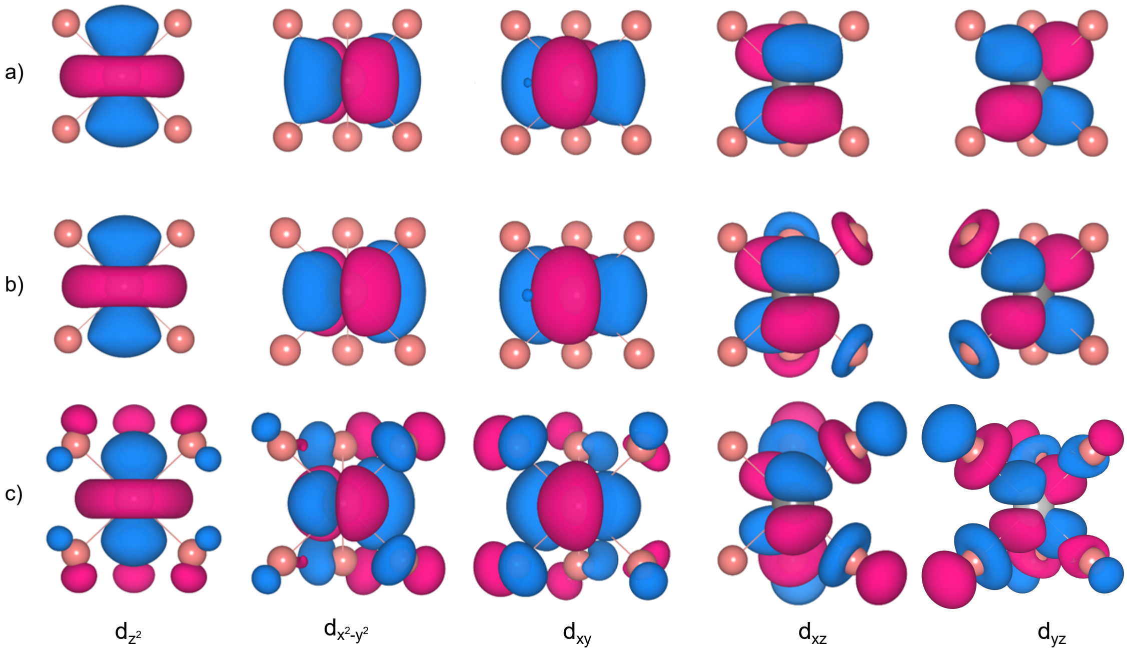
a)
b)
c)
d_{z^2}
$d_{x^2-y^2}$
d_{xy}
d_{xz}
d_{yz}

Figure 3.4 – Isovalue plots of the five d Wannier functions of $1H$-TaS$_2$ in the (a) spd model, (b) pd, and (c) d models.

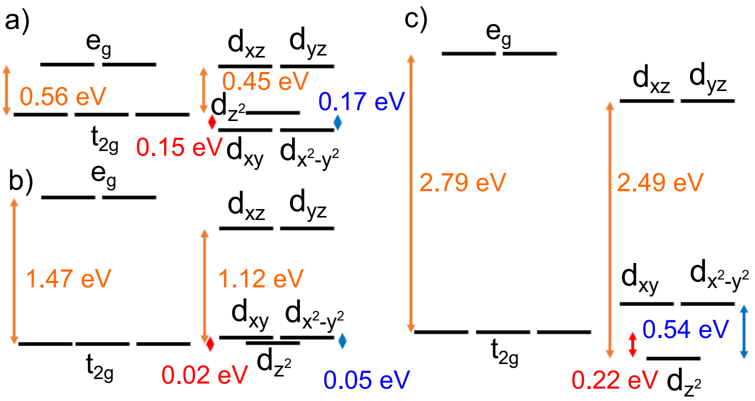

Figure 3.5 – Aligned energy levels for $1T$- (left) and $1H$- (right) TaS$_2$ in the (a) 13-band spd model, (b) 11-band pd, and (c) 5-band d models. The t_{2g} states in the $1T$ case are the d_{xy}, d_{xz}, d_{yz} ones, as shown in Fig. 3.3. The orange arrows correspond to the t_{2g}-e_g ($1T$) and d_{z^2}-d_{xz} splittings ($1H$). The blue arrows correspond to the splitting of the low-energy triplet in the $1H$ case, and the red arrows indicate the alignment between the lowest-energy levels of the two polymorphs.

For $1T$-TaS$_2$ the two high-energy d bands are slightly entangled with higher-energy bands, not shown in Fig. 3.2. Therefore, we perform the disentanglement procedure sketched in Sec. 3.2. A comparison between the disentangled bands and the PBE bands is provided in the appendix n, in Sec. 3.8. We obtain two s-like and six p-like WFs, centered on the sulfur atoms, as well as five d-like WFs centered on the tantalum atom. In Fig. 3.3(a) and Fig. 3.4(a), we present isovalue plots of the obtained d-like WFs. As the reader will notice, we have chosen different coordinate systems for the two polymorphs, for reasons that we will explain below. For the $1T$ case, the z-axis is defined along one of the Ta-S bonds. Since the octahedral symmetry is broken and the S-Ta-S angles are not 90° (but either 94.19° or 85.81°), it is not possible to chose at the same time the x and y axes to be exactly parallel to Ta-S bonds. On the other hand, for the $1H$ polymorph, the z-axis is pointing in the out-of plane direction, while the x-axis is chosen parallel to one of the lattice primitive vectors. As one can see in Figs. 3.3 and 3.4, the d-like WFs in the spd model are atomic-like and do not contain any visible hybridization with the sulfur $3s$ and $3p$ orbitals. Therefore, the calculated energy differences between the on-site energies of the WFs, obtained by inspecting the d block of the Wannier Hamiltonian, should be a good approximation to the bare crystal field, coming from the electrostatic interaction with the negatively charged sulfur ions. The calculated energy splittings are reported schematically in Fig. 3.5(a).

For $1T$-TaS$_2$, we obtain a three-below-two energy splitting pattern, as expected from crystal field theory. The three d_{xz}, d_{yz} and d_{xy} WFs have on-site energies that are degenerate within 0.01 eV. On the other hand, the two $d_{x^2-y^2}$ and d_{z^2} WFs are higher in energy by 0.56 eV, with a small difference of $\Delta^{(13)}_{z^2-x^2y^2} = \epsilon^{(13)}_{z^2} - \epsilon^{(13)}_{x^2-y^2} = 0.03$ eV, where $\epsilon^{(13)}_{\alpha}$ refers to the on-site energy of the WF of type α in the 13-band model. In the following, we shall refer to the d_{xz}, d_{yz} and d_{xy} WFs as the t_{2g} triplet, and to the $d_{x^2-y^2}$ and d_{z^2} WFs as the e_g doublet, because the octahedral symmetry remains a useful approximate symmetry. Whenever discussing the crystal or ligand field splitting

Table 3.2 – Summary of spreads (Ω), energy levels (ϵ), and splittings (Δ) for the d WFs in various models. The meaning of the different models is explained in the text. The energy reference is arbitrary, but consistent between different models of a polymorph.

Model 1T	Ω_{z^2} (Å^2)	$\Omega_{x^2-y^2}$ (Å^2)	$\Omega_{t_{2g}}$ (Å^2)	ϵ_{z^2} (eV)	$\Delta_{z^2-x^2y^2}$ (eV)	$\Delta_{e_g-t_{2g}}$ (eV)
d (5)	6.36	6.33	4.68	5.52	0.03	2.79
pd (11)	2.96	2.95	2.03	2.95	0.03	1.47
spd (13)	2.65	2.64	2.03	2.03	0.03	0.56
$spspd$ (17)	2.65	2.64	1.99	2.03	0.03	0.58
$spdds$ (24)	1.32	1.31	1.37	3.85	0.03	0.87
$spddsp$ (27)	1.20	1.20	1.42	3.88	0.03	0.91

Model 1H	Ω_{z^2} (Å^2)	Ω_{xy} (Å^2)	Ω_{xz} (Å^2)	ϵ_{z^2} (eV)	Δ_{xy-z^2} (eV)	Δ_{xz-z^2} (eV)
d_{z^2} (1/4)	15.59	9.73	5.34	0.84	3.28	4.32
d (5)	3.93	4.80	5.34	2.66	0.54	2.49
pd (11)	2.13	2.37	2.39	1.65	0.05	1.12
spd (13)	2.13	2.27	2.21	1.65	-0.17	0.45
$spspd$ (17)	2.13	2.28	2.21	1.62	-0.19	0.47
$spdds$ (24)	1.51	1.26	1.24	3.18	-0.09	0.65
$spddsp$ (27)	1.15	1.21	1.22	3.32	-0.07	0.52

between the e_g doublet and the t_{2g} triplet, we actually mean the difference between the average on-site energies.

For 1H-TaS$_2$, because of the trigonal prismatic coordination, crystal field theory predicts a splitting of the d levels into a singlet a_1' (following the notation of Ref. [7]), a low-energy doublet e' and a high-energy doublet e''. As shown in Fig. 3.5a), we have obtained, in the spd model, two degenerate doublets $d_{xy}/d_{x^2-y^2}$ and d_{xz}/d_{yz}, corresponding to the e' and e'' doublets, respectively. The on-site energies within a doublet differ by less than 0.005 eV. Contrary to the 1T case where the lowering of the symmetry from octahedral to trigonal antiprismatic leads to intrinsic lifting of degeneracies, we interpret those small differences being due to the wannierization procedure that does not preserve exactly the symmetries. In the spd model, we find that the d_{z^2} a_1' singlet is 0.17 eV higher in energy compared to the $d_{xy}/d_{x^2-y^2}$ doublet, and 0.45 eV lower than the d_{xz}/d_{yz} doublet. In Ref. [7], Huisman *et al.* considered a point-charge model to calculate the crystal field splitting in a trigonal prismatic coordination. Huisman *et al.* obtained that the relative positions of the singlet and low-energy doublet depends sensitively both on the angle between the ligand and the z-axis, and on the spread of the orbitals. Using parameters assumed relevant for MoS$_2$, it was estimated that the singlet a_1' should be higher in energy than the e' doublet. As we shall discuss in Sec. 3.5 where we study other TMDs, we have consistently found that, in the spd model, the d_{z^2} singlet is slightly higher in energy than the $d_{xy}/d_{x^2-y^2}$ doublet, except for d^6 TMDs where the whole crystal field splitting is reversed.

Both for the $1T$ and $1H$ polymorphs, the calculated energy splittings are rather small (~ 0.5 eV) compared to the overall bandwidth of the five d bands (~ 7 eV). This is in agreement with the intuitive expectation that for covalent bonding, electrostatic effects should not be dominant, while the hybridization with the ligands' valence orbitals is important. We have then considered an 11-band pd model, by constructing six p WFs and five d WFs from the bands shown in blue and red in Fig. 3.2 simultaneously. In Figs. 3.3(b) and 3.4(b), we present plots of the corresponding d WFs. We see that, although the isovalue for the plots is the same as for the WFs in the spd model, certain WFs exhibit considerable weight on the sulfur atoms, typical of molecular orbitals with antibonding character. Indeed, the on-site energies of some of the d WFs are shifted upward in energy compared to the spd model, as we summarize in Table 3.2. The differences of on-site energies between the spd and pd models can be interpreted as the hybridization energy between s and d orbitals [67].

For the $1T$ case, we obtain hybridization energies $\epsilon_{e_g}^{(11)} - \epsilon_{e_g}^{(13)} = 0.92$ eV, and $\epsilon_{t_{2g}}^{(11)} - \epsilon_{t_{2g}}^{(13)} \approx 0$ eV. Also, the spread Ω of the e_g WFs, defined in Sec.3.2, increases from 2.65 Å^2 to 2.95 Å^2, whereas the spread of the t_{2g} WFs is identical in the two models. This indicates lack of hybridization between t_{2g} d orbitals and sulfur s orbitals, consistent with the observation in the projected density of states plot, in Fig. 3.2(a), that the three low-energy d bands have negligible sulfur s character. Therefore, we conclude that the hybridization with the s orbitals leads to a significant increase of the ligand field splitting of 0.91 eV, as represented in Fig. 3.5(b). It is worth mentioning that the on-site energies of the p WFs change only slightly between the two models, as one would expect by noticing in Fig.3.2(a) that the s bands have a negligible p character. We obtain a small difference between the average of the on-site energies of $\bar{\epsilon}_p^{(11)} - \bar{\epsilon}_p^{(13)} = 0.06$ eV.

For the $1H$ polymorph, as we report in Table 3.2, sd hybridization leads to an increase of the on-site energy of two two doublets, while the d_{z^2} singlet remains unaffected. The splitting $\Delta_{xz-z^2} = \epsilon_{xz} - \epsilon_{z^2}$ therefore increases from 0.45 eV to 1.12 eV in the pd model, meaning a hybridization energy of 0.67 eV for the high energy d_{xz}/d_{yz} doublet. As shown in Fig. 3.5, the splitting $\Delta_{xy-z^2} = \epsilon_{xy} - \epsilon_{z^2}$ has a different sign compared to the spd model, because of the sd hybridization energy $\epsilon_{xy}^{(11)} - \epsilon_{xy}^{(13)} = 0.22$ eV for the low-energy $d_{xy}/d_{x^2-y^2}$ doublet.

In order to account for the pd-hybridization contribution to the ligand field, we consider a 5-band d-only model, constructed by including only the five d bands during the wannierization procedure. In Fig. 3.3(c), we show isovalue plots of the derived WFs. We see that all five WFs have large weight on the sulfur atoms and resemble molecular orbitals with large pd antibonding hybridization. We observe that π-bonding occurs for the t_{2g} WFs, while σ-bonding takes place in the case of the e_g WFs. This leads to a larger hybridization energy for the e_g WFs, $\epsilon_{z^2}^{(5)} - \epsilon_{z^2}^{(11)} = 2.57$ eV, causing an increase of the e_g-t_{2g} splitting of 1.32 eV, so that it is 2.79 eV in the 5-band model.

In Fig. 3.4(c), we show isovalue plots of the five WFs in the d-only model for $1H$-TaS$_2$. As for the $1T$ polymorph, it is apparent that all five WFs resemble molecular orbitals with antibonding character. The d_{z^2} WF forms π-antibonding combinations with the sulfur p orbitals. The

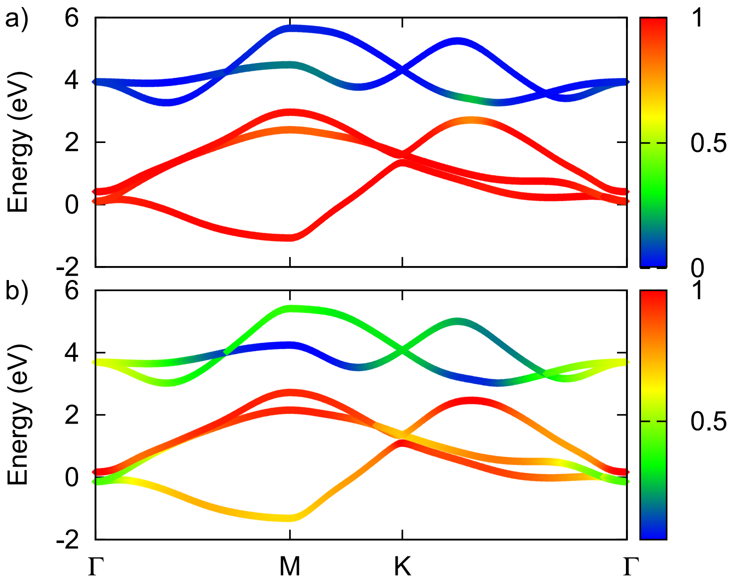

Figure 3.6 – Band structure for the 5-band model of $1T$-TaS$_2$ with orbital weight as a color code of the (a) t_{2g} (d_{xy}, d_{xz} and d_{yz}, with z along a Ta-S bond) WFs, and (b) d_{z^2}, d_{xy} and $d_{x^2-y^2}$ WFs, with z in the out-of-plane direction. The Fermi level is set to zero.

calculated pd hybridization energy is given by $\epsilon^{(5)}_{z^2} - \epsilon^{(11)}_{z^2} = 1.01$ eV. The $d_{xy}/d_{x^2-y^2}$ and d_{xz}/d_{yz} doublets interact more strongly with the ligands' p orbitals, leading to increased ligand field parameters $\Delta^{(5)}_{xy-z^2} = 0.54$ eV and $\Delta_{xz-z^2} = 2.49$ eV, as shown in Fig. 3.5(c).

It is now appropriate to discuss in more detail the different choices of coordinate system for the $1T$ and $1H$ polymorphs. In the literature, crystal field arguments are often given to qualitatively describe the electronic structure of dichalcogenides. For $1T$ TMDs, while the ligand field spitting is often discussed using the same coordinate system as here (see e.g. Refs. [56, 14, 83]), some authors discuss the low energy triplet in terms of d_{z^2}, d_{xy} and $d_{x^2-y^2}$ orbitals with the z axis pointing in the out-of-plane direction, following Mattheiss [65]. In Fig. 3.6(a), we show the band structure of $1T$-TaS$_2$ with the orbital weight of the three t_{2g} WFs in the 5-band model that we have discussed above. We see that the t_{2g} WFs give rise to the three low-energy bands, and that the hybridization with the e_g WFs is very weak. We interpret the weak t_{2g}-e_g hybridization as resulting from weak the distortion of the octahedral symmetry. In Fig. 3.6(b), we show the orbital weight of the three low-energy orbitals with the z-axis defined out-of plane, as for the $1H$ polymorph. With this choice of axes, the on-site part of the Wannier Hamiltonian contains large off-diagonal matrix elements $H^{R=R'}_{\alpha\neq\alpha'}$ (~ 1.2 eV in the d model, against ~ 0.1 eV with the other coordinate choice), so that the three low-energy WFs strongly hybridize with the two high-energy WFs, as can be seen in Fig. 3.3(b). By inspection of the on-site energies of the WFs, we obtain the same ordering as in the $1H$ case, with a splitting $\epsilon^{(5)}_{xy} - \epsilon^{(5)}_{z^2} = 0.74$ eV. However, for both choices of coordinate systems, the same three-below-two splitting pattern is obtained upon diagonalizing the on-site Hamiltonian matrix, with identical energy eigenvalues. Therefore, our choice of coordinate system is motivated by the fact that the corresponding splitting of on-site energies

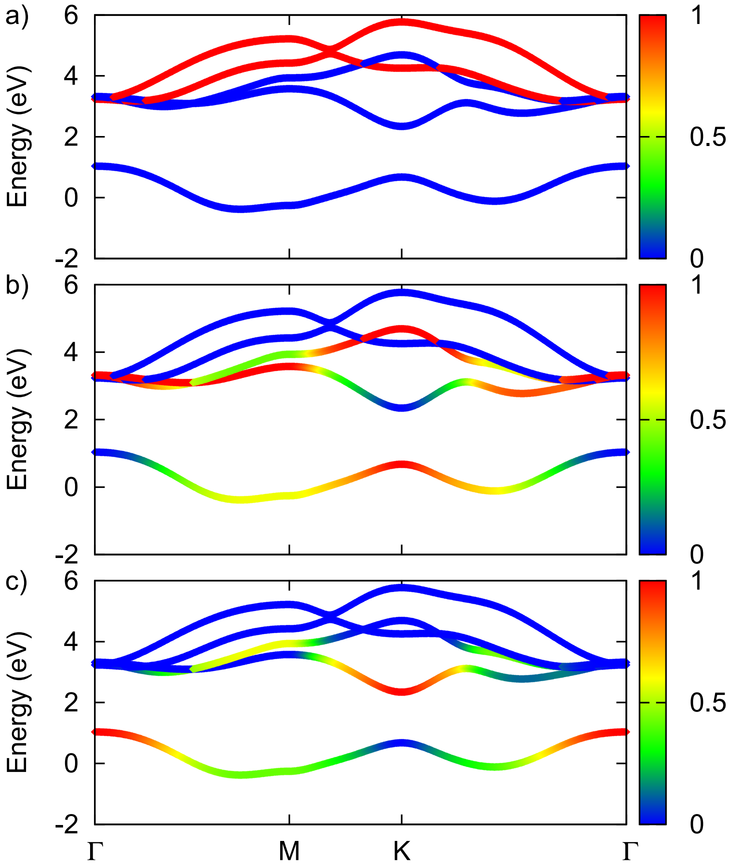

Figure 3.7 – Band structure for the 5-band model of $1H$-TaS$_2$ with orbital weight as a color code of the (a) two d_{xz} and d_{yz} WFs, (b) two d_{xy} and $d_{x^2-y^2}$ WFs, and (c) d_{z^2} WF. The Fermi level is set to zero.

leads to a better approximate picture for the electronic structure. On the other hand, for the $1H$ polymorph, the on-site Hamiltonian is exactly diagonal when the z-axis is chosen out-of-plane. From Fig. 3.7(a), it is evident that the two high-energy d_{xz}/d_{yz} WFs are decoupled from the three low-energy WFs.

It is worth mentioning that, although we have defined the WFs by projection and have not performed the localization procedure, the obtained PWFs are very close to maximal localization, with a nearly zero imaginary part. In the 5-band model, the ligand field spittings calculated with PWFs and MLWFs are nearly identical. The main difference arises in the 13-band model, where the localization procedure admixes the s WFs with other WFs, leading to a slightly reduced total spread but to less localized d-like WFs. We have also found that, in certain cases, the localization procedure leads to a change in coordinate system. Therefore, we have adopted PWFs instead of MLWFs, giving us a better control of the orbital character and the coordinate system.

3.3.2 Semi-core and high-energy states

In the 13-band model, the d-like WFs are atomic-like. However, it is expected that they are even more localized for models derived from a larger number of bands. We have therefore first considered including tantalum $5s$ and $5p$ semi-core states in the construction of the WFs. The changes in the spread of the WFs, on-site energies and splittings are summarized in Table 3.2. As expected, the effect of the inclusion of the semi-core states on the calculated crystal field splitting and on the spread of the d WFs is very weak, as core electrons are non-bonding by definition.

When plotting the d WFs of the 13-band model with a sufficiently small isovalue, one can recognize tails on the sulfur atoms that resemble d electrons. This means that d WFs are in fact bonding combinations of Ta $5d$ and S $3d$ orbitals. Since the excited-state bands above the Ta d-bands are highly entangled, it is not possible to isolate a set of bands corresponding to the sulfur d electrons. In order to assess the effect of Ta-d/S-d hybridization on the crystal field, we include 40 excited states above the Ta d bands and disentangle the Ta $6s$ and S $3d$ bands, keeping the 13 valence bands frozen. The tantalum $6s$ states are explicitly kept because they are lower in energy than the sulfur d ones. Therefore, we obtain a 24-band $spdds$ model, describing a finite set of excited states in addition to the valence bands. The corresponding band structure for $1T$-TaS$_2$ is shown in the appendix, in Sec. 3.8. The d WFs are more localized and have a higher energy than in the 13-band model, as summarized in Table 3.2. The energy splittings are somewhat increased compared to the 13-band model (0.87 eV against 0.56 eV for $1T$-TaS$_2$), indicating a small *negative* contribution to the total ligand field. We have also considered a 27-band $spddsp$ model, including Ta $6p$ states, that yields similar results.

To summarize, we conclude that the total e_g-t_{2g} splitting of 2.79 eV in $1T$-TaS$_2$ is the result of positive contributions from electrostatic effects and hybridization with ligands' $3s$ and $3p$ states, all of the order of ~ 1 eV, as well as a smaller negative contribution of 0.3 eV due to the formation of bonding combinations with the higher energy ligands' $3d$ states. Also, the d_{xy}-d_{z^2}

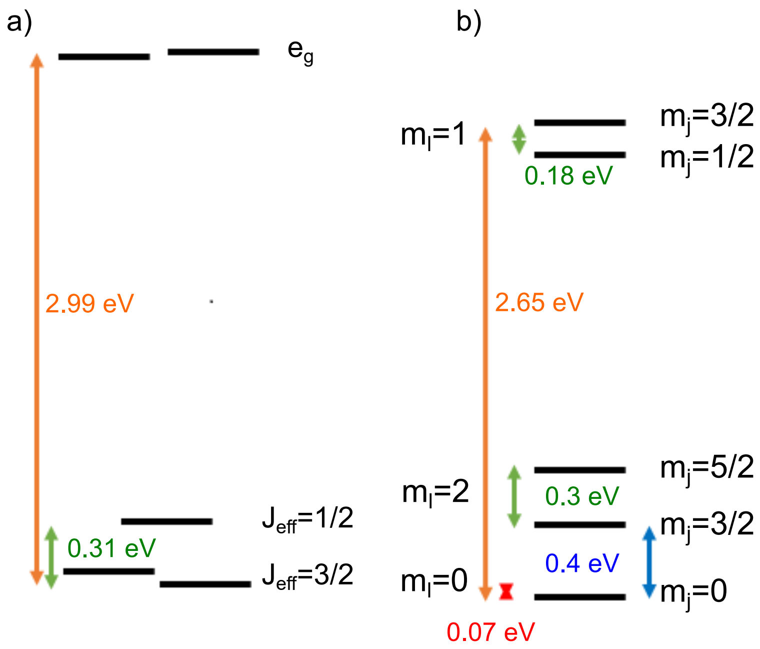

Figure 3.8 – Aligned ligand field energy diagram, including the SOC, for (a) $1T$-TaS$_2$, and (b) $1H$-TaS$_2$. The orange arrows indicate the splittings between the lowest- and highest-energy states, the green arrows indicate the splittings of otherwise degenerate states induced by the SOC, the blue arrow indicates the ligand field splitting of the low-energy states in the 1H case, and the red arrow correspond to the alignment between the lowest-energy state of the two polymorphs.

splitting of 0.54 eV in $1H$-TaS$_2$ comes from negative contributions due to electrostatic effects and hybridization with $3d$ states (of the order of ~ 0.1 eV each), and positive contributions from hybridization with $3s$ and $3p$ states (0.22 and 0.49 eV, respectively).

3.3.3 Spin-orbit coupling

The spin-orbit coupling (SOC) is strong in many TMDs and leads to many interesting effects, such as topological phases in distorted d^2 $1T$ TMDs [15], or Ising superconductivity in single-layer d^1 and doped d^2 $1H$ TMDs [84, 11]. Here, we investigate the effect of the SOC on the calculated ligand field splittings in $1T$- and $1H$-TaS$_2$. The SOC introduces off-diagonal imaginary matrix elements in the on-site part of the Hamiltonian, lifting degeneracies. In Fig. 3.8, we present the calculated ligand field diagrams in the d model with and without the SOC.

For the $1T$ polymorph, the SOC splits the t_{2g} manifold into a lower-energy $J_{\mathrm{eff}=3/2}$ doublet and a higher-energy $J_{\mathrm{eff}} = 1/2$ singlet. The calculated splitting of 0.31 eV is modest compared to the bandwidth (~ 3.5 eV) of the three t_{2g} bands, as well as compared to the ligand field splitting $\Delta^{(5)}_{e_g-t_{2g}} = 2.79$ eV. On the other hand, the e_g doublet remains nearly degenerate (within 0.03 eV). The degeneracy of the $J_{\mathrm{eff}} = 3/2$ doublet is lifted by 0.07 eV. These findings are in agreement with crystal field theory, that predicts a splitting of the t_{2g} shell induced by the SOC, but not of the e_g

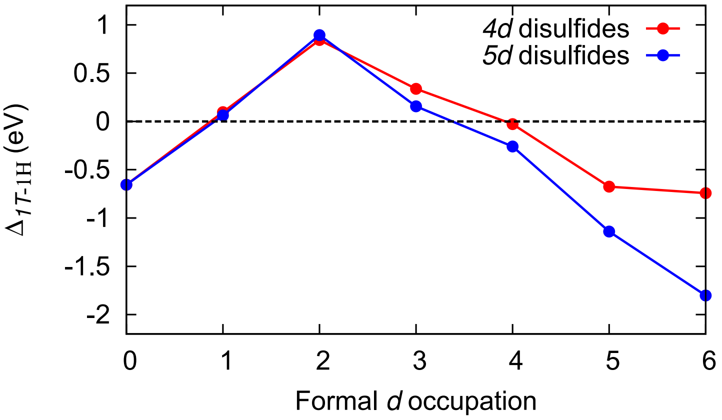

Figure 3.9 – Calculated total energy difference, per formula unit, between the 1*T* and 1*H* phases of 4*d* and 5*d* disulfides, as a function of the formal number of *d* electrons. A negative energy indicates higher stability of the 1*T* phase.

shell.

For 1*H*-TaS_2, Fig. 3.8 shows that the SOC splits the low-energy and high-energy doublets by 0.3 eV and 0.18 eV, respectively. We note that the SOC splitting is of the same magnitude as the ligand field Δ_{xy-z^2} splitting.

3.4 Crystal field and the relative stability of the 1*T* and 1*H* phases

Having estimated crystal field and ligand field parameters for TaS_2, we proceed to discussing their relevance in determining the relative stability of the 1*T* and 1*H* phases. In Fig. 3.9, we present the calculated total energy difference per formula unit $\Delta_{1T-1H} = (E_{1H} - E_{1T})$ for the series of material MS_2, with M belonging to the the 4*d* and 5*d* rows of transition metals. Fig. 3.9 shows that the 1*H* phase is energetically slightly more favourable than the 1*T* phase in the d^1 (NbS_2 and TaS_2) and d^3 cases (TcS_2 and ReS_2), highly favourable in the d^2 case (MoS_2 and WS_2), and unfavourable for any other filling. Note that some of the materials calculated in this plot, such as OsS_2, do not exist in nature in either the 1*T* or 1*H* polymorph (in neither bulk nor monolayer form). However, it is instructive to calculate their properties in order to discuss trends. In Fig. 3.9, we notice a discontinuity at the $4d^6$ point, corresponding to PdS_2. Indeed, the 1*H* polymorph of PdS_2 relaxes to a structure with a short S-S distance of ≈ 2 Å, leading to a qualitatively different electronic structure. Nevertheless, the corresponding structure is still highly unfavourable with respect to the 1*T* phase. In light of the preceding, we are now in a position to assess the role of crystal and ligand field effects in determining this trend. As in the previous section, we shall focus on the case of monolayer TaS_2 as an example. As we will show in the next section by discussing trends across the periodic table, the physics discussed here is not unique to TaS_2 but applies to the entire family of TMDs, because of the universality of the band structure. The discussion also applies to bulk materials as long as interlayer couplings are not too strong.

In Fig. 3.5, we have plotted the aligned crystal and ligand field energy diagrams for $1T$- and $1H$-TaS$_2$. In the 13-band model, the d_{z^2} state is actually slightly higher in energy compared to the $d_{x^2-y^2}$ and d_{xy} states, so that the bare crystal field does not favour a $d^1_{z^2}$ configuration for the $1H$ polymorph. However, as one can infer from the 11-band and 5-band models, hybridization effects with the ligand s an p states pushes the d_{xy} and $d_{x^2-y2^2}$ states ~ 0.5 eV higher in energy. Hence, in a local picture neglecting inter-site hoppings, the ground-state configuration for $n < 2$ d electrons is obtained by partially filling the d_{z^2} state, in agreement with the standard ligand field argument. From Fig. 3.5 (c), we observe that, in the d model, the d_{z^2} level in the $1H$ polymorph is 0.22 eV below the t_{2g} levels of the $1T$ polymorph. Note that the energy levels were aligned by equalizing the vacuum energies. Without such alignement, the energy difference is somewhat smaller, i.e. 0.06 eV. The calculated stabilizing energy of 0.22 eV is small compared to the amplitude of the bandwidths, or even compared to lifting of degeneracies induced by the octahedral symmetry breaking and by the spin-orbit coupling. Indeed, the stablilizing energy of the d_{z^2} singlet is reduced to 0.19 eV when the lifting of degeneracy of the t_{2g} states is taken into account (see Fig. 3.10(a), where we have represented with dashed lines the eigenenergies of the on-site Hamiltonian). When the SOC is included, as is shown in Fig. 3.8, the energy gain of the d_{z^2} level compared to the $J_{\text{eff}} = 3/2$ doublet is even more reduced to 0.07 eV (note that the SOC does not improve the relative stability of the $1T$ polymorph of TaS$_2$). While the ligand field *does* actually favour the $1H$ polymorph for $n < 2$ and disfavours it for $n > 2$, this effect appears to be rather weak and insufficient to explain the calculated trend presented in Fig. 3.9.

In Fig. 3.7, we plot the band structure of the $1H$ phase in the 5-band model with the orbital weights of the three groups of WFs in pannels (a), (b) and (c). As we have already discussed in Sec. 3.3, the d_{xz}/d_{yz} doublet is perfectly decoupled from the three low-energy Wannier functions. This is guaranteed by symmetry since the two groups of orbitals have a different parity under the exact mirror symmetry, i.e. they pick a different sign under the $z \to -z$ transformation. On the other hand, it is clear from Fig. 3.7(b)-(c) that the d_{z^2} WF strongly hybridizes with the d_{xy} and $d_{x^2-y^2}$ WFs, except at the high-symmetry Γ and K points.

From Fig. 3.7(b) and (c), we see that the isolated low-energy band is not only of d_z^2 character, but contains strong weight from the d_{xy} and $d_{x^2-y^2}$ WFs [65, 58]. The emergence of this isolated band is therefore not directly related to the ligand field splitting $\Delta_{z^2,xy}$, as often believed, but to the hybridization between the three low-energy Wannier functions. This was first emphasized by Mattheiss based on his early band structure calculations of layered TMDs [65]. Mattheiss noticed the mixed orbital character of the low-energy band, and showed (in the case of $2H$-MoS$_2$) that the gap closes if the interorbital hoppings are set to zero. More recently, Isaacs and Marianetti gave a similar argument for $1H$-VS$_2$ [66]. Considering an 11-band pd model derived from MLWFs, they showed that the low-energy isolated band is no longer isolated if the direct d-d hoppings are set to zero.

In the following, we argue that this gap opening can be understood from a simple intuitive band structure effect. At the Γ point, the d_{z^2} and $d_{xy} - d_{x^2-y^2}$ bands cannot hybridize because they belong to different representation of the point group. The gap at the Γ point (~ 2 eV) is much larger than the calculated ligand field, as it contains large contributions from band structure effects, especially from nearest-neighbor hoppings (NNHs). The d_{z^2} NNHs $t_{z^2z^2}$ are negative and equal in all directions so that the d_{z^2} band at the Γ point has an energy given by $\epsilon_{z^2}(k = \Gamma) \approx \epsilon^{(5)}_{z^2} - 6|t_{z^2z^2}|$, with $|t_{z^2z^2}| = 0.17$ eV. On the other hand, $d_{xy}/d_{x^2-y^2}$ WFs have hoppings with different signs along different directions, leading to a partial cancellation of NNH effects on the band energy at the zone center. The result is a band energy at the Γ point higher than the on-site energy by ~ 0.8 eV. Since the $d_{z^2} - d_{z^2}$ hoppings are negative, the d_{z^2} band disperses to higher energy as the momentum moves away from the Γ point, while the $d_{xy} - d_{x^2-y^2}$ bands split and disperse to lower energy. As Fig. 3.7 shows, the crossing between those bands is avoided, resulting in a rather large gap because the NNHs between the d_{z^2} and $d_{xy}/d_{x^2-y^2}$ WFs are large (~ 0.6 eV). At the K point, hybridization between the two sets of WFs is also prevented by symmetry, so that the corresponding state of the low-energy band is given by the bottom of one of the two $d_{xy}/d_{x^2-y^2}$-bands. We note that the interorbital hybridization is maximal at the bottom of the low-energy band, suggesting a strong stabilization effect for the $1H$ polymorph when the corresponding states are filled.

In order to estimate the contribution from interorbital hybridization to the stabilization of the $1H$ phase, we consider another model, derived by performing wannierization by considering the lower d band (1-band d'_{z^2} model) and the four higher-energy d bands (4-band model) *separately*. In Fig. 3.10(c), we show the d_{z^2}-like WF for the 1-band model. In the 1-band model, the obtained d_{z^2}-like Wannier function is strongly distorted compared to the 5-band model, while still resembling a d_{z^2} orbital. In the following, we shall refer to it as the d'_{z^2} WF, and to the two higher-energy WFs as d'_{xy} and $d'_{x^2-y^2}$. In Fig. 3.10(b), we report the aligned energy diagrams for the 5-band model of the $1T$ and $1H$ phases, as well as for the 1-band/4-band model for the $1H$ polymorph. The d'_{z^2} WF is much lower in energy in the 1-band model, with an energy gain of 2 eV compared to the t_{2g} states of the $1T$ phase. On the other hand, the d'_{xy} and $d'_{x^2-y^2}$ in the 4-band model are much higher in energy, 3.27 eV above the d'_{z^2} state.

From the discussion above, we conclude that the dominant effect for the calculated trend in Fig. 3.9 is the inter-site hybridization between Wannier functions with different orbital character. While the ligand field gives a small contribution, estimated in the 5-band model, its role is mostly an indirect one, i.e. producing different low-energy triplets in the two phases.

We would like to point out that the discussion here only applies to the relative stability of the ideal, undistorted $1T$ and $1H$ polymorphs. Since TMDs are known to be subject to various lattice instabilities, we will briefly discuss further complications that can affect the energetics. Materials with d^0 occupations are either insulators or semimetals. They are in general stable, with the notable exceptions of $1T$-TiSe$_2$, that undergoes an unusual insulator to insulator CDW transition [85], and $1T$-TiTe$_2$, where a semimetal to semimetal CDW transition was recently observed in the limit of a monolayer but not in thicker samples [19]. This is associated with a small energy gain of a few meVs and does not affect significantly the overall relative stability. In the d^1 family,

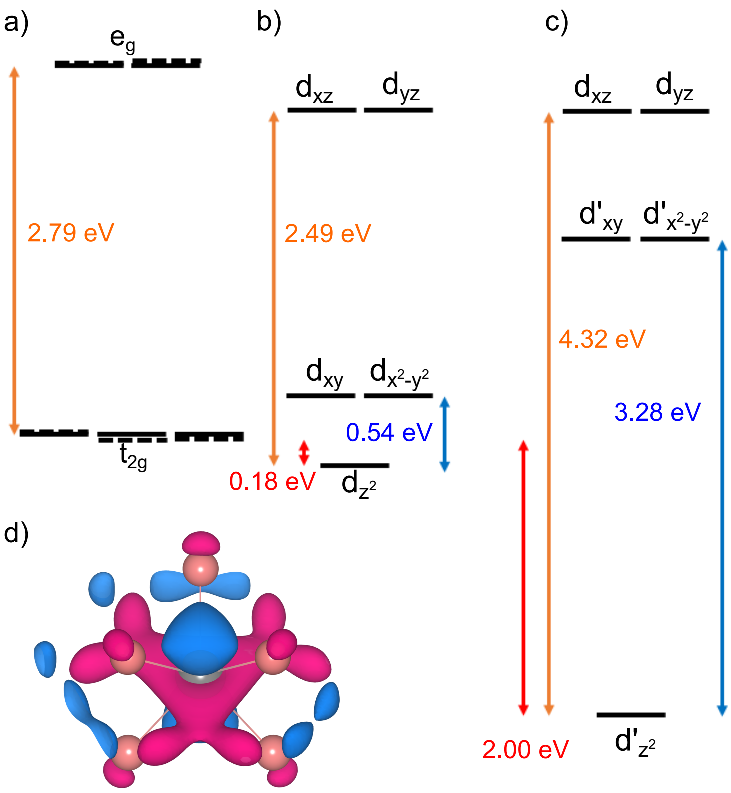
a)
e_g
2.79 eV
t_{2g}
b)
d_{xz}
d_{yz}
2.49 eV
d_{xy}
$d_{x^2-y^2}$
0.54 eV
0.18 eV
d_{z^2}
c)
d_{xz}
d_{yz}
d'_{xy}
$d'_{x^2-y^2}$
4.32 eV
3.28 eV
2.00 eV
d'_{z^2}
d)

Figure 3.10 – (a)-(b) Aligned ligand field diagrams for 1*T* and 1*H* TaS_2. The dashed lines correspond to the eigenvalues of the on-site Hamiltonian matrix for the 1*T* case. (c) Energy levels in the 1-band/4-band models (the meaning of which is explained in the text) for 1*H*-TaS_2. The orange arrows correspond to the t_{2g}-e_g (1*T*) and d_{z^2}-d_{xz} splittings (1*H*). The blue arrows correspond to the splitting of the low-energy triplet in the 1*H* case, and the red arrows indicate the alignment between the lowest-energy levels of the two polymorphs. (d) Isovalue plot of the d'_{z^2} Wannier function.

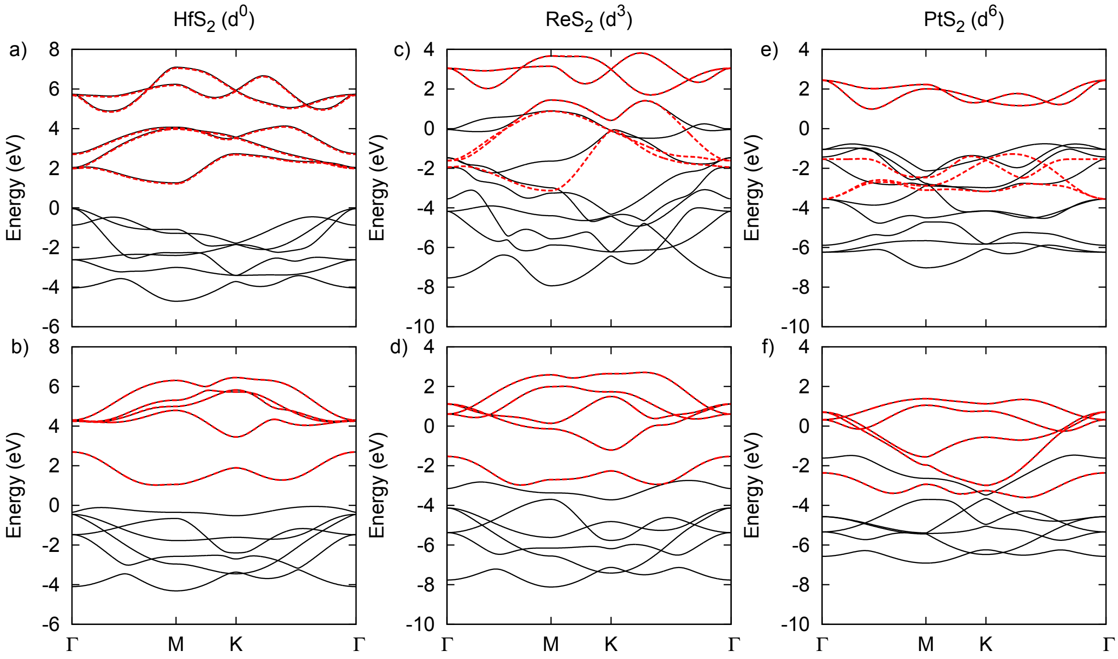

Figure 3.11 – Band structure calculated from first principles of the transition metal dichalcogenides (a)-(b) $1T$ and $1H$ HfS_2,(c)-(d) $1T$ and $1H$ ReS_2, and (e)-(f) $1T$ and $1H$ PtS_2. The Fermi level is set to zero in all panels. The red dashed lines correspond to the band structure in the 5-band model.

the $1T$ and $1H$ (or $2H$) polymorphs are both observed experimentally and are subject to various forms of charge and spin instabilities [6, 13, 86, 87, 88, 89, 90]. The corresponding energy gains are also of a few tens of meVs, but not necessarily negligible since the energy difference between the ideal $1T$ and $1H$ phases is very small (for TaS_2, the $1H$ phase is 62 meV lower in energy). It has been suggested that in specific cases these subtle effects might change the relative stability of the polymorphs [66, 91]. In that case, it is clear that a more careful treatment of electron correlations is needed to make a precise prediction. While $1H$ TMDs with d^2 occupation are insulating and stable, the corresponding $1T$ materials are also found in nature in a distorted phase with a doubled unit cell [56, 14]. The corresponding distorted $1T$ phase, dubbed $1T'$, has an energy much lower than the ideal $1T$ but is still unfavourable compared to the ideal $1H$ for all materials with the exception of WTe_2 [64, 59]. In Fig. 3.9, we see that for the d^3 case, the $1H$ phase is still slightly lower in energy for $4d$ and $5d$ disulfides. However, the corresponding materials, such as ReS_2, are most stable in a distorted $1T$ phase [58], characterized by a 2×2 unit cell, and a large energy gain upon distortion [60, 61]. The metallic $1H$ phase is not observed experimentally in any of the $n_d = 3$ materials, and is predicted to be thermodynamically unstable [60].

We close this section by stressing that, although it can explain the trends of Fig. 3.9, the ligand field/interorbital hybridization argument does not help understanding the higher stability of the $1T$ phase in the d^0 case. It is expected that the electrostatic repulsion between the chalcogen atoms, that should be minimized in an octahedral coordination, plays an important role [7]. It is

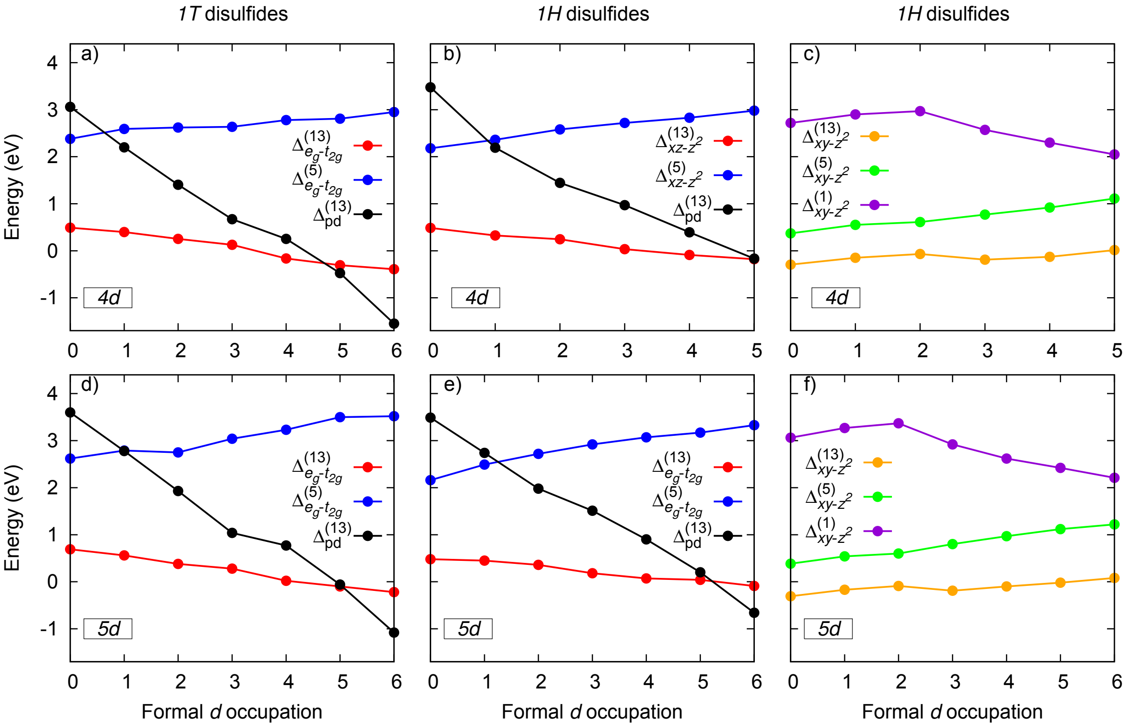

Figure 3.12 – Evolution of the calculated ligand field parameters as a function of the column, in the periodic table, of the transition metal for (a)-(c) $4d$ $1T$ and $1H$ disulfides, and (d)-(f) $5d$ $1T$ and $1H$ disulfides.

also possible that differences in energies of the p bands favour the $1T$ polymorph. Estimating these effects is however outside of the scope of the present work.

3.5 Trends accross the periodic table

So far, we have focused on the specific case of TaS_2. In fact, as we shall discuss, because of the universality of the band structures of TMDs, the reasoning applies to the entire family of materials. As we shall see, the differences between materials are mostly quantitative, i.e. the calculated crystal field parameters vary smoothly across the periodic table and follow trends that can be understood with simple chemical intuition. Reporting all the calculated parameters for all materials would not be particularly illuminating. Therefore, we have chosen a few selected parameters and will discuss the evolution of those parameters in the following.

We first consider the effect of changing the transition metal atom, while keeping the chalcogen to be sulfur. In Fig. 3.11, we show the band structure of a few $5d$ transition metal disulfides in both polymorphs. It is clear that they are qualitatively the same, the main difference being the position of the Fermi level. As the column of the transition metal in the periodic table increases, the energy separation between the d-like and p-like bands decreases. For $n \leq 3$, the two manifolds overlap, so that disentanglement is necessary to derive an effective 5-band

d-only model. In Fig. 3.11, the disentangled d bands are shown with red dashed lines. For the $1T$ case, the disentangled d bands do not match the DFT bands, indicating hybridization with the p-like bands (e.g. avoided crossings). However, the resulting disentangled t_{2g} bands look qualitatively similar in all cases. The narrower bandwidth in the d^6 case (PtS_2) is not related to the entanglement with the p bands, but to a larger lattice constant (see Fig. 3.13). For the $1H$ polymorph, it is the low-energy d'_{z^2} band that overlaps in energy with the p bands. In that case, the resulting disentangled bands match perfectly the DFT bands, meaning the absence of hybridization between these bands. In Fig. 3.11, we have not plotted higher-energy bands. For d^0 disulfides, there is actually some overlap between the top of the d bands and the bottom of the higher-energy bands, so that disentanglement is required to build the d, pd and spd models.

In Fig. 3.12(a) and (c), we plot the calculated $t_{2g} - e_g$ splitting in the 13-band and 5-band models, as well as the charge-transfer energy $\Delta_{pd}^{(13)}$ in the 13-band model, for MS_2, with M belonging to the $4d$ and $5d$ rows of the periodic table. The band structures of the corresponding materials are shown in the appendix, in Sec. 3.8. The charge-transfer energy is defined as the average difference of on-site energies between the d and p Wannier functions, i.e. $\Delta_{pd}^{(13)} = \bar{\epsilon}_d^{(13)} - \bar{\epsilon}_p^{(13)}$. We have taken the 13-band spd model as representative of the bare electrostatic crystal field, so that the disentanglement of the high-energy bands is not necessary.

Figs. 3.12 (a) and (c) show that, for both $4d$ and $5d$ disulfides, the crystal field in the 13-band model decreases as one moves to the right of the periodic table. This trend can be explained with chemical considerations, as the electronegativity increases as one moves to the left, favouring more ionicity and therefore a larger electrostatic contribution to the crystal field. As one can observe in Fig. 3.12, the charge-transfer energy Δ_{pd} decreases as one goes to the right of the periodic table. Again, this trend can be understood from electronegativity considerations and is consistent with the maximal electrostatic contribution to the crystal field for d^0 TMDs. For late-groups TMDs, we observe that the charge-transfer energy is negative. Consistently, the crystal field splitting in the spd model is reversed for those materials. Note that for these late-groups TMDs, because of the small charge-transfer energy, hybridization is so large that the d bands contain actually about 50 percents of ligands' p contribution.

While the electrostatic contribution to the crystal field is expected to decrease with decreasing charge-transfer energy, the opposite trend is anticipated for the ligand field since a small charge-transfer energy favours stronger hybridization. The total ligand field, i.e. that calculated in the 5-band d-only model, is the sum of the bare electrostatic crystal field plus the contribution from hybridization with various ligand states. Hence, the trend for $t_{2g} - e_g$ splitting in the 5-band model is controlled by the competition between opposite trends. For both the $4d$ and $5d$ cases, it appears that the hybridization trend dominates so that the total splitting increases for later-column materials.

For the $1H$ polymorph, as shown in Fig. 3.12(b) and (e), the calculated trends are analogous to those in the $1T$ polymorph and the same logic applies. For both $4d$ and $5d$ disulfides, as

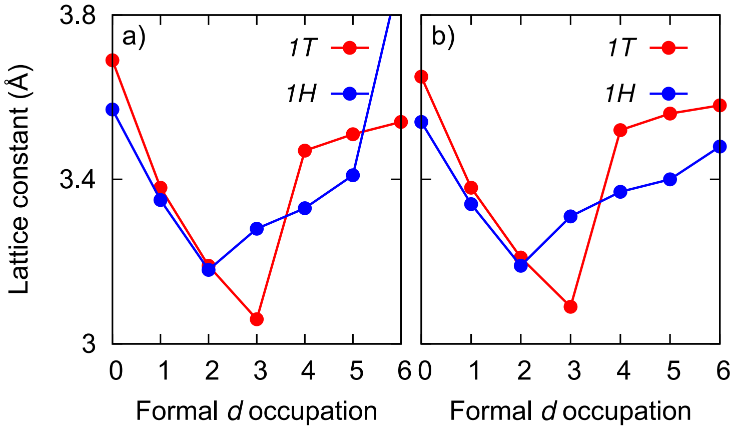

Figure 3.13 – Evolution of the calculated lattice constant as a function of the column, in the periodic table, of the transition metal for (a) $4d$ $1T$ and $1H$ disulfides, and (b) $5d$ $1T$ and $1H$ disulfides.

one moves to the right in the periodic table, the Δ_{xz-z^2} splitting decreases in the spd model and increases in the d model. In the $4d$ case, we have not included $1H$-PdS$_2$ ($4d^6$) in the trend, because, as mentioned above, the electronic structure is qualitatively different.

In order to demonstrate the universality of the argument for the relative stability of the $1T$ and $1H$ phases, we study the Δ_{xy-z^2} splitting for the $4d$ and $5d$ disulfides. In Fig. 3.12(c) and (f), we report the calculated splittings in the 13-band, 5-band and 1-band/4-band models. In the 13-band model, the splitting is consistently small and negative, except for d^6 TMDs because of the inverted charge-transfer energy. In the 5-band model, the splitting increases linearly as n increases due to the larger covalency. On the other hand, in the 1-band model, the lowering of energy of the d'_{z^2} WF is non-monotonous as a function of n. It is interesting to notice that the maximum splitting $\Delta^{(1)}_{xy-z^2}$ corresponds to the maximum filling of the low-energy state while keeping higher-energy states empty (i.e. $n = 2$). This suggests that the lattice relaxes is such a way to maximize the $\Delta^{(1)}_{xy-z^2}$ splitting for the energy gain to be optimal. Indeed, Fig. 3.13 shows that the calculated lattice constant for $1H$ disulfides follows the same trend. The lattice constant is minimal at $n = 2$ in order to increase intersite hoppings, while for the $1T$ case the minimum of the lattice constant is at $n = 3$, corresponding to half-filled t_{2g} bands. It is interesting to note that materials with the largest ligand field splittings $\Delta^{(5)}_{xy-z^2}$ do not exhibit the largest splittings $\Delta^{(1)}_{xy-z^2}$ when interorbital effects are included, confirming that the ligand field alone plays a minor role in stabilizing the $1H$ polymorph in d^1 and d^2 TMDs.

In Fig. 3.14(a)-(c), we show the effect of changing the row of the transition metal atom in the periodic table, by considering $3d^1$ (VS$_2$), $4d^1$ (VS$_2$) and $5d^1$ (TaS$_2$) disulfides. Again, the calculated changes of the charge-transfer energy and the splittings in the spd model follow trends that can be understood from electronegativity considerations. The ligand field contribution to the splitting (i.e. difference of splittings between the spd and d models, not shown here) are almost constant, because the effect of a smaller charge-transfer energy in $3d^1$ materials is

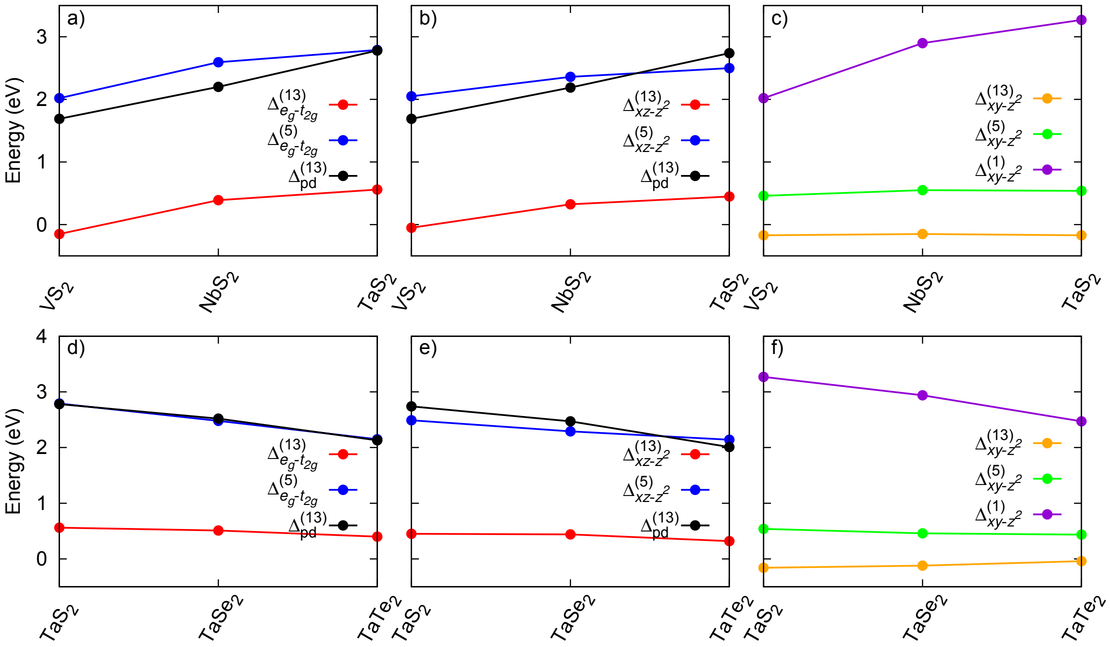

Figure 3.14 – (a-c) Evolution of the calculated ligand field parameters as a function of the row, in the periodic table, of the transition metal for $1T$ and $1H$ d^1 disulfides. (d-f) Evolution of the calculated ligand field parameters as a function of the chalcogen atom (X =S, Se, Te) for $1T$ and $1H$ TaX_2.

compensated by smaller hoppings, since the $3d$ electrons are more localized. In Fig. 3.14 (c), we observe that the ligand field splitting $\Delta^{(5)}_{xz-z^2}$ is nearly constant for the three materials, but that the interorbital effects are larger for the $5d$ case.

In Fig. 3.14 (d)-(f), we summarize the effect of changing the chalcogen atom by considering TaS_2, $TaSe_2$, and $TaTe_2$. Again, the trend for the charge-transfer energy and crystal field splitting in the 13-band model follows what one can anticipate from simple chemistry considerations, as the electronegativity of the chalcogens decreases with increasing the row number in the periodic table, and is therefore the smallest for tellurium. The somewhat smaller charge-transfer energy for $TaTe_2$ does not lead to increased ligand field splittings, because it is compensated by smaller hoppings due to a larger Ta-Te distance ($d = 2.81$ Å). We note the trends for the energy splittings in the 5-band and 13-band models are similar, meaning that the trend for the overall splitting is controlled by the electrostatic effects.

3.6 Relation to previous work

The question of the ligand field stabilization of the $1H$ (or $2H$ in the case of bulk materials) TMDs is an old one that goes back to the early days of research on layered dichalcogenides. Therefore, before closing this paper, we wish to put our study in perspective with previous work.

The ligand field argument was put forward because of the discovery of stable $2H$ d^1 and d^2 TMDs, and still often appears in the recent literature. Originally, there has been controversy regarding the alignement of the singlet state and low-energy $d_{xy}/d_{x^2-y^2}$ doublet [92, 7]. Goodenough [92] suggested a ligand field model with the d_{z^2} singlet higher in energy than the $d_{xy}/d_{x^2-y^2}$ doublet. In his model, the semiconducting character of d^2 TMDs such as MoS_2 is explained by the SOC-induced splitting of the $d_{xy}/d_{x^2-y^2}$ doublet into $m_j = \pm 3/2$ and $m_j = \pm 5/2$ singlets. By considering both a simplified point-charge model and molecular-orbital calculations, Huisman *et al.* [7] suggested that, while electrostatic effects lead to a singlet higher in energy, hybridization with the ligands should reverse the ordering, in agreement with what we have found with our *ab initio* Wannier-function approach. While Huisman *et al.* estimated a ligand field stabilization for the trigonal prismatic coordination and suggested a simple picture for the electronic structure with a low-energy band derived from the d_{z^2} state, Mattheiss [65] showed how the actual band structure is more complex and stressed the role of intersite hopping effects in splitting the d bands into a one-below-four pattern. Mattheiss also estimated the ligand field splitting of the d electrons, for MoS_2 and TaS_2, by fitting the d-like bands to a tight-binding model. Surprisingly, the Δ_{xy-z^2} splitting of 0.04 Ry ($\approx$ 0.544 eV) for trigonal prismatic TaS_2 is in almost perfect agreement with our finding of 0.54 eV. Such agreement is likely accidental, as other features of the reported ligand field diagrams differ significantly from our results. For instance, the Δ_{xz-z^2} splitting of $\sim$ 1.7 eV is significantly smaller than what we have found (2.49 eV). More importantly, the alignment between the $1T$ t_{2g} states (which he discusses in terms of d_{z^2}, d_{xy} and $d_{x^2-y^2}$ states, with z oriented in the out-of-plane direction) and the $2H$ d_{z^2} state is inverted compared to our results. Also, the reported splitting inside the t_{2g} shell ($\sim$ 0.2 eV) is significantly smaller than the value we obtained (0.74 eV) using the same coordinate system.

In this work, by systematically investigating the ligand field splittings across the family of materials, we have come to the conclusion that the ligand field does indeed have a stabilizing effect for $1H$ d^1 and d^2 TMDs, because the singlet d_{z^2} state is lower in energy than the $1T$ t_{2g} states for all materials considered. However, our quantitative calculations also show that this effect is fairly small (compared to the bandwidth or even compared to SOC-induced lifting of degeneracies), so that band structure effects are dominant and lead to a d'_{z^2} Wannier function much lower in energy when interorbital hybridization is taken into account.

3.7 Conclusion

In conclusion, using a modern Wannier-function-based methodology, we have revisited the problem of the relative stability of the $1T$ and $1H$ phases in TMDs by estimating crystal and ligand field parameters for a broad range of materials. Our results show that the ligand field alone plays only a small if any role in determining the most stable phase, because the ligand field splitting of the low-energy triplet in the $1H$ phase is not large, and because the low-energy d_{z^2} singlet state is found to be close in energy to the t_{2g} triplet of the $1T$ phase. This allowed us to conclude that intersite effects are dominant, so that the role of the ligand field is mostly an indirect one: giving rise to low-energy triplets with different orbital character in the two polymorphs. We have also found that, because of the universality of the band structure, the variation of the calculated parameters vary smoothly across the family of materials and follow trends that can be understood using simple chemistry arguments. Finally, our calculations show that the total ligand field splitting of the d-like states in TMDs arises from various contributions, i.e. from electrostatic repulsion effects and from the hybridization with the ligands' s, p and d states, that are all of a similar magnitude. Therefore, simplified models, considering for instance only pd bonding, should not be quantitatively correct.

A remaining question is that of the higher stability of the $1T$ phase for group IV TMDs, that are characterized by empty d bands. Quantifiying the effect of the repulsion between ions in the two coordinations would be an interesting next step in further elucidating the origin of the occurrence of different phases in this family of materials.

3.8 Appendix

3.8.1 Higher-energy bands of $1T$-TaS$_2$

In the main text, we have discussed the effect of including explicitly high-energy states (i.e. tantalum $6s$ and $6p$ states, and sulfur $3d$ states) in the construction of the Wannier functions, without showing the corresponding band structures. In Fig. 3.15, we show the DFT bands including several excited-states bands above the two e_g bands. We see that the bands are highly entangled, so that one cannot simply take a set of isolated bands for wannierization. Fig. 3.15 also shows the bands in the 27-band $spddsp$ model, with the orbital weight of the five d Wannier functions as a color code. The d-like Wannier functions contribute mainly to the five bands close to the Fermi level, which we have referred to as the d bands in the main text. However, it is clear that the d Wannier functions also contribute to the lower-energy and higher-energy bands (especially to the bottom of the p bands), indicating the formation of bonding and antibonding states with the corresponding Wannier functions. In Fig. 3.15, we show, with dashed red lines, the bands obtained with the 13-band spd model. These bands match exactly the DFT bands, except at the top of the e_g bands, because there is a small overlap with the higher-energy bands.

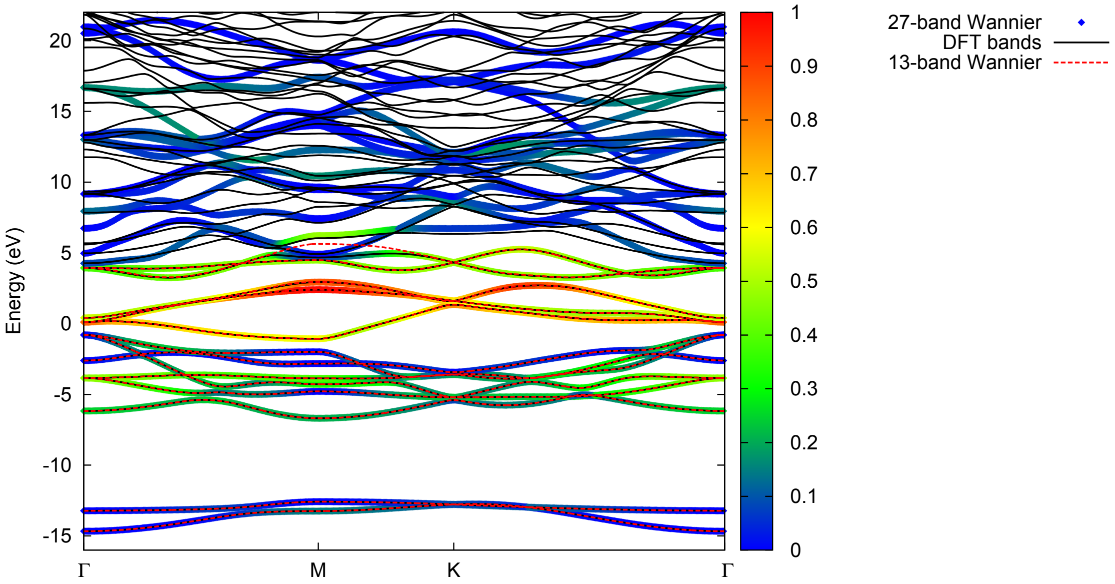

Figure 3.15 – Bands for the 27-band *spddsp* model of monolayer $1T$-TaS$_2$ with the orbital weight of the *d* Wannier functions as a color code. The Fermi level is set to zero. The DFT bands, including the high-energy bands, are shown with continuous black lines. The dashed red lines correspond to the bands of the 13-band *spd* model.

3.8.2 Band structures of the considered materials

In the main text, we have not shown the band structures for all the materials considered. Here, we present the missing band structures, for the 13-band and 5-band models, for both the $1T$ and $1H$ phases. Note that the DFT bands are not explicitly shown, but they match the bands of the 13-bands models up to some minor differences.

$4d$ disulfides trend

In Figs. 3.16 and 3.17, the calculated band structure for the $4d$ transition metal disulfides trends are shown. As for the $5d$ disulfides cases, the p-like and d-like bands are well separated in energy in the d^0-d^2 range. At $n \leq 3$ d electrons, the p and d bands overlap in energy, so that disentanglement is necessary to construct the 5-band models.

PdS$_2$

Fig. 3.18 shows the calculated PBE band structures of monolayer PdS$_2$ in the $1T$ and $1H$ phases. As we have stated in the main text, the relaxed atomic structure of PdS$_2$ in the $1H$ polymorph is characterized by a significant shortening of the S-S distance, leading to a band structure qualitatively different from the other considered materials. On the other hand, the calculated band structure of $1T$-PdS$_2$ is similar to that of other late-group $1T$ TMDs.

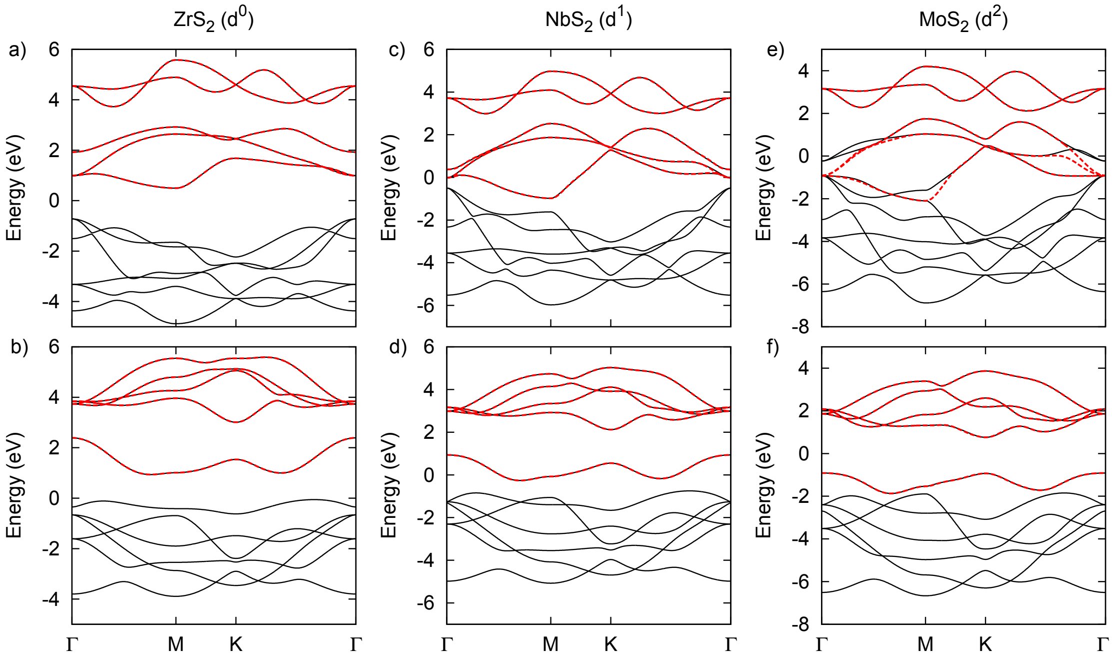

Figure 3.16 – Band structure calculated from first principles for monolayers of (a) $1T$-ZrS$_2$, (b) $1H$-ZrS$_2$, (c) $1T$-NbS$_2$, (d) $1H$-NbS$_2$, (e) $1T$-MoS$_2$ and (f) $1H$-MoS$_2$. The Fermi level is set to zero. Continuous black lines correspond to the 13-band *spd* model and red dashed lines correspond to the 5-band *d* model.

$5d$ disulfides trend

In Fig. 3.19, we show the band structures for the $5d$ disulfides trend that are not presented in the main text (WS$_2$, OsS$_2$ and IrS$_2$).

d^1 disulfides trend

In Fig. 3.20, we present the calculated band structures for the nd^1 trend. In the case of $1T$-VS$_2$, there is some entanglement between the t_{2g} and p bands (i.e. band inversion at the Γ point), explaining why the bands in the 13-band and 5-band models do not match exactly.

TaX$_2$

In Fig. 3.21, band structures for the TaX$_2$ trend are shown. The p and d bands are well separated for TaS$_2$ and TaSe$_2$, but overlap in energy for TaTe$_2$.

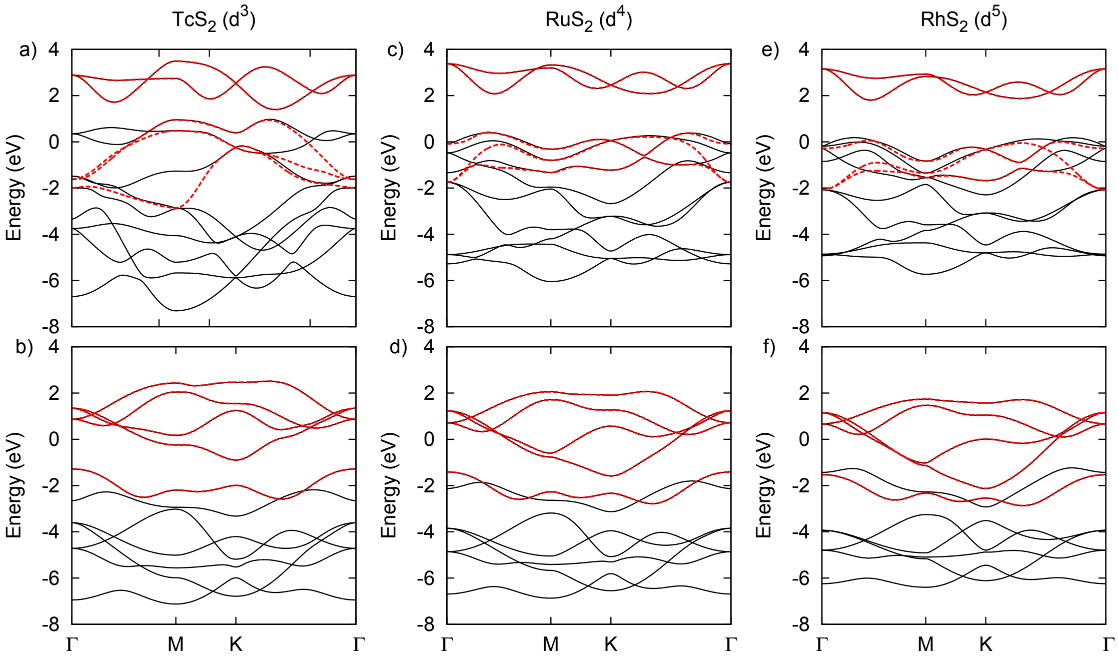

Figure 3.17 – Band structures calculated from first principles for monolayers of (a) 1T-TcS$_2$, (b) 1H-TcS$_2$, (c) 1T-RuS$_2$, (d) 1H-RuS$_2$, (e) 1T-RhS$_2$ and (f) 1H-RhS$_2$. The Fermi level is set to zero. Continuous black lines correspond to the 13-band spd model and red dashed lines correspond to the 5-band d model.

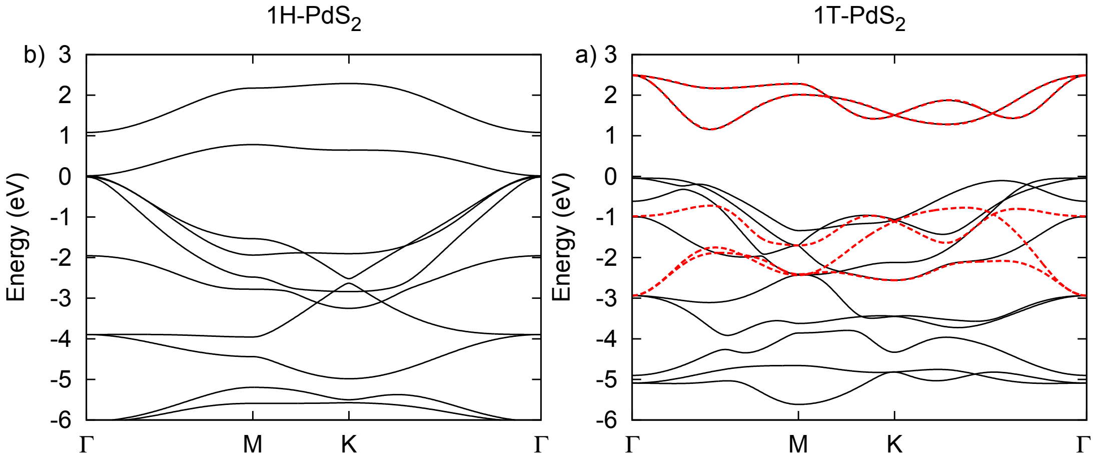

Figure 3.18 – Band structure calculated from first principles for monolayers of (a) 1T-PdS$_2$. The Fermi level is set to zero. Continuous black lines correspond to the 13-band spd model and red dashed lines correspond to the 5-band d model. (b) Calculated band structure for 1H-PdS$_2$.

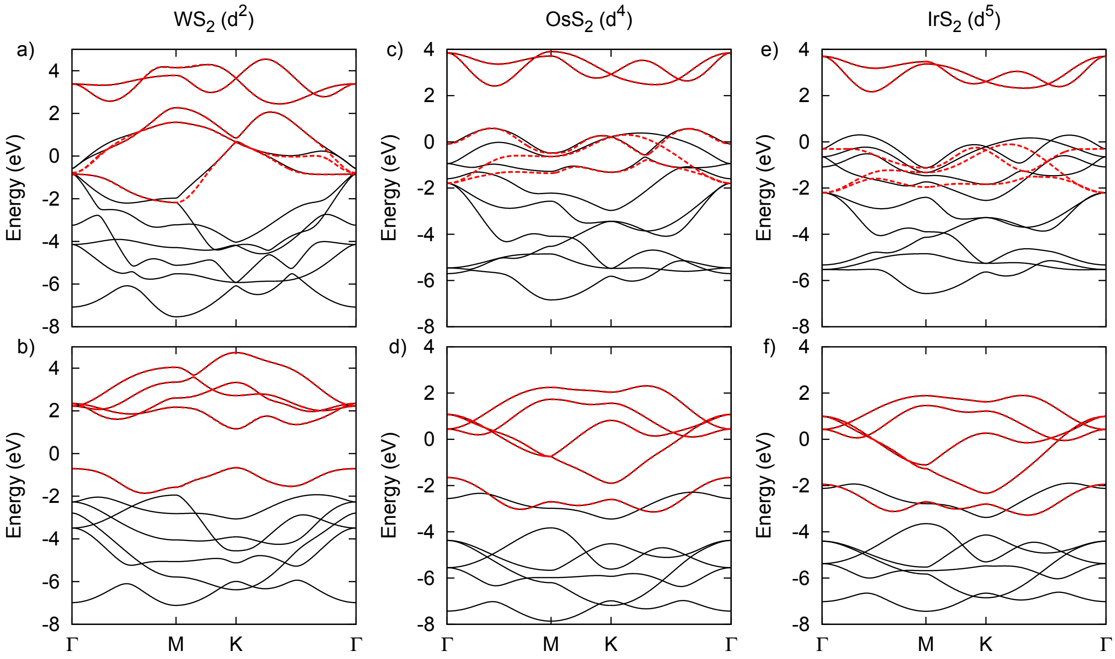

Figure 3.19 – Band structure calculated from first principles for monolyers of (a) $1T$-WS_2, (b) $1H$-WS_2, (c) $1T$-OsS_2, (d) $1H$-OsS_2, (e) $1T$-IrS_2 and (f) $1H$-IrS_2. The Fermi level is set to zero. Continuous black lines correspond to the 13-band *spd* model and red dashed lines correspond to the 5-band *d* model.

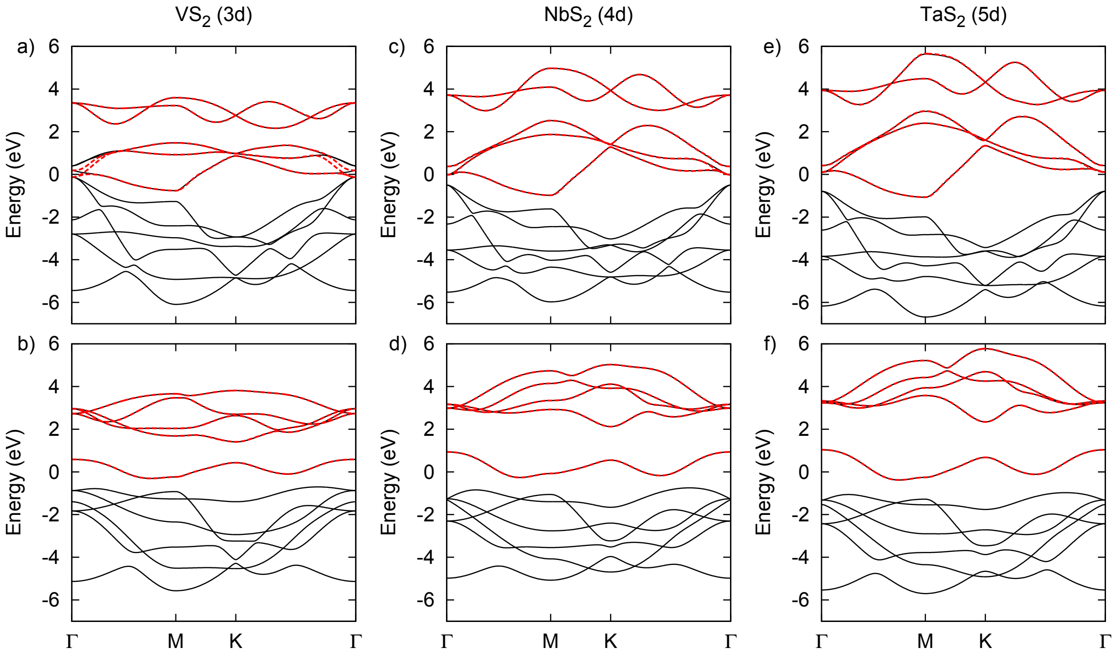

Figure 3.20 – Band structure calculated from first principles for monolayers of (a) 1*T*-VS$_2$, (b) 1*H*-VS$_2$, (c) 1*T*-NbS$_2$, (d) 1*H*-NbS$_2$, (e) 1*T*-TaS$_2$ and (f) 1*H*-TaS$_2$. The Fermi level is set to zero. Continuous black lines correspond to the 13-band *spd* model and red dashed lines correspond to the 5-band *d* model.

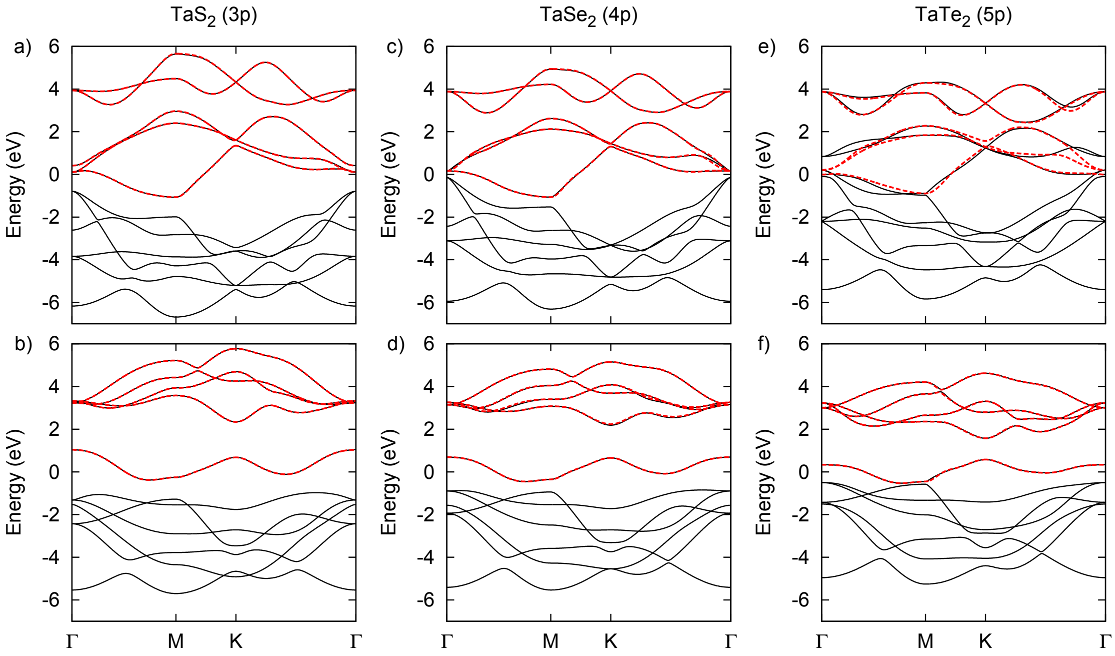

Figure 3.21 – Band structure calculated from first principles for monolayers of (a) $1T$-TaS_2, (b) $1H$-TaS_2, (c) $1T$-$TaSe_2$, (d) $1H$-$TaSe_2$, (e) $1T$-$TaTe_2$ and (f) $1H$-$TaTe_2$. The Fermi level is set to zero. Continuous black lines correspond to the 13-band spd model and red dashed lines correspond to the 5-band d model.

4 A unified picture for lattice instabilities in metallic octahedral transition metal dichalcogenides

Chapter 4 is a pre-print version of a Letter:

Pasquier, Diego; Yazyev, Oleg V. **to be submitted**

Transition metal dichalcogenides in the $1T$ polymorph are subject to a rich variety of periodic lattice distortions, often referred to as charge density waves (CDW) when not too strong. We study from first principles the doping-dependent fermiology and phonon dispersion of three representative single-layer transition metal disulfides with different occupation of the t_{2g} subshell : TaS_2 (t_{2g}^1), WS_2 (t_{2g}^2), and ReS_2 (t_{2g}^3). While strong electron-phonon interactions are at the heart of theses instabilities, we argue that away from half-filling of the t_{2g} subshell, the doping dependence of the calculated CDW wave vector can be explained from simple fermiology arguments, so that a weak-coupling nesting picture is a useful starting point for understanding. On the other hand, when the t_{2g} subshell is closer to half-filling, we show that nesting is irrelevant, while a real-space strong-coupling picture of bonding Wannier functions is more appropriate. We demonstrate that simple bond-counting arguments are qualitatively correct in that case.

Layered transition metal dichalcogenides (TMDs) have been the subject of much attention, partly because of the occurence of a rich variety of lattice instabilities [13, 93, 14, 88, 87, 6]. Two-dimensional TMDs [57, 56] of composition MX_2 consist of a triangular lattice of a transition metal (M=Nb, Ta, Mo, W, etc.), sandwiched between two layers of chalcogen atoms (X= S, Se, Te). Two high-symmetry stackings of the three atomic planes are possible, leading to a coordination of the transition metal atom exhibiting either trigonal antiprismatic (or distorted octahedral) or trigonal prismatic symmetry. The two coordinations lead to two families of polymorphs, referred to as $1T$ and $1H$, respectively.

With a few exceptions, all metallic TMDs experience some form of lattice distortion of various strength [6]. For Group V TMDs, characterized by a formal electronic configuration of the transition metal ion of d^1 [65], the distortions in both polymorph are weak to moderate, and are usually referred to as charge-density-wave (CDW) phases [93]. On the other hand, the distortions in Group VI and VII TMDs with formal occupation of d^2 and and d^3 of the transition metal ion, in the $1T$ polymorph, are much stronger [94, 58].

A Peierls mechanism (i.e. a nesting mechanism) [22, 25] was originally proposed for d^1 TMDs in both polymorphs [13, 93], although this point of view has often been challenged in the more recent literature [95], with several authors arguing that anisotropic momentum-dependant electron-phonon interactions are required to explain the phenomenology [96]. Real-space chemical bonding arguments have also been proposed [14, 97]. Numerous experimental and theoretical studies about CDWs in d^1 TMDs in have been reported in the last few years, for bulk, few-layers and monolayers forms of these materials [98, 99, 100, 101, 8, 102, 103, 104, 105, 106, 107, 108, 109, 110, 97, 111, 79, 112, 91, 113, 114, 115, 116, 117]. It is striking to note that, whereas certain authors mention a well-understood nesting mechanism, others consider nesting as irrelevant. Whereas the $1H$ polymorph of d^2 TMDs is semiconducting and stable, the $1T$ phase is highly unstable and distorts into the metastable $1T'$ phase, with 2×1 periodicity [14, 59].

The $1T'$ phase of d^2 TMDs was recently the focus of intense attention due to its topological properties [15], but the mechanism for the distortion has been less debated. In Ref. [14], Whangbo and Canadell suggested both a hidden nesting mechanism and a complementary chemical

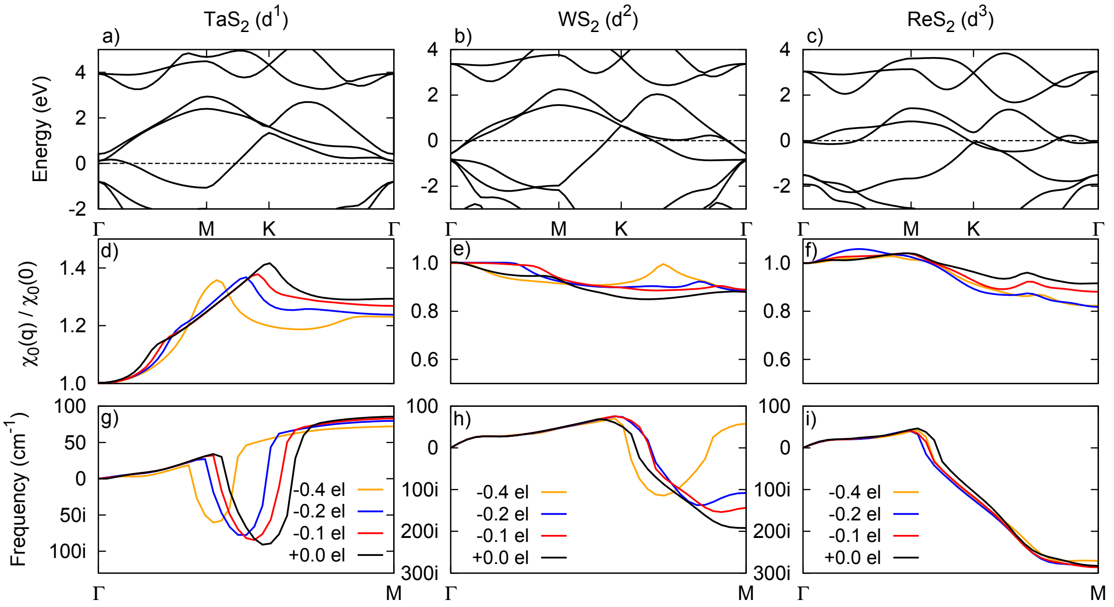

Figure 4.1 – Band structure calculated from first principles for monolayers of (a) $1T$-TaS$_2$, (b) $1T$-WS$_2$, and (c) $1T$-ReS$_2$. The Fermi level is set to zero. Calculated bare static susceptibility along ΓM for (d) $1T$-TaS$_2$, (e) $1T$-WS$_2$, and (f) $1T$-ReS$_2$. Calculated dispersion for the lowest-energy acoustic phonon along ΓM for (g) $1T$-TaS$_2$, (h) $1T$-WS$_2$, and (i) $1T$-ReS$_2$.

bonding picture. A Peierls nesting mechanism was also suggested for certain Mo dichalcogenides [118, 119], based on the inspection of the Fermi surface that reveals pockets apparently nested by the right wave vectors [1]. TMDs with d^3 formal occupation are found in a strongly distorted form of the $1T$ polymorph with 2×2 periodicity (sometimes referred to as $1T''$), with tetramer clusters of transition metal ions forming diamond chains [94, 60]. Kertesz and Hoffman first derived the structure theoretically and stressed the role of the strong interactions between in-plane d_{xy} and $d_{x^2-y^2}$ electrons in driving the distortion [58]. In an attempt to provide a unified theory for the distortions in the TMDs, Whangbo and Canadell *et al.* suggested a complementary picture of both hidden nesting and local chemical bonding [14], as for the $1T'$ phase in d^2 TMDs. More recently, it has been proposed that the $1T''$ phase should be understood as a Peierls instability of the $1T'$ phase, due to the existence in this phase of quasi-1D bands at half-filling for d^3 ions [61].

In this paper, we first study, by means of density functional theory (DFT) calculations, the doping-dependent fermiology and phonon instabilities in $5d$ $1T$ TMDs, taking monolayers of the disulfides TaS$_2$, WS$_2$ and ReS$_2$ as examples. For TaS$_2$, the doping-dependence of the calculated incommensurate CDW (ICDW) wave vector and its direct correspondence with the bare susceptibility provide a clean demonstration of the effect of the fermiology on the ICDW. We therefore argue that at $n \approx 1$ d electron (i.e. TaS$_2$ or heavily hole-doped WS$_2$), a weak-coupling

---

[1] In Ref. [119], the calculated instability for MoS$_2$ is maximal at the K point (corresponding to $\sqrt{3} \times \sqrt{3}$ periodicity) instead of the M point. This is due to the use of a too coarse grid of q-points for Fourier interpolation. The proposed nesting mechanism in Ref. [119] is to explain the instability at the K point.

k-space nesting picture is still a good starting point for understanding, although no sharp divergence is present in the bare susceptibility. On the other hand, we show that for $n \approx 2–3$ d electrons (WS_2 and ReS_2), nesting arguments are not useful, and that a real-space strong-coupling picture of bonding Wannier functions (WFs), splitting strongly the t_{2g} triplet, applies and provides a simple physical picture. This suggests a crossover between weak-coupling and strong-coupling regimes as a function of the electronic filling of the t_{2g} subshell of the transition metal ion.

Fig. 4.1 (a)-(c) shows the electronic structure for the undistorted monolayers of $1T$-TaS_2, $1T$-WS_2 and $1T$-ReS_2, calculated from first principles in the generalized gradient approximation (GGA) of DFT, according to Perdew, Burke, and Erzernhof (PBE) [29]. Details of the first-principles calculations are given in the appendix, in Sec. 4.1. The three bands close to the Fermi level have t_{2g} orbital character, i.e. d_{xy}, d_{xz} and d_{yz}, with the z-axis pointing towards a MS bond. The latter choice of coordinates allows to almost perfectly decouple the two high-energy and three low-energy d orbital degrees of freedom [54], justifying the denomination t_{2g}^1 for TaS_2, t_{2g}^2 for WS_2, and t_{2g}^3 for ReS_2. In edge-sharing geometry (i.e. a transition metal ion shares two ligands with each of its nearest neighbours), t_{2g} electrons have direct overlap with their nearest neigbours, leading to strong electron-phonon interactions [120]. The small qualitative differences of electronic structures between the three materials is due to the band inversion (with sulfur p bands) close to the Γ and M points for WS_2 and ReS_2, occuring because of the smaller charge-transfer energy [54]. While the band inversion is of importance for the topological properties of the $1T'$ phase [15], we shall ignore this point as it does not play an important role for the driving mechanism of the distortions.

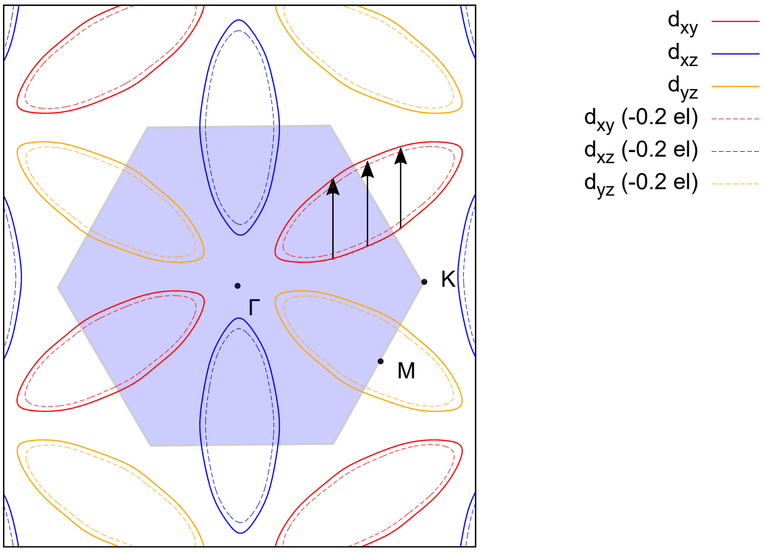

Figure 4.2 – Fermi surface for monolayer $1T$-TaS_2 (undoped and hole-doped). The blue shaded area corresponds to the first Brillouin zone. Nesting vectors for the undoped case have been drawn.

Fig. 4.1 (d)-(i) shows the calculated bare static susceptibilities and phonon dispersions along the

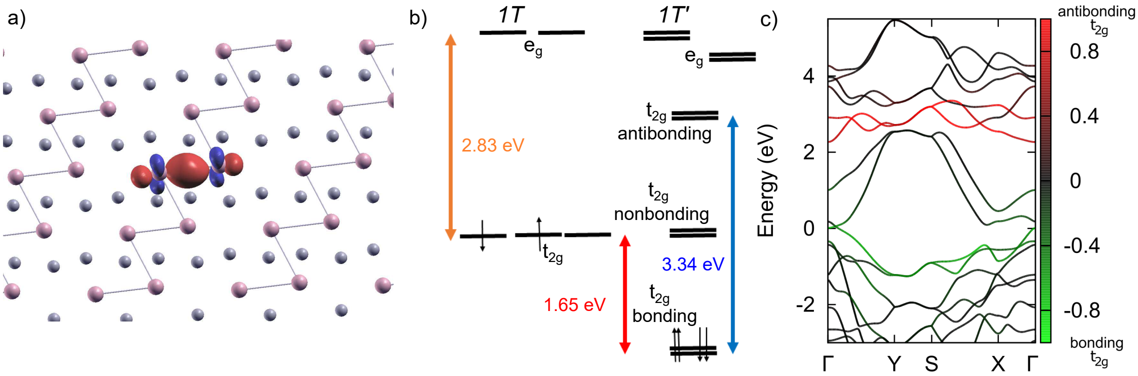

Figure 4.3 – Ball-and-stick representation of the $1T'$ phases of monolayer WS_2. Isovalue plot of a bonding t_{2g} Wannier function. Aligned ligand field and modified ligand field energy diagrams of the $1T$ and $1T'$ phases of monolayer WS_2. Band structure of monolayer $1T'$-WS_2 with orbital weight of bonding and antibonding t_{2g} Wannier functions.
(a) Ball-and-stick representation of the $1T'$ phase of WS_2 with an isovalue plot of one of the two equivalent bonding t_{2g} Wannier functions (WFs). W-W bonds have been drawn to facilitate visualization. Each bond drawn accomodates a bonding t_{2g} WF centered on it. (b) Aligned ligand field and modified ligand field energy diagrams for the $1T$ and $1T'$ phases. (c) Calculated band structure along high-symmetry directions for $1T'$-WS_2. The orbital weight of the bonding and and antibonding t_{2g} WFs is shown as a color code. The Fermi level is set to zero.

ΓM direction, for the three materials and for undoped and hole-doped cases [2]. For the sake of clarity of the figure, we have only shown the lowest-energy accoustic phonon mode, that softens for the three materials in all doping ranges considered. To evaluate the bare susceptibility, we have adopted the commonly-used constant-matrix-elements approximation (CMA), $\chi_0(q) = \frac{1}{N_k}\sum_{k,n,n'} \frac{f_{nk+q}-f_{n'k}}{\epsilon_{nk+q}-\epsilon_{n'k}}$, where N_k is the number of k-points in the discretized Brillouin zone, ϵ_{nk} is the energy of band n at momentum k, and f is the Fermi-Dirac distribution. We have included the three t_{2g}-like bands in the summation, and set the electronic temperature to 300 K. Using the CMA, the absolute value of the susceptibility is sensitive to the number of bands included in the summation [121]. However, we have checked that the location of the peak for TaS_2, as well as the absence of peaks at M for WS_2 and ReS_2, are robust with respect to the number of bands included.

In the theory of weak-coupling charge- and spin-density-wave instabilities, the bare susceptibility is the key quantity, because its enhancement at certain wave vectors favours softening of certain phonon or magnon modes, depending on the dominant microscopic interaction (i.e. electron-phonon or electron-electron) [25]. In the limit of perfect nesting, the bare susceptibility exhibits logarithmic divergences at momentum $2k_F$, leading to instabilities at infinitesimal coupling constant. Perfect nesting is achieved in toy models such as a one-dimensional one-band metal or a two-dimensional one-band metal on the square lattice with nearest-neighbour hopping only. In real materials, perfect nesting would require unrealistic fine-tuning, but nesting-derived instabilities can still occur provided that the interactions are not too weak.

---

[2] For definiteness, we present here the effect of hole doping to understand the effect of doping in these materials. However, the electron-doped case is analogous.

Fig. 4.1 (d) shows that, unlike most 2D metals, the bare susceptibility for $1T$-TaS$_2$ does not achieve its maximum at the Γ point, but at an incommensurate wave vector along the ΓM direction, corresponding to the momentum $q_{\text{ICDW}} \approx 0.28 b_i$ (where b_i are the three primitive lattice vector of the reciprocal lattice) where the calculated phonon softening is maximal. This is due to the approximate nesting properties of the Fermi surface, as shown in Fig. 4.2. Moreover, the calculated peak of the susceptibility, as well as the calculated q_{ICDW}, are found to be sensitive to the exact position of the Fermi level and are both shifted upon doping. Such behaviour is typical of a $2k_F$ effect and clearly shows the effect of the change of the Fermi surface area upon doping on the ICDW. It was found experimentally that Ti-doped bulk $1T$-TaS$_2$ exhibits an ICDW wave vector that decreases with increasing Ti concentration [109, 122]. For two-dimensional materials, one can make use of electrostatic doping to induce charge carriers in a way that closely resembles the rigid Fermi level shift of our calculations. It would therefore be of interest to address experimentally the change of ICDW periodicity in gated TaS$_2$ and other similar materials, in order to shine light on the effect of the Fermi surface. Bulk TaS$_2$ (and possibly the monolayer as well [123]) undergoes a so-called lock-in transition, where the ICDW adopts a periodicity commensurate with the high-symmetry phase, characterized by a commensurate wave vector close the the incommensurate one (corresponding to a $\sqrt{13} \times \sqrt{13}$ periodicity) [124, 125]. We stress that the calculated CDW wave vectors and peaks in the susceptibility correspond to the ICDW periodicity, as the lock-in transition results from anharmonic effects.

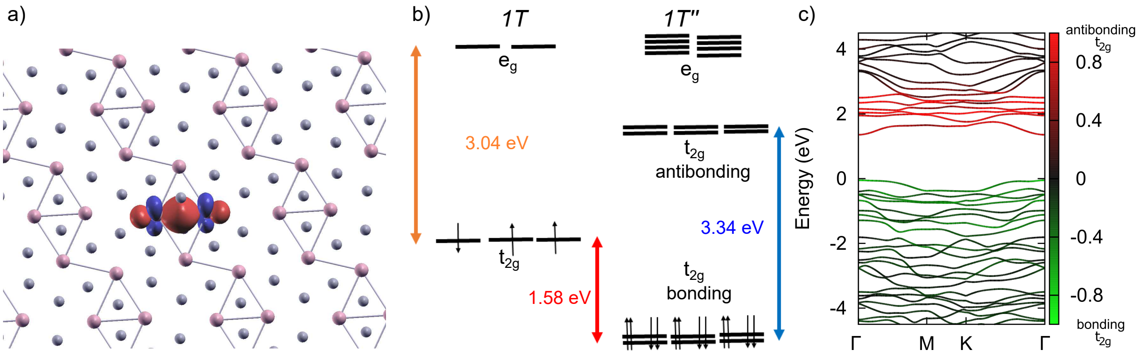

Figure 4.4 – (a) Ball-and-stick representation of the $1T''$ phase of ReS$_2$ with an isovalue plot of one of the bonding t_{2g} WFs. Re-Re bonds have been drawn to facilitate visualization. Each bond drawn accomodates a bonding t_{2g} WF centered on it.(b) aligned ligand field and modified ligand field energy diagrams for the $1T$ and $1T''$ phases. (c) Calculated band structure along high-symmetry directions for $1T''$-ReS$_2$. The orbital weight of the bonding and and antibonding t_{2g} WFs is shown as a color code. The Fermi level is set to zero.

As Fig. 4.1 (e)-(f) shows, the maximum phonon softening for the t_{2g}^2 and t_{2g}^3 cases occurs at the M point, indicating an instability towards doubling the unit cell. We note that, compared to TaS$_2$ the phonon softening occurs over a wider range of momenta and is much stronger. It is also clear that the phonon softening at the M point is not related to any peak in the bare susceptibility calculated in the CMA. Contrary to closely related MoS$_2$ [119] and MoTe$_2$ [118], the Fermi surface of WS_2 does not exhibits nested Fermi pockets, that appear only under electron doping (see the appendix, Sec. 4.1) and are therefore not responsible for the instability. For $n_{t_{2g}} \approx 3$ (ReS_2) the phonon instability is robust against doping, so that the calculated soft phonon mode in not sensitive to the exact number of electrons, contrary to the $n_{t_{2g}} \approx 1$ case. For WS_2, the instability at M is sensitive to hole doping, and disappears at $n_{\mathrm{hole}} \approx 0.4$. For heavily hole-doped WS_2, a behaviour analogous to TaS_2 is recovered, with a calculated incommensurate CDW wave vector associated with an enhancement of the bare susceptibility. Small dicommensurations are already present at lower doping, but it is not clear whether these could be observed experimentally because of anharmonic effects. It is clear that the instability at the M point is not associated with a nesting mechanism, since the calculated susceptibility in at its minimum. Nesting arguments are perturbative ones, so they become less and less relevant as the instability grows stronger, as is the case for WS_2 and ReS_2

From the considerations above, it appears that, contrary to the TaS_2 case, the lattice distortions in the $1T$ d^2 and d^3 TMDs should be better understood from a strong-coupling perspective. As explained e.g. in Ref. [87], the strong-coupling picture of CDWs consist in a real-space picture of chemical bonds. In the following, we shall demonstrate and quantify the bonding mechanism behind the $1T'$ and $1T''$ phases using a Wannier-function approach.

We begin by discussing the $1T'$ phase of d^1 TMDs, taking again WS_2 as a representative example. The relaxed lattice structure is shown in Fig. 4.3. The calculated energy gain upon distortion is large (0.36 eV per formula unit), and the change of the electronic structure is drastic. We have drawn certain W-W bonds as the interatomic distance is significantly reduced (2.78 Å against 3.21 Å in the undistorted $1T$ phase). Such a large shortening of the W-W distance suggests that t_{2g} states pointing toward this bond interact strongly with their nearest neighbour and form bonding and antibonding combinations [14].

To check this hypothesis, we construct Maximally Localized Wannier Functions (MLWFs) [69] by considering two different sets of bands separately to assess the formation of bonding states. Details about the construction of the Wannier functions are provided in the appendix, in Sec. 4.1

Fig. 4.3 (b) shows the aligned ligand field (including electrostatic and pd hybridization effects, as we have discussed in Ref. [54]) and modified ligand field energy diagrams for $1T$ and $1T'$ WS_2, calculated with MLWFs [67]. Our Wannier analysis demonstrates that the main effect of the distortion is to split strongly the t_{2g} states into bonding, nonbonding and antibonding WFs, while the e_g states are weakly affected, although the lifting of degeneracy within the e_g doublet is somewhat increased (0.36 eV against 0.05 eV in the $1T$ phase). In Fig. 4.3 (a), we show an isovalue plot of one of the two equivalent bonding t_{2g} WFs, centered on a W-W bond. Other WFs plots are presented in the appendix, in Sec. 4.1. The on-site energies of the nonbonding t_{2g} states, pointing in the direction of the zigzag chain, are found to be very close (~ 0.1 eV of difference) to these of the undistorted $1T$ phase. On the other hand, the t_{2g} WFs pointing in the W-W bonds directions are split in energy by 3.34 eV. The calculated energy splitting is significantly larger than the half-bandwidth of the undistorted $1T$ phase ($W/2 \approx 2.23$ eV), that one would obtain by simply doubling the unit cell without distortion. This indicates the formation of strong W-W bonds upon translational symmetry breaking. Moreover, Fig. 4.3 (c) shows that the two bonding t_{2g} WFs contribute mainly to the two occupied bands closest to the Fermi level, and are therefore roughly filled by two electrons. The optimal filling of the two strongly bonding WFs explain why the $1T'$ phase is energetically favourable for $n_{t_{2g}} \approx 2$.

Let us now consider the diamond-chain structure (or $1T''$ phase) of d^3 $1T$ TMDs with 2×2 periodicity, with ReS_2 taken as an example. The relaxed structure in the 2×2 supercell, shown in Fig. 4.4 (a), is associated with a large energy gain of 1.12 eV per formula unit compared to the undistorted $1T$ phase. We have drawn Re-Re bonds, because the interatomic distance between the corresponding rhenium atoms is significantly reduced compared to the undistorted phase (2.71−2.9 Å against 3.1 Å in the $1T$ phase).

As for WS_2, we have constructed MLWFs by considering separately two sets of bands, see Sec. 4.1 for details. The aligned ligand field and modified ligand field energy diagrams for the $1T$ and $1T''$ phases are represented in Fig. 4.4 (b). We see that the effect of the distortion is mainly to split strongly the whole t_{2g} subshell into bonding and antibonding states. Indeed, we estimate an energy splitting of 3.34 eV, significantly larger than the half-bandwidth of the undistorted $1T$ phase ($W/2 \approx 2.22$ eV). Since not all the shortened bonds are equal in the $1T''$ phases, there are differences in the on-site energies of the corresponding WFs. The bonding WF on the shortest bond (2.71 Å), plotted in Fig 4.4 (a), is found 0.24 eV lower in energy compared to that centered on the largest bond (2.9 Å). As Fig. 4.4 (c) shows, the bonding t_{2g} WFs contribute mostly to the top of the occupied-bands manifold. We see that in the $1T''$ phase at t_{2g}^3, all the strongly bonding t_{2g} WFs are fully occupied, explaining the stability of this phase.

In our study, we have considered as examples monolayers of transition metal disulfides. However, because of the weak interlayer couplings of the bulk materials, and because of the universality of the electronic structure of TMDs, the reasoning should also apply to other member of this family of materials.

In summary, we report a first-principles study of doping-dependent fermiology and phonon instabilities in two-dimensional $1T$ transition metal disulfides at d^1, d^2, and d^3 occupation of the d shell. When the electron filling of the t_{2g} subshell is far from half-filling, as in TaS_2, we find that the dependence of the ICDW wave vector on the doping levels matches that of the peak of the bare susceptibility. This behaviour is suggestive of a $2k_F$ effect and supports the view that a k-space nesting picture is a good, and necessary, starting point for understanding, even though this point of view has often been challenged. On the other hand, when the electron filling of the t_{2g} subshell is closer to half-filling, as in WS_2 and ReS_2, the behaviour is qualitatively different and nesting appears irrelevant. Indeed, our Wannier-function analysis shows that the effect of the distortions is mainly to split strongly the t_{2g} states, and that simple bond-counting arguments are qualitatively correct. Our study suggests a crossover between weak/moderate-coupling and strong-coupling regimes, tuned by the electronic filling of the t_{2g} orbitals.

4.1 Appendix

4.1.1 Computational methodology

DFT calculations are performed using the QUANTUM ESPRESSO package [40]. We use norm-conserving pseudopotentials from the SG15 library [71, 72, 74], that include the $5s$ and $5p$ semicore states of Ta, W and Re explicitly. A plane-wave cutoff of 60 Ry is used. We employ 24×24 k-points (12×24 and 12×12 for the 2×1 and 2×2 supercells) and a Marzari-Vanderbilt smearing [77] of 10 mRy. We use the cell parameters and atomic positions obtained by relaxing the undoped materials until all the all the Hellman-Feynman forces are smaller than 10^{-4} Ry/Bohr and the pressure is smaller than 0.1 Kbar. We include about 13 Å of vacuum between periodic replicas. We employ the Wannier90 code [78] to obtain Maximally Localized Wannier Functions (MLWFs). Phonon frequencies are calculated within density functional perturbation theory [47]. To plot the phonon dispersion curves, we have calculated the phonons on a 24×24 grid of q-points and used Fourier interpolation. The susceptibility is evaluated on a 100×100 k-points grid with Wannier-interpolated bands. Doping is simulated by changing the total charge of the electron system, with a compensating jellium backround added to ensure the overall charge neutrality of the unit cell.

4.1.2 Wannier functions for $1T'$-WS$_2$

In the main text, we have discussed the splitting of the t_{2g} states in the $1T'$ phase of single-layer WS$_2$, and presented a plot of one of the two equivalent bonding t_{2g} Wannier functions (WFs). Here, we explain how the MLWFs are constructed and present a few extra plots.

Firstly, we derive MLWFs by including 14 occupied bands and the 2 next unoccupied bands. The low-energy Sulfur s-bands and semi-core states bands are excluded. We use the Bloch phases as initial projector and perform the minimization of the spread functional [69]. We obtain 12 p-like WFs centered on the Sulfur atoms, two t_{2g}-like WFs pointing along the chain direction, and two molecular WFs. The molecular WFs are centered on the W-W bonds and clearly resemble bonding combinations of t_{2g} WFs.

Secondly, we wannierize the 6 higher-energy unoccupied bands, yielding 4 e_g-like WFs and 2 antibonding WFs centered on the W-W bonds. Since the bonding and nonbonding t_{2g} WFs in the $1T'$ phase are constructed together with the p WFs, they do not contain explicitly the pd antibonding energy. For proper comparison with the antibonding t_{2g} and e_g WFs, we have therefore added the t_{2g}-p hybridization energy of 1.49 eV, calculated according to the methodology proposed in [67], that we have previously applied to the TMDs in [54].

Note that, in order to obtain the molecular bonding and antibonding WFs centered on the W-W bonds, it is necessary to consider two sets of bands separately, because otherwise the maximal localization procedure would yield atomic-like WFs centered on the ions.

Fig. 4.5 (a) shows an isovalue plot of one of the antibonding WFs. Contrary to the bonding

WF, the antibonding WF contains some weight on the ligands, which reflects the hybridization with the $3p$ states of sulfur atoms. This difference stems from the fact that the p-like bands are excluded when constructing the antibonding t_{2g} and e_g WFs. Fig. 4.5 (b) shows one of the two equivalent nonbonding t_{2g} WF, centered one one of the two W atoms of the unit cell. The nonbonding t_{2g} WFs point towards the direction where the W-W distance is unaffected by the distortion compared to the $1T$ phase. The on-site energy of the nonbonding t_{2g} WFs is very close to that of the t_{2g} WFs of the undistorted $1T$ phase. In Fig. 4.5 (c), we present an isovalue plots of one of the four e_g-like WFs (two per tungsten atom), with $d_{x^2-y^2}$ character.

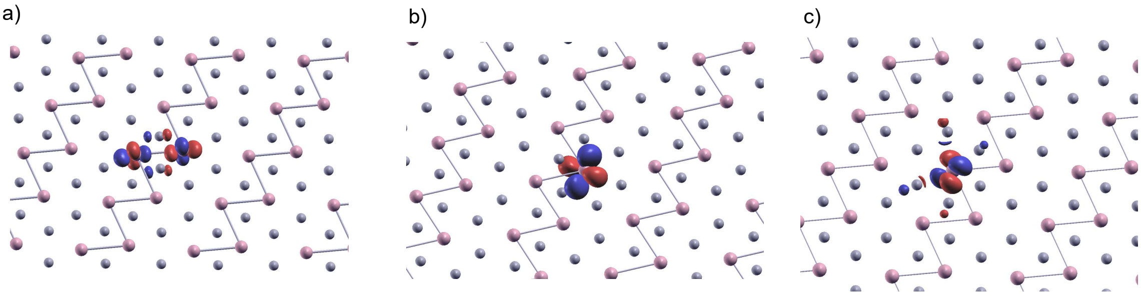

Figure 4.5 – Selected isovalue plots of Wannier functions (WFs) for monolayer $1T'$-WS$_2$. (a) Antibonding t_{2g} WF. (b) Nonbonding t_{2g} WF. (c) e_g WF with $d_{x^2-y^2}$ character.

4.1.3 Wannier functions for $1T''$-ReS$_2$

In the main text, we have discussed the splitting of the t_{2g} subshell of monolayer ReS$_2$ in the $1T''$ phase into six bonding and six antibonding t_{2g} states, and presented a plot of one of the six bonding t_{2g} WFs.

We first consider 30 occupied bands, and obtain 24 p-like WFs centered on the 8 sulfur atoms, and 6 bonding t_{2g} WFs, each bond drawn in Fig. 4.6 (a) accomodating one of them. The lower-energy bands, coming from the sulfur $3s$ states and from the transition metal $5s$ and $5p$ semicore states, are excluded.

We then consider 14 unoccupied conduction bands, and obtain the corresponding 6 antibonding t_{2g} WFs, as well as 8 e_g WFs centered on the 4 Re atoms.

In Fig. 4.6 (a), we show an isovalue plot of the corresponding antibonding t_{2g} WF, centered on the same bond. As for $1T'$-WS$_2$, and for the same reasons, the antibonding t_{2g} WFs contain some weight on the sulfur atoms resembling p orbitals. Contrary to the $1T'$ phase of WS$_2$ for which all the W-W bonds are equivalent, the Re-Re bonds in the $1T''$ phase are not all equal. Fig. 4.6 (b) shows another bonding t_{2g} WF, centered on another nonequivalent Re-Re bond. In Fig. 4.6 (c), we show one of the eight e_g WFs, with d_{z^2} orbital character.

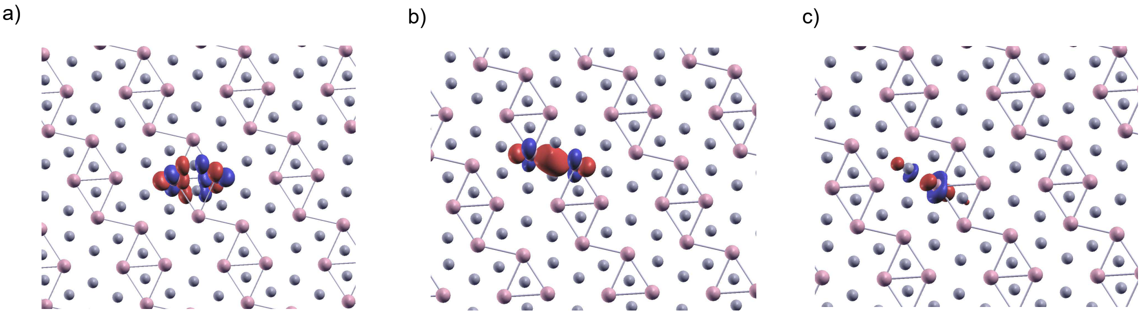

Figure 4.6 – Selected isovalue plots of Wannier functions (WFs) for monolayer $1T''$-ReS$_2$. (a) Antibonding t_{2g} WF. (b) Bonding t_{2g} WF. (c) e_g WF with d_{z^2} character.

4.1.4 Fermi surface for $1T$-WS$_2$

In the main text, we have mentioned the proposed nesting mechanism for the $1T$-to-$1T'$ of certain molybdenum dichalcogenides, based on the inspection of the Fermi surface. In Fig. 4.7 (a) and (b), we show the Fermi surface of monolayer $1T$-WS$_2$ in the undoped and electron-doped cases (with 0.1 extra electron per formula unit). One can see that in the electron-doped case, some extra small electron pockets are present. These pockets are approximately nested by the vector $\Gamma-M$. However, the absence of these pockets in the undoped case shows that the instability at the M point is not related to them. The mechanism for the $1T$-to-$1T'$ instability in the d^2 TMDs must be universal, so the nesting of these pockets cannot account for the distortion in the Mo dichalcogenides either.

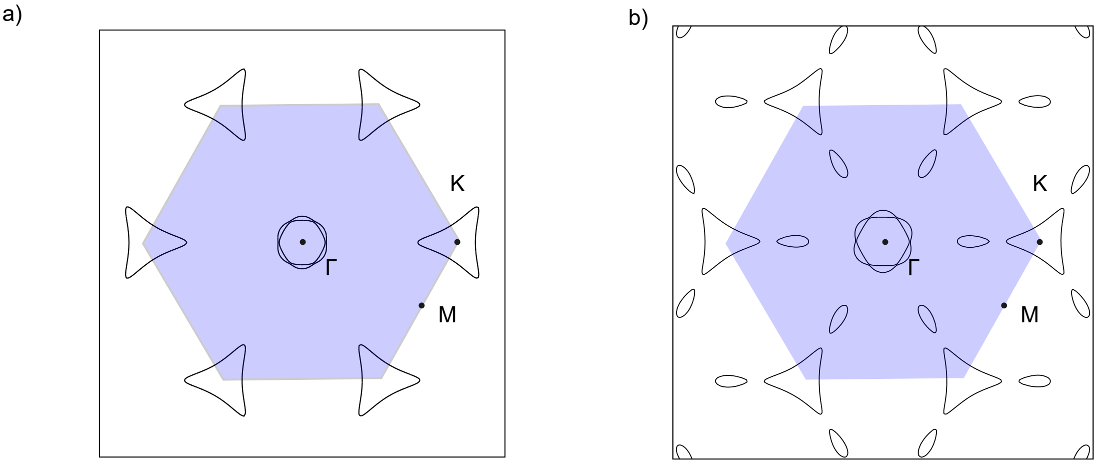

Figure 4.7 – Fermi surface for monolayer $1T$-WS$_2$ for the (a) undoped, and (b) electron-doped (+0.1 electron per formula unit) cases. The blue shaded area corresponds the the first Brillouin zone.

5 Charge density wave phase, Mottness, and ferromagnetism in two-dimensional $1T$-NbSe$_2$

Chapter 5 is a post-print version of a Paper published as:

Pasquier, Diego; Yazyev, Oleg V. *Phys. Rev. B 98 (4), 045114 (2018)* [113]

The recently investigated $1T$-polymorph of monolayer NbSe$_2$ revealed an insulating behaviour suggesting a star-of-David phase with $\sqrt{13} \times \sqrt{13}$ periodicity associated with a Mott insulator, reminiscent of $1T$-TaS$_2$. In this work, we examine this novel two-dimensional material from first principles. We find an instability towards the formation of an incommensurate charge-density-wave (CDW) and establish the star-of-David phase as the most stable commensurate CDW. The mottness in the star-of-David phase is confirmed and studied at various levels of theory: the spin-polarized generalized gradient approximation (GGA) and its extension involving the on-site Coulomb repulsion (GGA+U), as well as the dynamical mean-field theory (DMFT). Finally, we estimate Heisenberg exchange couplings in this material and find a weak nearest-neighbour ferromagnetic coupling, at odds with most Mott insulators. We point out the close resemblance between this star-of-David phase and flat-band ferromagnetism models.

5.1 Introduction

Transition metal dichalcogenides (TMDs) have been extensively studied for their charge-density-wave phases [13, 93, 88, 87], historically being the first materials where the Peierls instability [22] manisfests itself, although this point of view has been frequently challenged in the last few years [95, 96]. More recently, TMDs (for recent reviews see e.g. [56, 6]) have further attracted attention due to their novel topological properties [15, 126], unconventional Ising superconductivity [11, 84, 127, 128], as well as the possibility to thin them down to a single layer [1], leading to a rich family of two-dimensional (2D) materials that includes semiconductors with promising technological applications [57].

TMDs with chemical composition MX_2 are layered materials, each layer consisting of a transition metal (M = Ti, V, Nb, Ta, etc.) forming a triangular lattice sandwiched between two atomic planes of chalcogen atoms (X = S, Se, Te). The local coordination sphere of the transition metal can have either trigonal prismatic or distorted octahedral symmetry, giving rise to two families of polytopes, referred to as $2H$ and $1T$, respectively, where 1 and 2 stand for the number of inequivalent layers in the unit cell for bulk materials. The different coordination environments lead to distinct crystal field splittings of the d-like bands and therefore very different electronic properties [56].

Among all the TMDs, $1T$-TaS$_2$ displays arguably the most complex phase diagram. Indeed, $1T$-TaS$_2$ exhibits a series of structural phase transitions, that involves one second-order and two first-order transitions, upon decreasing temperature [93, 81, 82]. The low-temperature commensurate CDW phase is characterized by the formation of star-of-David clusters of Ta atoms in a $\sqrt{13} \times \sqrt{13}$ supercell associated with the emergence of a narrow band crossing the Fermi level [129, 130], favouring the opening of a Mott correlation gap. Moreover, it has recently been pointed out that no trace of magnetic order is observed down to very low temperatures, indicating a possible quantum spin liquid (QSL) state [16].

Only known so far in the $2H$ phase, $1T$-NbSe$_2$ has recently been successfully synthesized in a monolayer form [17]. Niobium is situated in the same column of the periodic table as Tantalum, which implies that these two transition metal elements are isoelectronic and have formal d-shell populations of $4d^1$ and $5d^1$ in $NbSe_2$ and TaS_2, respectively. It has been found that a superlattice is formed in monolayer $1T$-$NbSe_2$ and that the electronic structure exhibits an insulating energy gap of ~ 0.4 eV, strongly suggesting a phase diagram analogous to $1T$-TaS_2.

The purpose of this paper is to provide a first-principles study of this new material, including the instability of the metallic undistorted $1T$ phase towards a CDW phase, structural properties and different scenarios for the nature of the gap, correlation effects and magnetism. Our work confirms the $\sqrt{13} \times \sqrt{13}$ phase as the most stable commensurate CDW phase as well as the opening of a correlation gap that is to some extent captured even by spin-polarized GGA calculations. GGA+U and DMFT calculations provide further insight and suggest a gap of the charge transfer type. An estimation of Heisenberg exchange couplings surprisingly indicates a ferromagnetic ground state, contrary to what one would expect in a Mott insulator. We suggest that, if confirmed, the ferromagnetism strongly resembles the flat-band ferromagnetism [131, 132, 133, 134, 135, 136, 137, 138] effect in multiband Hubbard models and that this star-of-David phase could be a real material realization of this effect in 2D.

This paper is organized as follows. Section 5.2 briefly describes the computational methodology. In Section 5.3, we study the fermiology and the phonon dispersion of the undistorted $1T$ phase, as well as possible commensurate superlattices. In Sections 5.4 and 5.5, we present an analysis of the electronic structure and magnetism of the $\sqrt{13} \times \sqrt{13}$ phase. Section 5.6 offers conclusions.

5.2 Computational methodology

First-principles density functional theory (DFT) calculations were performed using the QUANTUM ESPRESSO package [40]. The interaction between the valence and core electrons is described by means of ultrasoft pseudopotentials [45] (available from the PSLIBRARY [75, 139]), explicitly including the *s* and *p* semi-core electrons as valence electrons for Nb atoms. The plane-wave cutoffs are set to 60 and 300 Ry for the wave functions and charge density, respectively. The exchange-correlation functional is approximated by the generalized gradient approximation according to Perdew, Burke and Ernzerhof (PBE) [29]. For GGA+U calculations, we adopt the simplified formulation of Cococcioni and de Gironcoli [39], with a Hubbard parameter $U = 3.02$ eV for Nb $4d$ orbitals, calculated from linear response in a supercell of the undistorted $1T$ phase containing 75 atoms. Brillouin zone integration is performed on a $24 \times 24 \times 1$ k-points mesh ($8\times8\times1$ and $6\times6\times1$ for the $\sqrt{13} \times \sqrt{13}$ and 4×4 supercells, respectively) and a Marzari-Vanderbilt smearing [77] of 1 mRy. To simulate the monolayer form, we include approximatively 13 Å of vacuum between periodic replicas. Lattice constants and atomic positions of various phases are determined by fully relaxing the structure at the PBE level until all the Hellmann-Feynman forces are less than 10^{-4} Ry/Bohr. The spin-orbit coupling is not included but its effect is described in the appendix, in Sec. 5.7.

The phonon dispersion is calculated within density functional perturbation theory (DFPT) [47], using a denser mesh of $84 \times 84 \times 1$ k-points and a larger smearing of 5 mRy. To plot the full dispersion, we have calculated the phonons on a 12 × 12 grid of q-points and used Fourier interpolation. In addition, we have computed the dispersion close to the CDW wave vector by performing a DFPT calculation for several points in its vicinity, using different smearings of 10 mRy, 5 mRy and 2.5 mRy and a denser grid of 192 × 192 k-points to ensure convergence of the imaginary frequencies.

Dynamical mean-field theory (DMFT) [140] calculations are performed using the AMULET code [141]. The quantum impurity problem is solved with the continuous-time quantum Monte-Carlo (CT-QMC) algorithm [142] with ten millions QMC steps. The simplified fully localized limit prescription is adopted to account for double counting. The spectrum is obtained with the maximum entropy method.

Maximally localized Wannier functions (MLWF) [69, 68] are obtained using the WANNIER90 code [78]. The susceptibility is calculated on a dense 400 × 400 × 1 k-points grid with Wannier-interpolated bands.

5.3 Charge-density-wave phases

We begin our discussion by determining the structural and electronic properties of the undistorted $1T$ polymorph of monolayer NbSe$_2$. The latter contains three atoms per unit cell and belongs to the symmorphic D^3_{3d} space group. The lattice constant and the Nb−Se distance at the PBE level are $a = 3.49$ Å and $d_{\text{Nb-Se}} = 2.62$ Å, respectively.

The electronic structure and the t$_{2g}$ Fermi surface are shown in Figure 5.1. Since the spin-orbit coupling does not play an important role, we neglect it but briefly describe its effect in the appendix, in Sec. 5.7. The three t$_{2g}$ bands are filled with one electron. The bandwidth is rather large (~ 3 eV), implying that the moderate electron-electron interactions can be neglected at this point. On the other hand, the t$_{2g}$ electrons are prone to form σ-bonds due to their directional character, implying a large coupling to a local bond-stretching phonon. The latter is, to the best of our understanding, responsible for the recurrent occurrence of CDWs in the $1T$ dichalcogenides and lead to stronger distortions when the filling is closer to half-filling, as e.g. in $1T'$-MoS$_2$ [143] or ReS$_2$ [60], in which strong metal-metal bonds are formed. The Fermi surface is typical of group V $1T$ dichalcogenides and displays pseudo-nesting, favouring density wave instabilities with incommensurate wave vectors $\mathbf{Q}_i = Q_{\text{ICDW}}\mathbf{b}_i$, where $\mathbf{b}_i$ ($i = 1, 2, 3$) are the three reciprocal lattice vectors of a triangular lattice and $Q_{\text{ICDW}} \approx 0.25 - 0.33$ [93, 144], depending on material-dependent details of the electronic structure.

Figure 5.2 shows the calculated phonon dispersion curves and bare static susceptibility along the $\Gamma - M$ direction. Neglecting matrix elements, the susceptibility reads

$$\chi_0(q) = \frac{1}{N_k} \sum_{k,n,m} \frac{f(\epsilon_{n,k+q}) - f(\epsilon_{m,k})}{\epsilon_{n,k+q} - \epsilon_{m,k}}\,, \tag{5.1}$$

where $f(\epsilon_{n,k})$ is the Fermi-Dirac distribution and $\epsilon_{n,k}$ are the Kohn-Sham energies. The suscep-

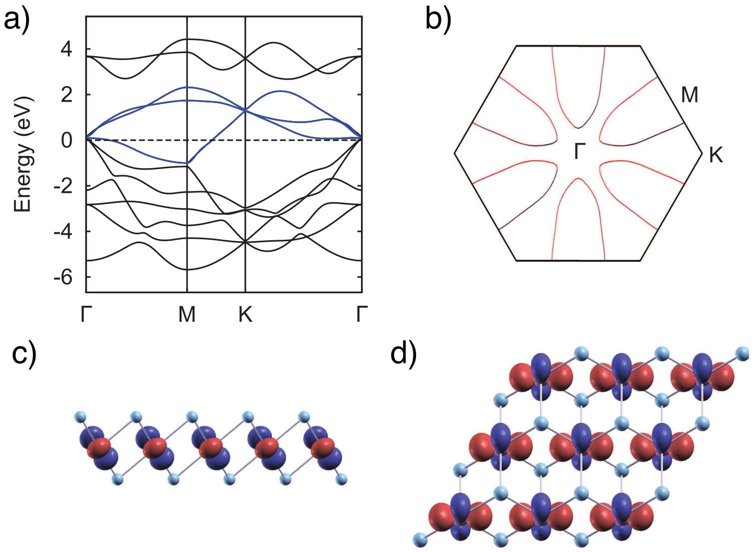

Figure 5.1 – (a) GGA band structure of the undistorted 1*T*-phase of monolayer $NbSe_2$. The t_{2g} bands are emphasized in blue. The dashed line corresponds to the Fermi energy, set to zero. (b) Fermi surface of monolayer $NbSe_2$. (c),(d) Ball-and-stick representation of the undistorted 1*T* phase of monolayer $NbSe_2$ with an isosurface plot of one of the three symmetry-equivalent t_{2g}-like Wannier functions. Selenium atoms are shown in blue.

tibility is proportional to the phonon self-energy in the random phase approximation, favouring soft phonon modes when it is enhanced at a particular wave vector [25]. One can see that the system is unstable against the formation of a CDW with momentum $Q_{\mathrm{ICDW}} \approx 0.26$, corresponding to the maximum of the susceptibility at $T = 300$ K (Fig. 5.2b). At lower temperatures, the maximum is shifted closer to $Q_{\mathrm{ICDW}} = 0.27$. Accordingly, the calculated phonon softening becomes stronger closer to $Q_{\mathrm{ICDW}} = 0.27$ when a smaller smearing is used. We also observe that at $T = 5000$ K the susceptibility is completely flat as the Fermi surface is blurred. The incommensurability of the soft phonon mode and its correlation with the maximum of the susceptibility demonstrate the effect of the fermiology on the CDW (Fig. 5.2c), even if we stress that the latter is possible only in the presence of a rather strong electron-phonon coupling due to imperfect nesting.

As understood by McMillan [124, 125], density waves can further gain energy by adopting a commensurate periodicity characterized by a momentum $\mathbf{Q}_{\mathrm{CCDW}}$ close to $\mathbf{Q}_{\mathrm{ICDW}}$. This can lead to first-order incommensurate-to-commensurate phase transitions (lock-in transitions) as the temperature is lowered. Such transitions come from higher-order terms of the free energy and are therefore not captured by a phonon calculation. The calculated $Q_{\mathrm{ICDW}} \approx 0.26$ suggests either 4×4 or $\sqrt{13} \times \sqrt{13}$ periodicity. In the latter case, each unit cell contains an odd number of electrons and an insulating gap, as observed in experiments, can only come from electron correlations. On the other hand, the 4×4 cell could possibly be a normal band insulator. We have therefore addressed both scenarios by relaxing atomic positions (starting from randomized ones) and lattice vectors in the two supercells.

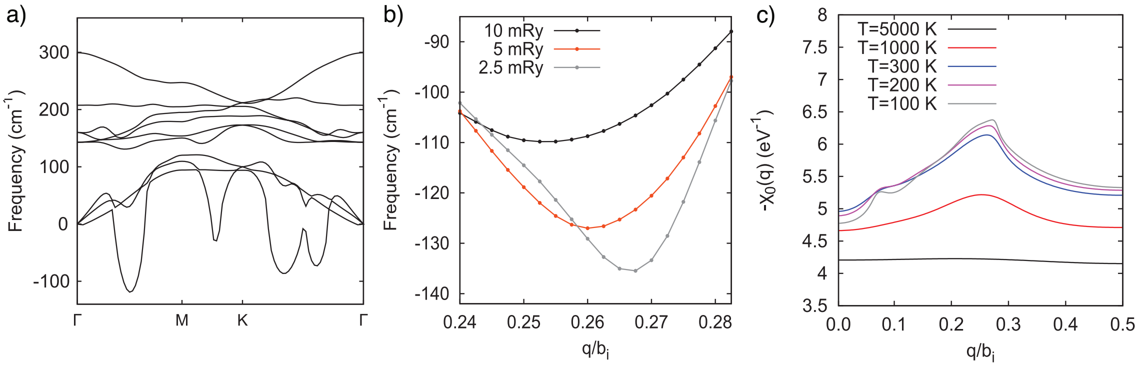

Figure 5.2 – (a) Calculated phonon dispersion for the undistorted 1*T* phase of monolayer NbSe$_2$ obtained by Fourier interpolation. Imaginary frequencies are plotted as negative. (b) Phonon dispersion close to the wave vector of maximum softening with different electronic population smearing values. Each point corresponds to a DFPT calculation. (c) Calculated bare static susceptibility along the $\Gamma - M$ direction at different electronic temperatures.

For the 4 × 4 cell, we obtain an energy gain of 49 meV per NbSe$_2$ formula unit compared to the undistorted 1*T* phase and a magnetically ordered metallic phase (see in Sec. 5.7), whereas for the $\sqrt{13} \times \sqrt{13}$ cell we obtain the star-of-David phase with a larger energy gain of 69 meV/f.u. and a Mott insulator phase (see next section). Another possibility would be that the CDW remains incommensurate down to zero temperature. However, incommensurate CDWs in the dichalcogenides usually have a rather small effect on the electronic structure so that it is unlikely that a gap of ∼ 0.4 eV could be opened.

5.4 Mottness in the Star-of-David phase

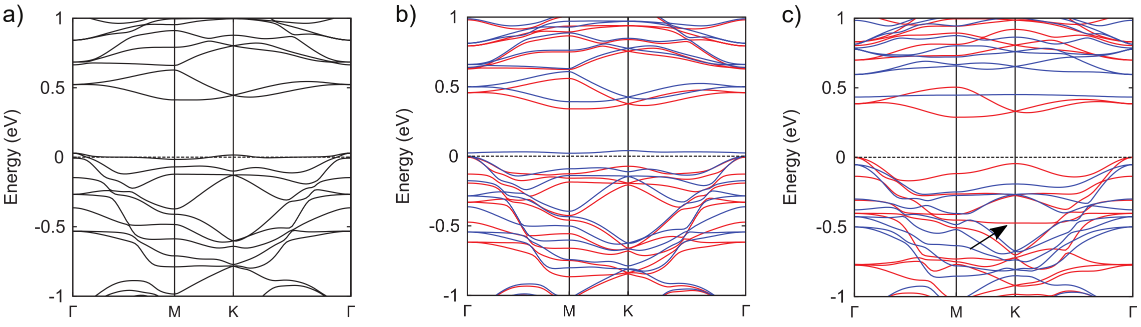

Figure 5.3 – (a) Electronic band structure of the $\sqrt{13} \times \sqrt{13}$ CCDW phase of monolayer NbSe$_2$ obtained from non-spin-polarized GGA calculations. The dashed line corresponds to the Fermi level, set to zero. (b),(c) Electronic band structures obtained from spin-polarized (b) GGA and (c) GGA+*U* ($U = 3.02$ eV) calculations. The arrow marks the flat-like lower Hubbard band. The up and down spin bands are shown in red and blue, respectively.

We now proceed to study the electronic structure of the star-of-David phase at various levels of theory.

As one can see in Figure 5.3a, a very narrow band crossing the Fermi level emerges in the GGA band structure. Spin-polarized GGA already captures some correlation effects and can sometimes describe mottness approximatively (but not in quantitative agreement with experiments [37]), together with a magnetic solution. In Figure 5.3b, we observe a small band gap of ~ 20 meV at the spin-polarized GGA level with a total magnetic moment of 1 μ_B per supercell that contains one David star. The computed gap is clearly too small compared to the experiments, therefore we add an on-site Hubbard repulsion $U = 3.02$ eV for Nb $4d$ orbitals. The calculated gap is now ~ 0.3 eV (Fig. 5.3c), in better agreement with the experimental data. However, the gap appears to between the "uncorrelated" bands rather than between the lower Hubbard band (LHB) and the upper Hubbard band (UHB), as expected in Ref. [17]. We note that the flat LHB and UHB bands can still be distinguished amongst the "uncorrelated" bands in Fig. 5.3c.

To gain further insight, we derive a minimal three-bands (occupied by five electrons) tight-binding model in the basis of maximally localized Wannier functions. We obtain, as can be seen on Figure 5.4, one Wannier function (type I WF) localized at the center of the star with a spread of 22Å^2, giving rise to the narrow band and two Wannier functions (type II WFs, see the appendix in Sec. 5.7), with larger spreads and more weights on the outer Nb atoms of the David stars, hybridizing very weakly with the type I WF. This choice of model allows to capture the bands crossing the Fermi level and to disentangle the narrow "correlated" band, constituting therefore a minimal model to understand the opening of a correlation gap. Treating only the type I WF as correlated with a single variable on-site Hubbard parameter U, we solve the model with DMFT in the paramagnetic phase with an inverse temperature of 40 eV^{-1} ($T \approx 300$ K).

Since the band derived from type I WFs is nearly flat with a bandwidth of ~ 30 meV, it splits into a LHB and a UHB upon any small interaction, explaining why the GGA functional can already capture the gap opening. With a sufficiently large Hubbard U, a gap opens between the type II bands and the UHB (charge transfer insulator) and the orbital population of the type I WF changes from 1.18 in GGA to 1.0 in DMFT. A Hubbard parameter $U \sim 0.9$ eV gives a gap between the type II bands and the UHB consistent with the GGA+U calculation. We note that the spectra obtained from DMFT agree qualitatively with the simpler spin-polarized GGA+U calculations, although the Hubbard parameter used needs to be much smaller. It is clear that the Hubbard parameter in DMFT is only loosely related to that of DFT+U, as it captures the on-site repulsion associated by double-occupancy of a type I WF function rather than an atomic $4d$ orbital. Since this Wannier function is much more spread than an atomic orbital, it is expected that the Hubbard term should be smaller.

We note that in the GGA+U band structure (Fig. 5.3c), while a flat UHB is easily recognizable, the LHB appears to further hybridize with other bands, even if a flat-like band is seen at ~ 0.5 eV below the valence band maximum. This suggests that it would be interesting to compare this minimal three-bands models with more elaborate models containing more bands and to take into account charge self-consistency, but this is beyond the scope of the present work.

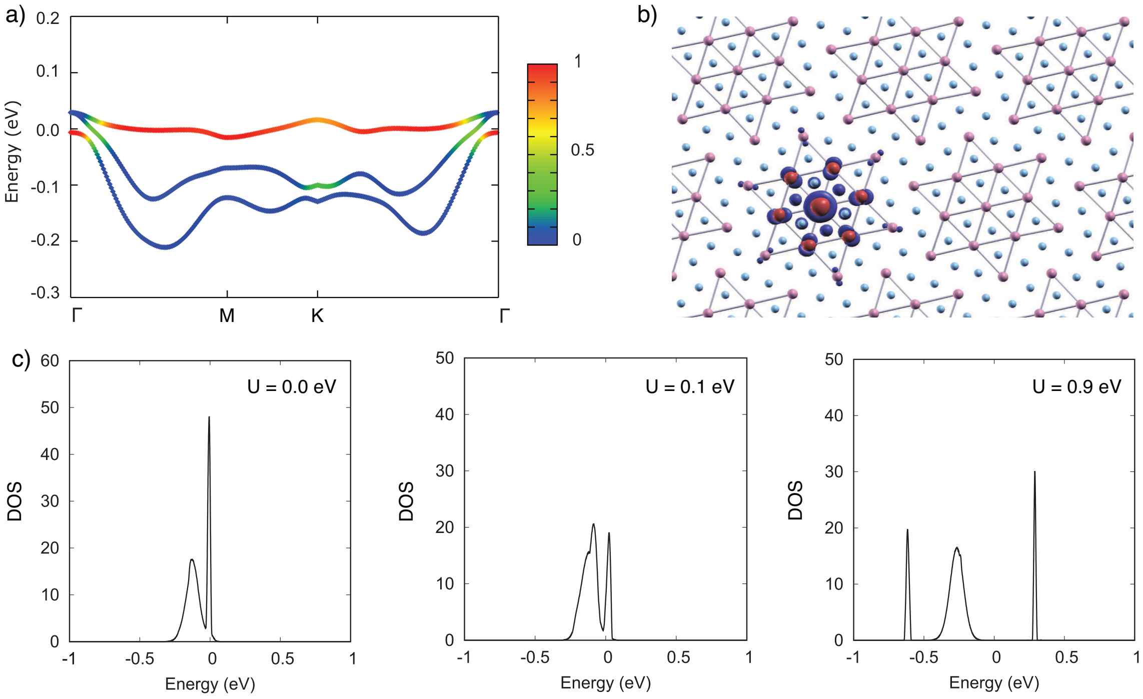

Figure 5.4 – (a) Three-band model chosen for the DMFT calculations with the orbital weight of the type I Wannier function color-coded. (b) Ball-and-stick representation of the star-of-David phase with an isovalue plot of the type I Wannier function. Nb−Nb bonds are drawn to facilitate the visualization. (c) Spectra obtained by analytic continuation of the imaginary-time Green's functions for $U = 0.0$, 0.1 and 0.9 eV. The Fermi energy is set to zero.

Table 5.1 – Calculated nearest-neighbour (J_1) and next-nearest-neighbour (J_2) ferromagnetic exchange couplings in Kelvins.

	J_1 (K)	J_2 (K)
GGA	2.38	0.12
GGA+U	4.77	0.04

5.5 Magnetic phases

In Mott insulators, the low-energy degrees of freedom are localized spins whose interactions lead to long-range magnetic order below a characteristic temperature, unless prevented by strong fluctuations (i.e. a QSL state). It is therefore natural to study the mean-field magnetic solutions obtained from DFT to anticipate the character of magnetic correlations expected in a material.

In Figure 5.5, we present an isovalue plot of the spin polarization density obtained from the GGA+U calculations. While the total magnetic moment is 1 μ_B per star-of-David ($S = 1/2$ Mott insulator), the absolute magnetization is found close to $3\mu_B$/star. This is an effect of the on-site Hubbard repulsion, since in the GGA case, the latter is close to one ($1.19\,\mu_B$/star). In the GGA+U solution, the Nb atom at the center of the star acquires a larger magnetic moment (0.8 against $0.2\,\mu_B$), while its six nearest-neighbours Se atoms, as well as the six outer Nb atoms, acquire small opposite magnetic moments, as can be seen in the spin polarization plot. Our GGA+U solution therefore bears resemblance with ferrimagnetism. However, we stress that the opposite magnetic moments are the consequence of a spin-splitting of the lower bands induced by the magnetic moment associated with the LHB in GGA+U. Focusing on the global properties of the system, we address the question whether the total spins on neighbouring stars couple ferromagnetically or antiferromagnetically [37]. We therefore consider the $2\sqrt{13} \times \sqrt{13}$ and $\sqrt{3}\sqrt{13} \times \sqrt{3}\sqrt{13}$ supercells, containing two and three stars per supercell, respectively. By choosing suitable initial conditions for the spin polarizations, we can ensure the solution of the self-consistent procedure in DFT calculations converges to the one where the total moments of different stars in the supercell are either parallel or anti-parallel. By comparing the total energies of the different configurations, we can then extract effective nearest-neighbour and next-nearest-neighbour Heisenberg exchange couplings J_1 and J_2, as illustrated in Figure 5.5, assuming that further couplings can be neglected. We stress that we are aware that DFT can sometimes give misleading results for magnetic properties, but more accurate wave functions method would be prohibitive for this system and we therefore restrict ourselves to GGA and GGA+U.

The estimated magnetic exchange couplings are reported in Table 5.1. We find a weak nearest-neighbour ferromagnetic coupling and a negligible next-nearest-neighbour coupling. This is rather unexpected since Mott insulators are usually antiferromagnetic, with a few exceptions such as $YTiO_3$ [145] or Ba_2NaOs_6 [146]. We have also verified that introducing the spin-orbit coupling does not affect the sign of the magnetic exchange coupling parameters, even though it gives rise to small anisotropies (see the appendix in Sec. 5.7). A possible scenario for the occurrence of ferromagnetism in multiband Hubbard models is the so-called flat-band ferromagnetism studied by Mielke and Tasaki [131, 132, 133, 134, 135]. Flat-band ferromagnetism can emerge, for instance, on the Kagome lattice with nearest-neighbour hoppings only [147, 148, 149]. While a perfectly flat band requires fine-tuning of the model parameters unlikely to happen in any real material, ferromagnetism is robust against some deviations [138, 148] if the (nearly) flat-band is at half-filling. In the monolayer $1T$-NbSe$_2$ case, the flat-band has some dispersion and overlaps in energy with two other bands. Intuitively, the direct antiferromagnetic exchange is expected to be small because the correlated type I Wannier function are at the center of the stars and have hence small direct hoppings. Therefore, higher-order processes can become dominant and ferromagnetic couplings can be enabled depending on the sign of the different hopping parameters. It is expected that several mechanisms are involved, including the effect of the spin polarization of the “uncorrelated” bands, and that a quantitative model would likely be rather complicated.

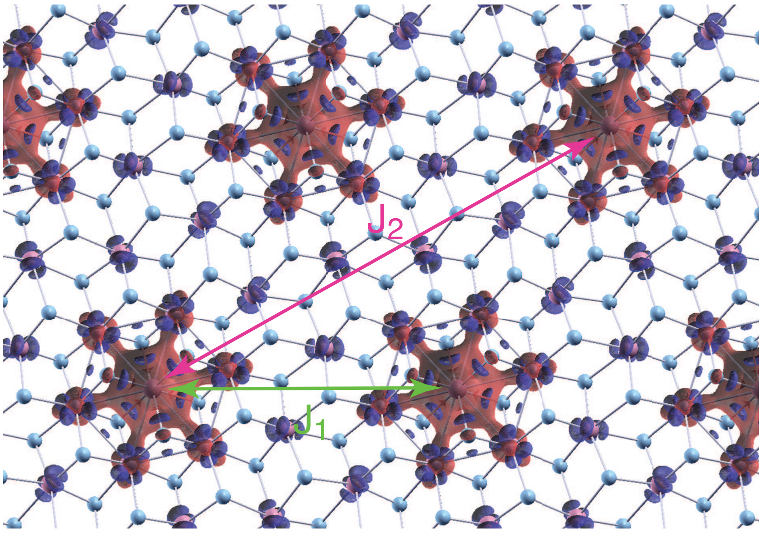

Figure 5.5 – Spin polarization density in monolayer NbSe$_2$ obtained at the GGA+U level in the ferromagnetic phase. A small isovalue of 0.0025 a_0^{-3} was chosen to visualize the opposite polarization on the outer star-of-David atoms. The definitions of nearest-neighbour (J_1) and next-nearest-neighbour (J_2) exchange coupling are indicated.

We point out that monolayer $1T$-TaS$_2$ seems even closer to the ideal flat-band model since the narrow band is well isolated. We have verified that in this system the magnetic exchange coupling is also ferromagnetic at the GGA and GGA+U levels of theory (in agreement with Ref. [150]). We stress that this is not in contradiction with the absence of magnetism observed experimentally, since all experimental studies of magnetism so far were carried out on bulk materials, for which both experiments and calculations suggest significant dispersion between the layers and the existence of a Fermi surface [129, 151, 152, 150]. On the other hand, the ferromagnetic scenario does not seem to agree with the recent proposal of a quasi-2D quantum spin liquid phase in $1T$-TaS$_2$ [16], that could occur, e.g. in a J_1-J_2 antiferromagnetic model on a triangular lattice with $0.08 \leq J_2/J_1 \leq 0.16$ [153]. It would therefore be interesting to address experimentally the possible magnetic ordering in monolayer $1T$-NbSe$_2$ and $1T$-TaS$_2$ at low temperatures.

5.6 Conclusions

In our work, we addressed by means of first-principles calculations monolayer $1T$-NbSe$_2$ that was recently realized experimentally. We found an instability against an incommensurate CDW and established the $\sqrt{13} \times \sqrt{13}$ CCDW with the star-of-David distortion as the most stable phase. Our calculations performed at the level of DFT, DFT+U and DMFT identify this configuration as a Mott insulator. Finally, we suggested the possible existence of ferromagnetic ordering in this star-of-David phase and pointed out the resemblance with the so-called flat-band ferromagnetism scenario. The emergence of the narrow band close to the Fermi level in the CCDW phase leads to exotic physics making these materials unique in the family of the TMDs.

5.7 Appendix

5.7.1 Assessment of the effect of spin-orbit coupling

The spin-orbit coupling (SOC) is responsible for several interesting properties and phenomena in two-dimensional TMDs. In the main text, we have argued that it does not play an important role in the discussed physics and have therefore neglected it. The purpose of this section is to justify this claim.

In Figure 5.6, we show the GGA band structure of the undistorted $1T$-phase monolayer NbSe$_2$ calculated with and without the SOC. The main effect of SOC is a small lifting of band degeneracy at certain points. All bands are doubly degenerate due to inversion symmetry.

Starting from the GGA-relaxed structure in the $\sqrt{13} \times \sqrt{13}$ phase, we have further relaxed atomic positions including the SOC. It was found that the further energy gain is very small (0.12 meV/f.u.), indicating, as expected, that the SOC plays a negligible role in the structural distortion.

In Figure 5.7, we compare non-spin-polarized GGA+SOC and spin-polarized GGA+U+SOC band structures of the $\sqrt{13} \times \sqrt{13}$ phase of monolayer $1T$-NbSe$_2$. One can observe that the SOC splits the two "type II" bands at the Γ point such that a two-band model would be enough to disentangle the narrow band.

To assess the effect of SOC on the magnetic properties, we have used the local density approximation (LDA) in order to avoid issues with the charge density self-consistency inherent to spin-polarized calculations with GGA when SOC is taken into account. Furthermore, we considered only the $2\sqrt{13} \times \sqrt{13}$ supercell.

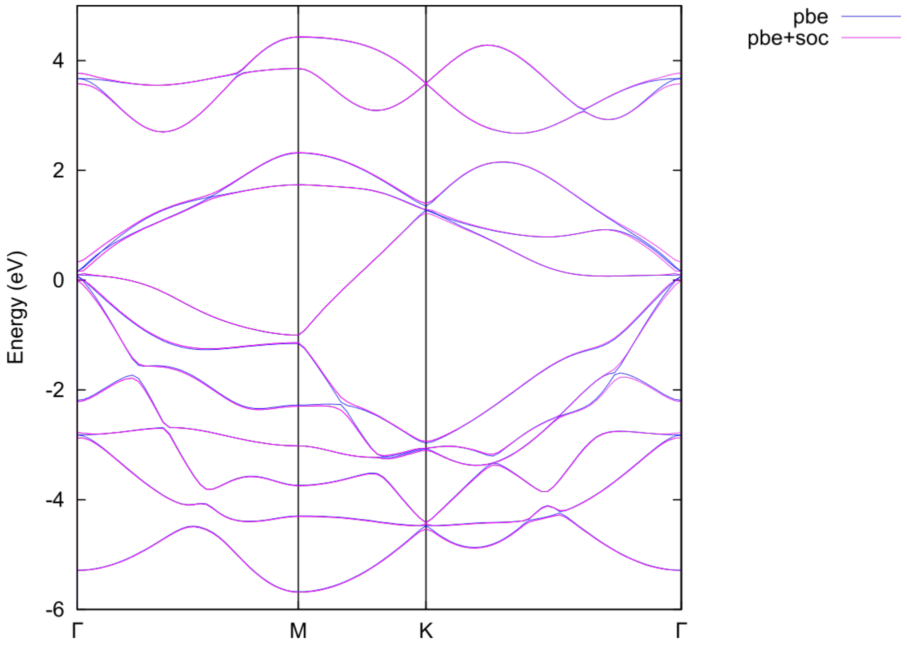

Figure 5.6 – Superimposed band structures of the undistorted monolayer 1T-NbSe$_2$ with and without spin-orbit coupling. The Fermi level is set to zero.

The energy difference between the parallel and antiparallel spin configurations in the $2\sqrt{13}\times\sqrt{13}$ cell is 0.75 meV/star, close to the GGA value of 0.86 meV/star but smaller than the GGA+U value of 1.66 meV/star. Including the spin-orbit coupling, the energy difference is 0.78 meV/star with the local magnetic moments oriented along the out-of-plane z direction. Moreover, we have found that the ferromagnetic solution with magnetic moments in the x-y plane has a total energy further reduced by 0.02 meV compared to the z-direction.

5.7.2 Investigation of the 4×4 CCDW phase

As discussed in the main text, another candidate for commensurate CDW phase in monolayer 1T-NbSe$_2$ has 4×4 periodicity, which turns out to be less favourable energetically compared to the $\sqrt{13}\times\sqrt{13}$ commensurate CDW phase (by 20 meV per NbSe$_2$). In Figure 5.8, we show the calculated GGA+U band structure. Its metallic nature provides further evidence that this phase is not realised in experiments. The calculated distortion pattern displays the formation of clusters of 16 Niobium atoms with an obvious resemblance with the star-of-David distortions in the $\sqrt{13}\times\sqrt{13}$ CCDW phase.

5.7.3 Type II Wannier functions

In the main text, we have introduced a three-band model and presented a plot of the type I Wannier function that gives rise to the narrow band and was treated as correlated in our DMFT calculations. In Figure 5.9, we show plots of the two type II Wannier functions of the model. As

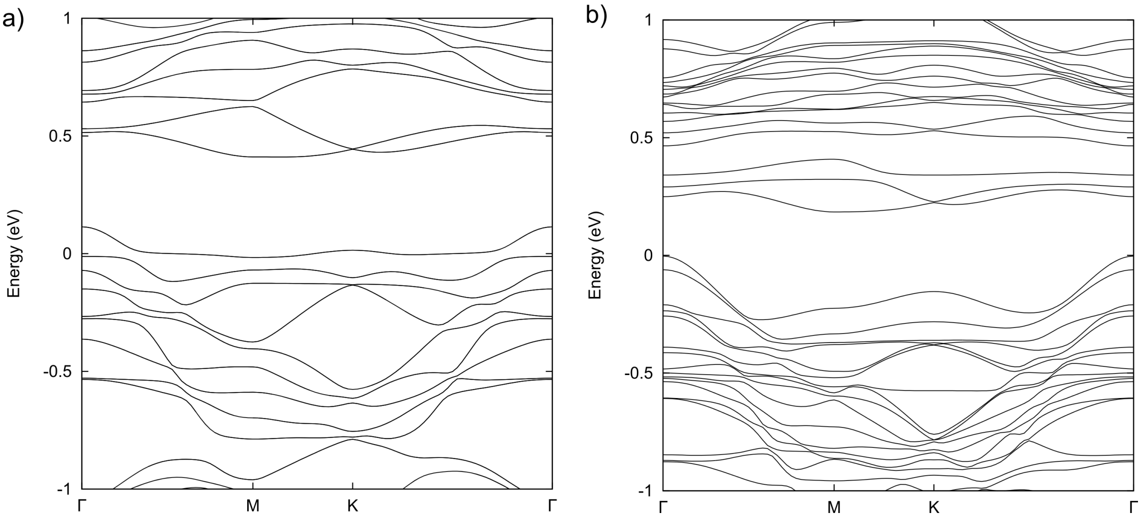

Figure 5.7 – (a) Non-magnetic GGA+SOC band structure in the $\sqrt{13} \times \sqrt{13}$ CCDW phase of monolayer $1T$-NbSe$_2$. The Fermi level is set to zero. (b) Ferromagnetic GGA+U+SOC band structure with $U = 3.02$ eV in the $\sqrt{13} \times \sqrt{13}$ CCDW phase of monolayer $1T$-NbSe$_2$. The valence band maximum is set to zero.

one can see, the two Wannier functions have more weight on outer atoms of the star, which explains why the hopping parameters between neighbouring stars are larger.

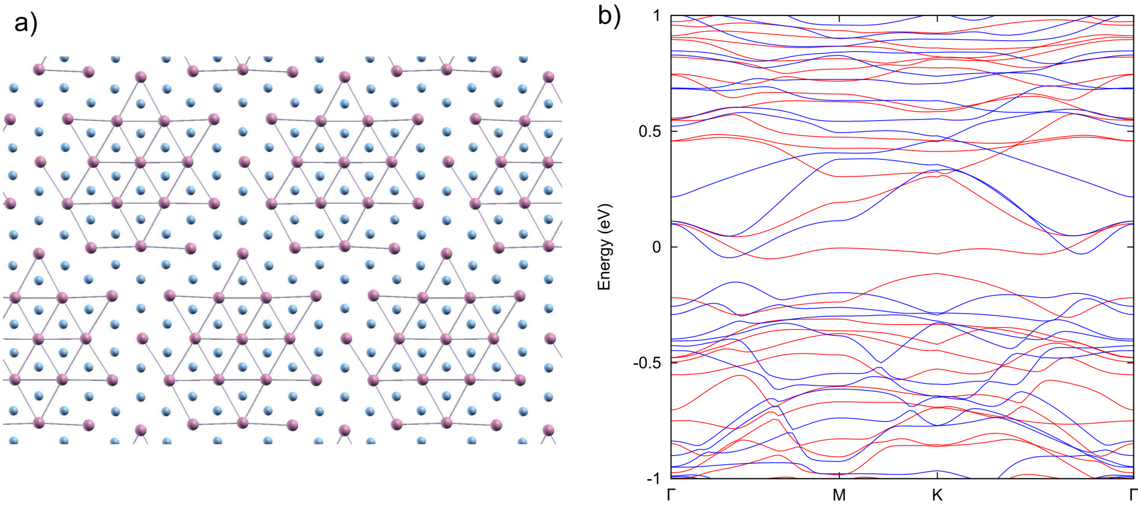

Figure 5.8 – (a) Ball-and-stick representation of the distorted 4 × 4 CCDW phase of monolayer 1T-NbSe$_2$ and (b) the ferromagnetic GGA+U band structure of this phase. The Fermi level is set to zero.

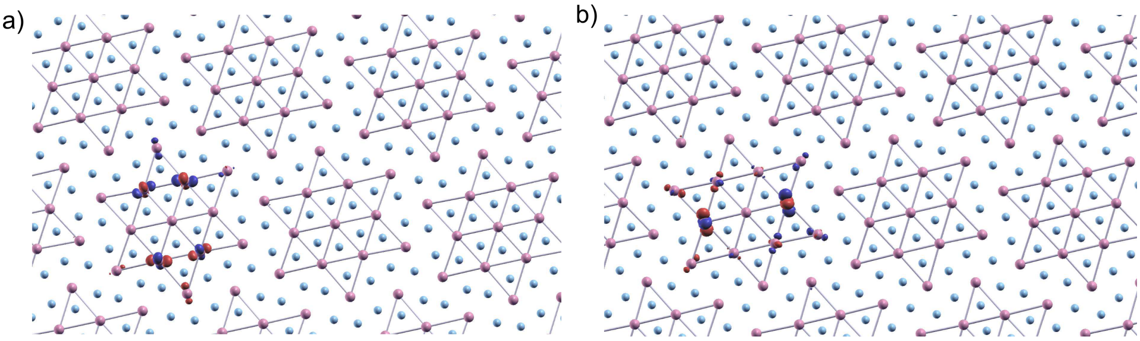

Figure 5.9 – (a,b) Isovalue plots of the two other Wannier functions for the three-band model discussed in the main text.

6 Excitonic effects in two-dimensional $TiSe_2$ from hybrid density functional theory

Chapter 6 is a pre-print version [154] of a Paper submitted to:

Pasquier, Diego; Yazyev, Oleg V. *Phys. Rev. B* **accepted**

Transition metal dichalcogenides (TMDs), whether in bulk or in monolayer form, exhibit a rich variety of charge-density-wave (CDW) phases and stronger periodic lattice distortions. While the actual role of nesting has been under debate, it is well understood that the microscopic interaction responsible for the CDWs is the electron-phonon coupling. The case of $1T$-$TiSe_2$ is however unique in this family in that the normal state above the critical temperature T_{CDW} is characterized by a small quasiparticle bandgap as measured by ARPES, so that no nesting-derived enhancement of the susceptibility is present. It has therefore been argued that the mechanism responsible for this CDW should be different and that this material realizes the excitonic insulator phase proposed by Walter Kohn. On the other hand, it has also been suggested that the whole phase diagram can be explained by a sufficiently strong electron-phonon coupling. In this work, in order to estimate how close this material is to the pure excitonic insulator instability, we quantify the strength of electron-hole interactions by computing the exciton band structure at the level of hybrid density functional theory, focusing on the monolayer. We find that in a certain range of parameters the indirect gap at q_{CDW} is significantly reduced by excitonic effects. We also stress the important role of the spin-orbit coupling in significantly reducing the bandgap. We discuss the consequences of those results regarding the debate on the physical mechanism responsible for this CDW. Based on the dependence of the calculated exciton binding energies as a function of the mixing parameter of hybrid DFT, we conjecture that a necessary condition for a pure excitonic insulator is that its noninteracting electronic structure is metallic.

Transition metal dichalcogenides (TMDs) of chemical formula MX_2 (where M is a transition metal atom and X = S, Se, Te) are materials made up of layers weakly bond together by long-range van der Waals forces, each layer consisting of a triangular lattice of transition metal ions sandwiched between two layers of chalcogen atoms. TMDs are realized in two polymorphs, depending on the coordination sphere of the transition metal atom that can have either trigonal prismatic or antiprismatic symmetry, leading to two families of materials called $2H$ (or $3R$ for bulk materials depending on the stacking sequence) and $1T$, respectively. Periodic lattice distortions, often referred to as charge-density-waves (CDWs) when weak or moderate, are a recurrent phenomenon in both $2H$ and $1T$ metallic TMDs [13, 93, 87, 6]. The CDW phases form rich phase diagrams and result in several interesting phenomena as side-effects such as anomalous metallic behaviour [88], topological phases [15], Anderson localization [155] or Mott insulating phases [82, 129, 17] possibly associated with weak ferromagnetic correlations [113].

$TiSe_2$ is known only in the $1T$ polymorph and belongs to the group IV TMDs, with a formal valence of $3d^0$ for Titanium. The indirect quasiparticle gap in the normal state measured by ARPES is very small (~ 100 meV in the monolayer [156, 157, 85]) leading to the intensely-debated conjecture that the observed CDW with $T_{CDW} \approx 200$ K is a manifestation of the excitonic insulator instability [158, 159, 14, 160, 161, 162, 163, 164], predicted several decades ago [20, 21] but still elusive in real materials (see however for instance Refs. [165, 166, 167]). This instability was originally proposed as a mechanism to interpret lattice distortions in small-gap semiconductors. Such an instability occurs when the electron-hole attraction generates an exciton binding energy larger than the bandgap. Notably, the semimetallic case with small band overlap is also prone to such an instability (see Ref. [21]). This leads to a particle-hole condensate associated with a distortion and breaks the translational symmetry of the crystal if the gap is indirect, due to the finite coupling between charge and lattice degrees of freedom [168]. Another way of viewing the excitonic insulator phase is to notice that the exciton eigenenergies are the poles of the charge susceptibility renormalized by electron-electron interactions, so that a vanishing exciton energy would lead to an enhancement of its low-frequency part and therefore a soft phonon mode for a finite electron-phonon coupling. This is analogous to the original Peierls instability [22] where the *bare* susceptibility is enhanced due to nesting properties [25].

The difference between an excitonic insulator and a purely phonon-driven CDW is ultimately a quantitative one [162], depending on the relative strength of electron-electron and electron-phonon interactions. In any case the observable consequences are the same: a displacement of the atoms from their high-symmetry positions and a redistribution of the spectral weight, meaning that an electronic instability is challenging to disentangle. This problem is reminiscent of that of nematic ordering observed in iron-based superconductors, whose electronic origin remains difficult to demonstrate [169].

Several experiments suggest important electron-electron effects in $\mathrm{TiSe_2}$. In Ref. [161], it was pointed out that the change in the spectral density measured by angle-resolved photoemission spectroscopy (ARPES), proportionally to the atomic displacements, is *large* compared to other dichalcogenides. More recently, using a new spectroscopic technique allowing to measure the momentum-resolved imaginary part of the charge susceptibility [170], Kogar *et al.* have found the evidence for a collective electronic mode softening just above T_{CDW} [171].

On the computational side, Calandra and Mauri first showed that first-principles density functional calculations, within the local density approximation (LDA) and generalized gradient approximation (GGA), correctly predict a soft phonon mode and reproduce a lattice distortion in fairly good agreement with experiments, casting serious doubts on the actual relevance of excitonic effects [172, 173]. The drawback is that the normal state is wrongly predicted to be a metal with a Fermi surface displaying nesting between the hole and electron pockets at Γ and M, leading to an artificial enhancement of the bare susceptibility at q_{CDW}. The insulating character can be recovered with the DFT+U method, but the CDW is then lost as the gap opens [173]. A significant improvement was achieved by Hellgren *et al.*, who successfully reproduced the insulating character and distortion for bulk $\mathrm{TiSe_2}$ within hybrid density functional theory, although the gap in the CDW phase was found to be overestimated [174]. It is unclear to what extent to proposed interpretation, i.e. an exchange-enhancement of the electron-phonon coupling, is distinct from an exciton-phonon driven instability, as the exchange interaction is known to be responsible for excitonic effects as well.

In this work, we provide an estimate of the strength of excitonic effects in this material from first-principles calculations, focusing on the monolayer. The most general way to calculate exciton properties is to solve the Bethe-Salpeter equation with an exchange term screened by the full dielectric matrix, calculated in a preceding GW calculation (GW+BSE) [175]. Since there are

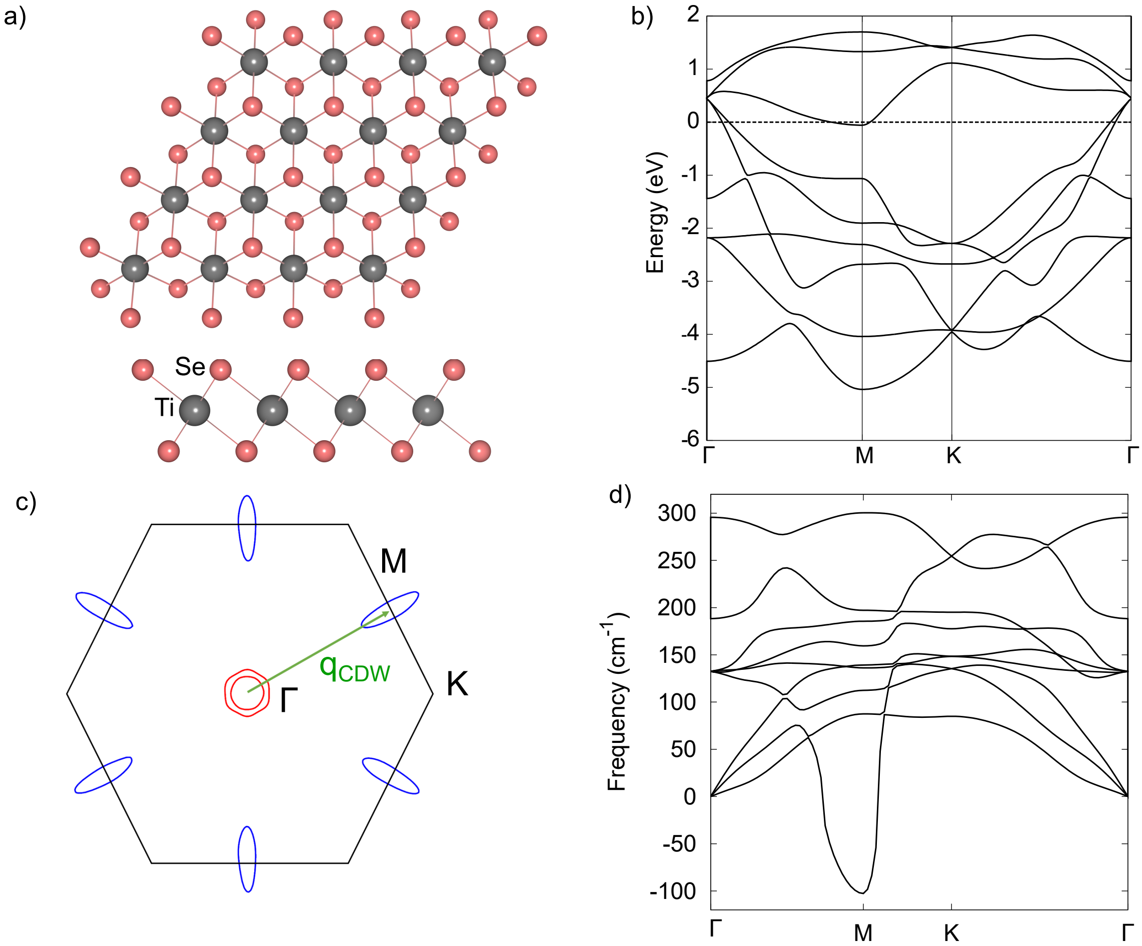

Figure 6.1 – (a) Atomic structure of the $1T$ phase of monolayer TiSe$_2$ (top and side views). (b) Calculated electronic structure of monolayer $1T$-TiSe$_2$ at the PBE level. The dashed line corresponds to the Fermi level, set to zero. (c) Corresponding Fermi surface. The Selenium-derived hole bands are shown in red. The Titanium t$_{2g}$-like electron pockets are shown in blue. The CDW wave vector, shown in green, corresponds to the separation between the hole and electron pockets. (d) Calculated phonon dispersion at the PBE level along the high-symmetry directions. Imaginary frequencies are plotted as negative.

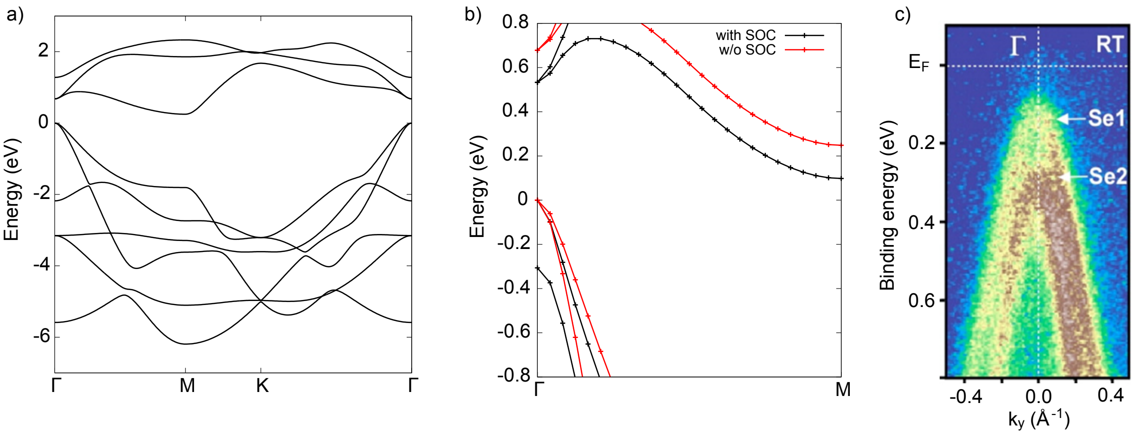

Figure 6.2 – (a) Quasiparticle band structure along the high-symmetry directions using the PBE0 functional and $\alpha = 0.185$. The valence band maximum is set to zero. (b) Calculated band structure, along the Γ-M direction, with and without the spin-orbit coupling. (c) ARPES data from Ref. [85] at room temperature along the Γ-M direction. The insulating character and spin-orbit induced splitting of the bands at the Γ point are visible. Adapted with permission from Ref. [85]. Copyright 2016 American Chemical Society.

no phonons involved in the problem, this should allow to determine whether a purely excitonic instability is indeed present. This is unfortunately very demanding computationally, preventing us from obtaining converged results so far. We have therefore adopted the method proposed by Kresse and collaborators [50], where the bare exchange in the BSE is screened more crudely in the fashion of hybrid functionals. Since this methodology is no longer fully *ab initio*, we have varied the parameters in reasonable ranges and drawn "phase diagrams".

We begin by discussing the structural and electronic properties of the undistorted 1T phase, shown in Fig. 6.1a, at the GGA level, according to Perdew, Burke and Ernzerhof (PBE) [29], using the QUANTUM ESPRESSO package [40] with PAW pseudopotentials [176] from the pslibrary [75, 139]. This phase contains three atoms per unit cell and belongs to the D^3_{3d} space group. The two independent structural parameters, namely the lattice constant a and the Titanium-Selenium distance $d_{\mathrm{Ti-Se}}$, were calculated to be $a = 3.537$ Å and $d_{\mathrm{Ti-Se}} = 2.566$ Å respectively. The calculated PBE lattice constant is in almost perfect agreement with the experimental value of 3.538 Å [177]. This is not really surprising because, whereas the PBE functional is well known to almost systematically overestimate lattice constants, it gives on average slightly underestimated lattice parameters for compounds with open 3d shells [178]. The PBE electronic structure, shown in Fig. 6.1b, is metallic, giving rise to a Fermi surface consisting of two hole pockets around the Γ point and three electron pockets, derived from the Se p and Ti t_{2g} orbitals, respectively. Following the work on bulk TiSe$_2$, several groups have recently reported the phonon softening and lattice distortion predicted by the PBE functional for the monolayer form [179, 180, 181]. In Fig. 6.1d, we show the phonon dispersion, calculated using density functional perturbation theory [47], displaying a soft mode at the M point. Like for the bulk case, the PBE prediction of the instability is associated with a *metallic* electronic structure. Since imaginary frequencies in

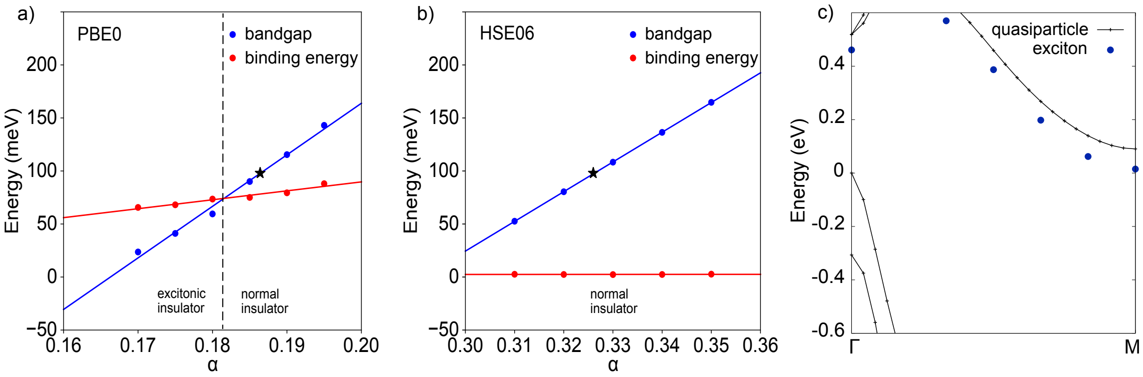

Figure 6.3 – (a) Calculated indirect bandgap and exciton binding energy as a function of the mixing parameter α for the $\mu = 0.0\ \text{Å}^{-1}$ functional (PBE0), including the spin-orbit coupling. The black star corresponds to the ARPES gap estimated at 98 meV in Ref. [156]. The continuous lines drawn correspond to linear fits. The dashed line separates the normal and excitonic insulator phases. (b) Same as in (a), but with $\mu = 0.2\ \text{Å}^{-1}$, corresponding to the HSE06 functional. (c) Band structure including the spin-orbit coupling for the mixing parameter $\alpha = 0.185$. The valence band maximum is set to 0.0 eV. The blue dots correspond to the lowest-energy excitons for a few selected k-points.

phonon calculations tend to be sensitive to the Fermi surface (e.g. charge doping suppresses the instability [180, 181]), it is unclear to what extent this prediction is robust or resulting partially from a cancellation of errors. We note that for TiS_2, PBE calculations predict a metallic electronic structure for both bulk and monolayer forms and phonon softening, with imaginary frequencies in the monolayer case [182]. Experimentally, the bulk material exhibits a gap of ~ 0.7 eV [183] and no sign of CDW or phonon softening were reported. Moreover, it was found experimentally that $TiTe_2$ experiences a CDW transition in the single-layer limit (suppressed already for a bilayer) that is not correctly predicted by the PBE functional [19]. These discrepancies with experiments lead to the questioning of the reliability of semilocal functional for describing the TiX_2 (X = S, Se, Te) materials, suggesting that a more careful treatment of electron-electron interactions is needed.

We now proceed to study the electronic and excitonic properties of monolayer $TiSe_2$ within hybrid density functional theory, using the VASP code [41, 42, 43] with PAW pseudopotentials [176, 184]. For simplicity, the structure in the following calculations is obtained by relaxing the Ti-Se distance using the PBE+SOC functional with the experimental lattice parameter $a = 3.538$ Å. The most popular choices of hybrid functionals are the HSE and PBE0 [31, 35, 36], both mixing the PBE functional with 1/4 of the Hartree-Fock exchange. We have found that those two functionals, including the spin-orbit coupling (SOC), give quantitatively wrong electronic properties for this material. Indeed, the HSE06+SOC functional predicts a *negative* gap of ~ −0.1 eV while the PBE0+SOC functional gives an overestimated gap of ~ 0.4 eV. These two functionals were designed to perform well for medium-gap semiconductors. The mixing parameter α can be interpreted as the inverse of the dielectric constant $1/\epsilon_\infty$ [33], meaning that the chosen mixing parameter should be material-dependent. It has been shown that the PBE0 functional with mixing parameter determined self-consistently gives excellent accuracy in calculating bandgaps [34], justifying *a posteriori* the use of α as a fitting parameter.

In Fig. 6.2a-b, we show the electronic structure with the PBE0 functional with the mixing parameter $\alpha = 0.185$, with and without the spin-orbit coupling. We see that the latter will play a crucial role in the following discussion as it reduces the gap by ~ 0.2 eV. The lifting of degeneracy of the bands at the Γ-point is typical of $1T$ dichalcogenides and is due to the rather strong spin-orbit coupling coming from Selenium atoms. We see in Fig. 6.2c that this feature is also clearly observed in experiments. The calculated band structure now correctly exhibits a small indirect quasiparticle bandgap between the top of the Se p bands at Γ and the bottom of the Ti t_{2g} bands at the M point.

We then solved the Bethe-Salpeter equation at momentum q_{CDW} to obtain the finite-momentum exciton eigenenergies, to see whether the charge-neutral excitation gap is reduced compared to the quasiparticle one. The lowest-energy excitation corresponds to a dark exciton, i.e. with nearly zero oscillator strength, with an energy of 15 meV, meaning an estimated binding energy of 75 meV. Furthermore, we have repeated the following calculations for a series of mixing parameters, effectively varying the screening environment. In Fig. 6.3a, we present the phase diagram obtained for the PBE0 functional as a function of the mixing parameter α, showing the transitions from metal to excitonic insulator to normal insulator as the value is increased. We see that both the computed indirect quasiparticle gap and exciton binding energy at q_{CDW} scale linearly with the mixing parameter α, although with different slopes. We see that for smaller gaps, the two lines are crossing and the lowest-energy exciton has a *negative* energy. By fitting linearly the gap and binding energy, we estimate that the critical mixing parameter for an excitonic insulator is $\alpha_c \approx 0.181$, whereas the optimal parameter giving the ARPES gap of 98 meV is $\alpha_{\mathrm{opt}} \approx 0.186$. We therefore conclude that within this approximation, the system is in proximity to a pure excitonic insulator instability. Note that in Ref. [156], the ARPES measurements were performed with bilayer graphene as a substrate. For a 2D material, the substrate can change the effective screening environment, therefore affecting several properties such as the bandgap. In Ref. [185], scanning tunneling spectroscopy (STS) measurements were performed on $\mathrm{TiSe_2}$ with both highly oriented pyrolytic graphite (HOPG) and $\mathrm{MoS_2}$ as a substrate. It was found that with $\mathrm{MoS_2}$ as a substrate, both the critical temperature (280 K against 230 K) and the STS gap in the CDW phase show an increase compared to the $\mathrm{TiSe_2}$/HOPG system.

In Fig. 6.3c, we plot the lowest-energy exciton for a few selected momenta along the Γ-M direction. One can see that the exciton band is roughly shifted by a constant value compared to the quasiparticle ones, showing that exciton binding energies are weakly momentum-dependent in this case.

We have also considered the effect of the screening parameter μ of the HSE functional [35]. The latter is introduced in order to make the Coulomb potential short-ranged and is advantageous from a computational point of view as it facilitates the convergence with respect to the k-point mesh. We have therefore repeated the previous calculations by using $\mu = 0.2\,\text{Å}^{-1}$, corresponding to the popular HSE06 functional [36]. The effect on both the bandgap and excitonic properties is drastic. Indeed, the effect of the Fock self-energy on the gap is strongly reduced, so that a much larger mixing parameter $\alpha \approx 0.33$ is required to obtain the experimental gap. Moreover, we see in Fig. 6.3b that excitonic effects are also strongly reduced. The exciton binding energies with this functional were calculated to be smaller than 3 meV in the whole range of α considered, so that the system is now far from an excitonic insulator.

To the best of our knowledge, systematic studies of how different hybrid functionals compare and perform for excitonic properties are missing, so it is difficult to tell *a priori* which class of functionals gives the most reliable results, and the optimal choice is expected to be material-dependant. We note that, in Ref. [174], it was found for the bulk material that the $\mu = 0$ functional leads to the strongest enhancement of the electron-phonon couplings. This correlates with our observation that the $\mu = 0$ limit gives the strongest excitonic effects. This is rather natural, since the microscopic interaction leading to these effects is the same. In a diagrammatic series, the dominant term in the BSE is the Fock diagram, which also appears in the expansion for the phonon propagator. Hence, beside comparing our hybrid DFT result with the GW+BSE approach, it would be interesting to study the phonon dispersion with these two classes of functionals, but this is beyond the scope of the present work.

Based on Fig. 6.3a, we make the following observation. In order for the gap and binding energy to cross for some value of the mixing parameter α, it seems necessary that the gap is negative at $\alpha = 0$, since the attraction between electron and holes comes from the screened exchange and grows with α slower than the gap. Therefore, it appears reasonable to conjecture that a necessary condition for a pure excitonic insulator is that its noninteracting band structure, i.e. without Fock self-energy corrections, is metallic. Another observation we make is that while modeling an excitonic phase using hybrid DFT is possible, a severe fine-tuning of the parameters is necessary. We also stress that, as shown e.g. in Refs. [162, 167], a strong electron-hole interaction, even if not large enough to drive a purely electronic instability, reduces the minimal electron-phonon coupling necessary for a distortion to occur. The results obtained with the $\mu = 0$ functional suggest such a scenario, in which both electron-phonon and excitonic interactions play important roles in the CDW phenomena. It is clear that with a sizable electron-phonon coupling, the instability is much more robust and less fine-tuning is required.

In summary, we have investigated electronic properties and excitonic effects in monolayer $TiSe_2$ using hybrid density functional theory. Our calculations have revealed a region in the parameter space where the system is not far from a pure excitonic insulator, which would suggest a hybrid phonon-exciton mechanism. On the other hand, we have also found that the calculated "phase diagram" depends crucially on the choice of the screening length of HSE, with the choice $\mu = 0.2Å^{-1}$ of HSE06 almost reducing to zero the exciton binding energy. The strong dependence of the calculated excitonic properties on the parameters of hybrid DFT prevents us from drawing definite conclusions regarding a pure excitonic instability and we stress the desirability of comparison with higher-level theory. Nevertheless, the observed trends allow us to conjecture that a necessary condition for a pure excitonic insulator is that its noninteracting electronic structure (i.e. at the LDA/GGA level) is metallic.

6.1 Computational details

Density functional perturbation theory calculations are performed with the QUANTUM ESPRESSO package, using PAW pseudopotentials, a plane-wave cutoff of 53 Ry, a k-point mesh of 24×24 points and a Marzari-Vanderbilt smearing of 0.01 Ry. Hybrid functional calculations, including the spin-orbit coupling, are carried out using the VASP code. A dense mesh of 48×48 k-points was employed for the Brillouin zone integration, with a mesh of 24×24 q-points for the evaluation of the exchange operator. The linear tetrahedron method [186] was used. We have included more than 80 Å of vacuum between periodic replicas to ensure converged exciton energies. Two occupied and one unoccupied bands were included when solving the Bethe-Salpeter equation.

7 After-thoughts, conclusions, and outlook

The purpose of this chapter is to summarize the main results obtained in this thesis. The previous chapters of this thesis are published or submitted to peer-reviewed journals and are as a consequence formal in nature. I shall therefore take the opportunity to give a more personal account of how I approached each problem and what the main difficulties have been. As happens often, working on answering a question leads to a plethora of new questions and ideas. I will therefore explain what new developments could be the topic of further study, and speculate on the possible outcomes.

The first purely theoretical question I was assigned to during the course of my PhD was to explain the relative stability of the $1T$ and $1H$ phases of two-dimensional TMDs. This question is an old one that goes back to the early days of research on layered TMDs [7]. The commonly-given answer is to invoke a crystal field argument. However, as pointed out by my supervisor Prof. Yazyev, a quantitative first-principles calculations of crystal field splittings in TMDs is lacking in the literature. Crystal field arguments are attractive due to their simplicity, reducing the complexity of the actual electronic structure to a transparent energy diagram of the d electron states, but their validity relies on quantitative matters.

The most straightforward approach to estimate the strength of the crystal field appeared to be using Wannier functions. Indeed, wannierization allows extracting a tight-binding Hamiltonian from an underlying first-principles density-functional calculation, containing information about crystald field splittings, charge-transfer energies, and hopping parameters. Moreover, as previously suggested, one can take advantage of the high degree of arbitrariness in the construction of Wannier functions in order to estimate how the total splitting emerges, i.e. what the different contributions are and how much they contribute [67]. The calculations revealed that, in both polymorphs, a subtle interplay between electrostatic effects, as well as hybridization effects with the ligands' electronic states, is responsible for the splitting of the d-like states. The band structure of 2D TMDs is universal, so that the differences between different materials belonging to the family are mostly quantitative. By studying a broad range of materials, we have found that the calculated parameters follow simple trends. These trends can be explained using transparent chemical arguments, allowing developing simple intuition.

Regarding the stabilization of the $1H$ phase in d^1 and d^2 materials, it was found that the t_{2g} states of the $1T$ polymorph hybridize more strongly with the ligands' p states compared to the d_{z^2} state of the $1H$ polymorph. This means that ligand field effects do help stabilizing the $1H$ phase for these materials (while electrostatic crystal field effects do not), but the calculated energy differences were found to be rather small. On the other hand, band structure effects, i.e. strong hybridization between the d_{z^2} and $d_{xy}/d_{x^2-y^2}$ bands away from high-symmetry points in the $1H$ polymorphs, can be absorbed in the ligand field energy diagram by using Wannier functions with mixed orbital character. We have found that these interorbital effects are dominant, so that the relative stability of the two polymorphs can only be explained when they are taken into account. The resulting modified ligand field energy diagrams allow explaining in simple terms the trend that d^1 and d^2 TMDs prefer the $1H$ polymorph.

However, the study of the splitting of the d-like electron states is insufficient to explain why d^0 TMDs are most stable in the $1T$ phase. It would be therefore interesting to address the latter problem to obtain a more complete picture. I expect that the Coulomb repulsion between the chalcogen ions is the dominant factor, but it is possible that differences in the p-like bands are also important. Moreover, certain TMDs in the $1T$ polymorph experience strong periodic lattice distortions, which can significantly lower the total energy, therefore influencing the relative stability between the two polymorphs. It is therefore natural that the next topic of this thesis has been devoted to the study of these distortions. Finally, I would like to stress that certain transition metal dichalcogenides are most stable in a crystalline phase that is qualitatively different than the $1T$ and $1H$ phases. These phases have not been studied in the course of this thesis, but it would be interesting to generalize the discussion to these pyrite structures.

The second question I was assigned to was to explain the strong lattice distortions experienced by d^2 and d^3 TMDs in the $1T$ polymorph. Since the distortions in d^2 and d^3 TMDs is much stronger than in the d^1 case, my supervisor rightly expected that the mechanism could be different. It would therefore be interesting to explain how and why they are different. It appeared that the lattice distortions in the d^1 TMDs were not fully understood, the debate being centred mostly on the role of Fermi surface nesting. While nesting was originally thought to explain the transitions, there has been numerous works in the more recent literature stating that nesting is irrelevant. Strikingly, some ofthese papers seemed to contain some misconceptions as to what the Peierls instability actually is. The main misconception is that the Peierls instability is a purely electronic mechanism, meaning that the electronic subsystem spontaneously break the translational symmetry of the lattice, and that the periodic lattice distortion is merely a secondary effect. As expected, all the reported first-principles calculations found the occurrence of a charge density wave only if the ions are allowed to move away from their high-symmetry position. One often-given alternative explanation is that highly momentum-dependent electron-phonon couplings, peaking at the CDW wave vector, should explain the observed occurrence and periodicities of CDWs in TMDs. For d^2 and d^3 TMDs, several proposals have been made to explain the observed distortions, including simple Fermi surface nesting, hidden nesting, and the formation of metal-metal bonds.

In Chapter 4 of this thesis, it was suggested to simulate the effect of charge doping in order the shed light on the effect of the Fermi surface on the periodic lattice distortions in $1T$ TMDs. For $1T$-TaS$_2$, taken as a representative example of d^1 materials, it was found that the results correspond to what one would anticipate from a nesting scenario. Indeed, the calculated doping-dependence of the CDW wave vector corresponds to the doping-dependent peak in the bare susceptibility, and can be anticipated by the change of surface area of the Fermi pockets. This is typical of a $2k_F$ effect, and indicates that weak-coupling nesting arguments are useful for understanding. On the other hand, we have found a qualitatively different behaviour for d^2 and d^3 materials, studied by taking WS$_2$ and ReS$_2$ as representative examples. For these materials, we have argued that a real-space strong-coupling picture of bonding t_{2g} Wannier functions provides the most appropriate description.

The results indicate that the most useful picture to describe the lattice instabilities in these materials is controlled solely by the electron filling of the t_{2g} bands. While it is expected that the interactions are the most effective close to half-filling, it would be interesting to investigate more closely how this crossover takes place. To do so, a microscopic model for the electron-phonon interactions in these materials is likely necessary.

The study of $1T$-NbSe$_2$ from first-principles calculations was mostly driven by recent experimental developments [17]. Indeed, during the course of this thesis, a paper was published, reporting the successful synthesis of a monolayer of NbSe$_2$ in the $1T$ polymorph. Bulk NbSe$_2$ in the trigonal prismatic phase is arguably one of the most studied members of the family of materials, due to its charge-density-wave properties. On the other hand, the $1T$ phase of bulk NbSe$_2$ had never been studied, neither theoretically nor experimentally, for it had never been synthesized. One of the popular axes of research on 2D TMDs is the high tunability of their properties, e.g. by changing the substrate. The successful synthesis of a $1T$-NbSe$_2$ is a rather extreme example of that. Indeed, it was shown that the selective synthesis of the $1T$ or $1H$ phases of NbSe$_2$ can be controlled by changing the temperature of the substrate during growth. The experiments revealed several interesting results. The authors of this remarkable study suggested a scenario analogous to bulk $1T$-TaS$_2$, i.e. a star-of-David phase with $\sqrt{13} \times \sqrt{13}$ periodicity associated with a Mott correlation gap. The results in Chapter 5 of this thesis confirm these speculations, while the other possiblity, i.e. a CCDW phase with a even number of electrons per unit cell and a normal bandgap, was excluded.

An open question about TaS$_2$ is the nature of magnetism in the Mott insulating phase. Indeed, it was pointed out that no trace of magnetic ordering was measured down to zero temperature, indicating a possible quantum spin liquid state [16]. The issue is that all measurements so far were carried out on bulk materials, for which the exact stacking of the layers is unknown. It is unclear whether bulk TaS$_2$ is truly a Mott insulator or an out-of-plane (bad) metal [129]. Hence, the study of magnetism in NbSe$_2$ could help solving this puzzle, because of the similarity between the two materials and because of the availability of single-layer crystals in the star-of-David phase. This puzzle has motivated the estimation of Heisenberg exchange couplings presented in Chapter 5. Since both the nearest-neighbour and next-nearest-neighbour couplings were found to be ferromagnetic, DFT calculations do not point towards a quantum-spin-liquid scenario.

The study of magnetism in the star-of-David phase is an open and difficult problem. Beside addressing experimentally magnetism in monolayer form of these materials, it would be interesting to compare the results of DFT calculations with more involved quantum chemistry methods. It would also be interesting to consider possible non-Heisenberg terms.

The last research project presented in this thesis (in Chapter 6) is devoted to the quantitative calculation of excitonic effects in single-layer $\mathrm{TiSe_2}$, at the level of hybrid density functional theory. While some form of CDW instability in d^1 TMDs is expected, d^0 TMDs are generally semiconducting and stable. The case of $\mathrm{TiSe_2}$ is unique as it experiences an unconventional insulator-to-insulator CDW transition at temperature $T \approx 200$ K [156]. The electronic structure of the normal state above the CDW temperature has led to the fourty-years-old conjecture that this material could be a rare, and possibly unique, real-material realization of the long-sought excitonium phase predicted by Walter Kohn. Several experiments seem suggestive of that [171] but no consensus has been reached so far. On the computational side, it has been shown that DFT calculations with simple exchange-correlation functional (i.e. LDA and GGA) do predict a CDW instability, suggesting that a simpler electron-phonon mechanism is at play. The issue is that the electronic structure with these functional predict a metallic normal state, with a Fermi surface exhibiting nesting properties favouring a soft phonon mode. There are good reasons to believe that the partial agreement obtained with these functionals result from partial cancellation of errors.

Ab initio calculations should make it possible to assess the role of excitonic effects in driving the CDW transition. Indeed, one may pretend that there is no phonon and calculate the quasiparticle and exciton band structures to demonstrate or exclude a possible excitonic insulator phase. The main difficulty for this project was the particularly slow convergence of the excitonic properties with respect to several parameters, leading to a high computational cost. The gold-standard for quasiparticle and excitonic properties, the GW+BSE approach, was particularly difficult to converge properly. Hence, the results presented in this thesis are at a more approximate level of theory : hybrid density functional theory. In hybrid DFT, the screening of the long-range exchange is described by adjustable parameters. It was found in Chapter 6 of this thesis that the conclusions regarding the excitonic phase in $\mathrm{TiSe_2}$ depends sensitively on these parameters. However, there exists a range of parameters (i.e. with the range-separation parameter of HSE set to zero, corresponding to PBE0) for which the material is indeed an excitonic insulator. Interestingly, while this project was ongoing work, a letter reporting the study of electronic and structural properties of bulk $\mathrm{TiSe_2}$ was published, suggesting that the same class of functionals yields the best description [174].

There have been recent successes in accelerating the convergence of GW+BSE calculations [187], so I would expect that it should eventually be possible to provide comparison with our hybrid DFT results. In all unconverged calculations carried out on $\mathrm{TiSe_2}$, I obtained that excitonic effects are stronger at the GW+BSE level compared to PBE0 (the hierarchy being $\epsilon_b^{GW} > \epsilon_b^{PBE0} > \epsilon_b^{HSE06}$). Since I have found that at the level of PBE0, the material is close to a pure excitonic insulator, I would naturally expect that GW does predict an excitonic insulator instability for $TiSe_2$.

Bibliography

[1] K. S. Novoselov, D. Jiang, F. Schedin, T. J. Booth, V. V. Khotkevich, S. V. Morozov, and A. K. Geim, “Two-dimensional atomic crystals,” *Proceedings of the National Academy of Sciences of the United States of America*, vol. 102, pp. 10451–10453, July 2005.

[2] A. C. Neto, F. Guinea, N. M. Peres, K. S. Novoselov, and A. K. Geim, “The electronic properties of graphene,” *Reviews of modern physics*, vol. 81, no. 1, p. 109, 2009.

[3] P. Miró, M. Audiffred, and T. Heine, “An atlas of two-dimensional materials,” *Chemical Society Reviews*, vol. 43, no. 18, pp. 6537–6554, 2014.

[4] G. R. Bhimanapati, Z. Lin, V. Meunier, Y. Jung, J. Cha, S. Das, D. Xiao, Y. Son, M. S. Strano, V. R. Cooper, *et al.*, “Recent advances in two-dimensional materials beyond graphene,” *ACS nano*, vol. 9, no. 12, pp. 11509–11539, 2015.

[5] N. Mounet *et al.*, “Two-dimensional materials from high-throughput computational exfoliation of experimentally known compounds,” *Nature nanotechnology*, vol. 13, no. 3, p. 246, 2018.

[6] S. Manzeli, D. Ovchinnikov, D. Pasquier, O. V. Yazyev, and A. Kis, “2d transition metal dichalcogenides,” *Nature Reviews Materials*, vol. 2, p. 17033, Aug. 2017.

[7] R. Huisman, R. De Jonge, C. Haas, and F. Jellinek, “Trigonal-prismatic coordination in solid compounds of transition metals,” *Journal of Solid State Chemistry*, vol. 3, no. 1, pp. 56–66, 1971.

[8] M. M. Ugeda *et al.*, “Characterization of collective ground states in single-layer nbse 2,” *Nature Physics*, vol. 12, no. 1, p. 92, 2016.

[9] B. Radisavljevic, A. Radenovic, J. Brivio, i. V. Giacometti, and A. Kis, “Single-layer mos$_2$ transistors,” *Nature nanotechnology*, vol. 6, no. 3, p. 147, 2011.

[10] Z. Y. Zhu, Y. C. Cheng, and U. Schwingenschlögl, “Giant spin-orbit-induced spin splitting in two-dimensional transition-metal dichalcogenide semiconductors,” *Phys. Rev. B*, vol. 84, p. 153402, Oct 2011.

[11] J. M. Lu, O. Zheliuk, I. Leermakers, N. F. Q. Yuan, U. Zeitler, K. T. Law, and J. T. Ye, "Evidence for two-dimensional ising superconductivity in gated mos$_2$," *Science*, vol. 350, pp. 1353–1357, Dec. 2015.

[12] A. Pulkin and O. V. Yazyev, "Spin- and valley-polarized transport across line defects in monolayer mos$_2$," *Phys. Rev. B*, vol. 93, p. 041419, Jan 2016.

[13] J. A. Wilson, F. J. Di Salvo, and S. Mahajan, "Charge-density waves in metallic, layered, transition-metal dichalcogenides," *Phys. Rev. Lett.*, vol. 32, pp. 882–885, Apr 1974.

[14] M. H. Whangbo and E. Canadell, "Analogies between the concepts of molecular chemistry and solid-state physics concerning structural instabilities. electronic origin of the structural modulations in layered transition metal dichalcogenides," *Journal of the American Chemical Society*, vol. 114, no. 24, pp. 9587–9600, 1992.

[15] X. Qian, J. Liu, L. Fu, and J. Li, "Quantum spin hall effect in two-dimensional transition metal dichalcogenides," *Science*, vol. 346, pp. 1344–1347, Dec. 2014.

[16] K. T. Law and P. A. Lee, "1t-tas$_2$ as a quantum spin liquid," *Proceedings of the National Academy of Sciences*, vol. 114, pp. 6996–7000, Mar. 2017.

[17] Y. Nakata, K. Sugawara, R. Shimizu, Y. Okada, P. Han, T. Hitosugi, K. Ueno, T. Sato, and T. Takahashi, "Monolayer $1T$-nbse$_2$ as a mott insulator," *NPG Asia Materials*, vol. 8, p. e321, Nov. 2016.

[18] F. J. Di Salvo, D. E. Moncton, and J. V. Waszczak, "Electronic properties and superlattice formation in the semimetal tise$_2$," *Phys. Rev. B*, vol. 14, pp. 4321–4328, Nov 1976.

[19] P. Chen, W. W. Pai, Y.-H. Chan, A. Takayama, C.-Z. Xu, A. Karn, S. Hasegawa, M.-Y. Chou, S.-K. Mo, A.-V. Fedorov, *et al.*, "Emergence of charge density waves and a pseudogap in single-layer tite$_2$," *Nature communications*, vol. 8, no. 1, p. 516, 2017.

[20] W. Kohn, "Excitonic phases," *Phys. Rev. Lett.*, vol. 19, pp. 439–442, Aug 1967.

[21] D. Jérome, T. M. Rice, and W. Kohn, "Excitonic insulator," *Phys. Rev.*, vol. 158, pp. 462–475, Jun 1967.

[22] R. E. Peierls, *Quantum theory of solids.* No. 23, Oxford University Press, 1955.

[23] F. Wilczek, "Particle physics and condensed matter: the saga continues," *Physica Scripta*, vol. 2016, no. T168, p. 014003, 2016.

[24] S. Coleman and E. Weinberg, "Radiative corrections as the origin of spontaneous symmetry breaking," *Phys. Rev. D*, vol. 7, pp. 1888–1910, Mar 1973.

[25] S.-K. Chan and V. Heine, "Spin density wave and soft phonon mode from nesting fermi surfaces," *Journal of Physics F: Metal Physics*, vol. 3, no. 4, p. 795, 1973.

[26] P. Hohenberg and W. Kohn, “Inhomogeneous electron gas,” *Phys. Rev.*, vol. 136, pp. B864–B871, Nov 1964.

[27] W. Kohn and L. J. Sham, “Self-consistent equations including exchange and correlation effects,” *Phys. Rev.*, vol. 140, pp. A1133–A1138, Nov 1965.

[28] D. M. Ceperley and B. J. Alder, “Ground state of the electron gas by a stochastic method,” *Phys. Rev. Lett.*, vol. 45, pp. 566–569, Aug 1980.

[29] J. P. Perdew, K. Burke, and M. Ernzerhof, “Generalized gradient approximation made simple,” *Physical Review Letters*, vol. 77, pp. 3865–3868, Oct. 1996.

[30] A. Seidl, A. Görling, P. Vogl, J. A. Majewski, and M. Levy, “Generalized kohn-sham schemes and the band-gap problem,” *Phys. Rev. B*, vol. 53, pp. 3764–3774, Feb 1996.

[31] C. Adamo and V. Barone, “Toward reliable density functional methods without adjustable parameters: The pbe0 model,” *The Journal of chemical physics*, vol. 110, no. 13, pp. 6158–6170, 1999.

[32] J. P. Perdew, M. Ernzerhof, and K. Burke, “Rationale for mixing exact exchange with density functional approximations,” *The Journal of chemical physics*, vol. 105, no. 22, pp. 9982–9985, 1996.

[33] M. A. L. Marques, J. Vidal, M. J. T. Oliveira, L. Reining, and S. Botti, “Density-based mixing parameter for hybrid functionals,” *Phys. Rev. B*, vol. 83, p. 035119, Jan 2011.

[34] J. H. Skone, M. Govoni, and G. Galli, “Self-consistent hybrid functional for condensed systems,” *Phys. Rev. B*, vol. 89, p. 195112, May 2014.

[35] J. Heyd, G. E. Scuseria, and M. Ernzerhof, “Hybrid functionals based on a screened coulomb potential,” *The Journal of chemical physics*, vol. 118, no. 18, pp. 8207–8215, 2003.

[36] A. V. Krukau, O. A. Vydrov, A. F. Izmaylov, and G. E. Scuseria, “Influence of the exchange screening parameter on the performance of screened hybrid functionals,” *The Journal of chemical physics*, vol. 125, no. 22, p. 224106, 2006.

[37] V. I. Anisimov, J. Zaanen, and O. K. Andersen, “Band theory and mott insulators: Hubbard u instead of stoner i,” *Physical Review B*, vol. 44, pp. 943–954, July 1991.

[38] B. Himmetoglu, A. Floris, S. De Gironcoli, and M. Cococcioni, “Hubbard-corrected dft energy functionals: The lda+ u description of correlated systems,” *International Journal of Quantum Chemistry*, vol. 114, no. 1, pp. 14–49, 2014.

[39] M. Cococcioni and S. de Gironcoli, “Linear response approach to the calculation of the effective interaction parameters in the LDA + U method,” *Physical Review B*, vol. 71, p. 035105, Jan. 2005.

[40] P. Giannozzi, S. Baroni, N. Bonini, M. Calandra, R. Car, C. Cavazzoni, D. Ceresoli, G. L. Chiarotti, M. Cococcioni, I. Dabo, *et al.*, “Quantum espresso: a modular and open-source software project for quantum simulations of materials,” *Journal of physics: Condensed matter*, vol. 21, no. 39, p. 395502, 2009.

[41] G. Kresse and J. Hafner, “Ab initio molecular dynamics for liquid metals,” *Phys. Rev. B*, vol. 47, pp. 558–561, Jan 1993.

[42] G. Kresse and J. Furthmüller, “Efficiency of ab-initio total energy calculations for metals and semiconductors using a plane-wave basis set,” *Computational materials science*, vol. 6, no. 1, pp. 15–50, 1996.

[43] G. Kresse and J. Furthmüller, “Efficient iterative schemes for ab initio total-energy calculations using a plane-wave basis set,” *Phys. Rev. B*, vol. 54, pp. 11169–11186, Oct 1996.

[44] D. R. Hamann, M. Schlüter, and C. Chiang, “Norm-conserving pseudopotentials,” *Phys. Rev. Lett.*, vol. 43, pp. 1494–1497, Nov 1979.

[45] D. Vanderbilt, “Soft self-consistent pseudopotentials in a generalized eigenvalue formalism,” *Physical Review B*, vol. 41, pp. 7892–7895, Apr. 1990.

[46] X. Gonze and C. Lee, “Dynamical matrices, born effective charges, dielectric permittivity tensors, and interatomic force constants from density-functional perturbation theory,” *Phys. Rev. B*, vol. 55, pp. 10355–10368, Apr 1997.

[47] S. Baroni, S. de Gironcoli, A. Dal Corso, and P. Giannozzi, “Phonons and related crystal properties from density-functional perturbation theory,” *Reviews of Modern Physics*, vol. 73, pp. 515–562, July 2001.

[48] C. A. Ullrich and Z.-h. Yang, *Excitons in Time-Dependent Density-Functional Theory*, pp. 185–217. Cham: Springer International Publishing, 2016.

[49] M. E. Casida, “Recent advances in density functional methods,” 1995.

[50] J. Paier, M. Marsman, and G. Kresse, “Dielectric properties and excitons for extended systems from hybrid functionals,” *Phys. Rev. B*, vol. 78, p. 121201, Sep 2008.

[51] M. Rohlfing and S. G. Louie, “Electron-hole excitations in semiconductors and insulators,” *Phys. Rev. Lett.*, vol. 81, pp. 2312–2315, Sep 1998.

[52] M. S. Hybertsen and S. G. Louie, “Electron correlation in semiconductors and insulators: Band gaps and quasiparticle energies,” *Phys. Rev. B*, vol. 34, pp. 5390–5413, Oct 1986.

[53] L. Hedin, “New method for calculating the one-particle green’s function with application to the electron-gas problem,” *Phys. Rev.*, vol. 139, pp. A796–A823, Aug 1965.

[54] D. Pasquier and O. V. Yazyev, “Crystal field, ligand field, and interorbital effects in two-dimensional transition metal dichalcogenides across the periodic table,” *arXiv preprint arXiv:1810.01302*, 2018.

[55] J. A. Wilson and A. Yoffe, “The transition metal dichalcogenides discussion and interpretation of the observed optical, electrical and structural properties,” *Advances in Physics*, vol. 18, no. 73, pp. 193–335, 1969.

[56] M. Chhowalla, H. S. Shin, G. Eda, L.-J. Li, K. P. Loh, and H. Zhang, “The chemistry of two-dimensional layered transition metal dichalcogenide nanosheets,” *Nature Chemistry*, vol. 5, p. 263, Apr. 2013.

[57] Q. H. Wang, K. Kalantar-Zadeh, A. Kis, J. N. Coleman, and M. S. Strano, “Electronics and optoelectronics of two-dimensional transition metal dichalcogenides,” *Nature nanotechnology*, vol. 7, no. 11, pp. 699–712, 2012.

[58] M. Kertesz and R. Hoffmann, “Octahedral vs. trigonal-prismatic coordination and clustering in transition-metal dichalcogenides,” *Journal of the American Chemical Society*, vol. 106, no. 12, pp. 3453–3460, 1984.

[59] K.-A. N. Duerloo, Y. Li, and E. J. Reed, “Structural phase transitions in two-dimensional mo-and w-dichalcogenide monolayers,” *Nature communications*, vol. 5, p. 4214, 2014.

[60] S. Tongay, H. Sahin, C. Ko, A. Luce, W. Fan, K. Liu, J. Zhou, Y.-S. Huang, C.-H. Ho, J. Yan, *et al.*, “Monolayer behaviour in bulk res 2 due to electronic and vibrational decoupling,” *Nature communications*, vol. 5, p. 3252, 2014.

[61] J.-H. Choi and S.-H. Jhi, “Origin of distorted 1t-phase res2: first-principles study,” *Journal of Physics: Condensed Matter*, vol. 30, no. 10, p. 105403, 2018.

[62] Y. Wang, Y. Li, and Z. Chen, “Not your familiar two dimensional transition metal disulfide: structural and electronic properties of the pds$_2$ monolayer,” *Journal of Materials Chemistry C*, vol. 3, no. 37, pp. 9603–9608, 2015.

[63] H. Yang, S. W. Kim, M. Chhowalla, and Y. H. Lee, “Structural and quantum-state phase transitions in van der waals layered materials,” *Nature Physics*, vol. 13, no. 10, p. 931, 2017.

[64] K. Santosh, C. Zhang, S. Hong, R. M. Wallace, and K. Cho, “Phase stability of transition metal dichalcogenide by competing ligand field stabilization and charge density wave,” *2D Materials*, vol. 2, no. 3, p. 035019, 2015.

[65] L. F. Mattheiss, “Band structures of transition-metal-dichalcogenide layer compounds,” *Phys. Rev. B*, vol. 8, pp. 3719–3740, Oct 1973.

[66] E. B. Isaacs and C. A. Marianetti, “Electronic correlations in monolayer vs$_2$,” *Phys. Rev. B*, vol. 94, p. 035120, Jul 2016.

[67] A. Scaramucci, J. Ammann, N. Spaldin, and C. Ederer, “Separating different contributions to the crystal-field parameters using wannier functions,” *Journal of Physics: Condensed Matter*, vol. 27, no. 17, p. 175503, 2015.

[68] N. Marzari, A. A. Mostofi, J. R. Yates, I. Souza, and D. Vanderbilt, “Maximally localized wannier functions: Theory and applications,” *Reviews of Modern Physics*, vol. 84, pp. 1419–1475, Oct. 2012.

[69] N. Marzari and D. Vanderbilt, “Maximally localized generalized wannier functions for composite energy bands,” *Physical Review B*, vol. 56, pp. 12847–12865, Nov. 1997.

[70] I. Souza, N. Marzari, and D. Vanderbilt, “Maximally localized wannier functions for entangled energy bands,” *Phys. Rev. B*, vol. 65, p. 035109, Dec 2001.

[71] D. R. Hamann, “Optimized norm-conserving vanderbilt pseudopotentials,” *Phys. Rev. B*, vol. 88, p. 085117, Aug 2013.

[72] P. Scherpelz, M. Govoni, I. Hamada, and G. Galli, “Implementation and validation of fully relativistic gw calculations: spin–orbit coupling in molecules, nanocrystals, and solids,” *Journal of chemical theory and computation*, vol. 12, no. 8, pp. 3523–3544, 2016.

[73] M. Schlipf and F. Gygi, “Optimization algorithm for the generation of oncv pseudopotentials,” *Computer Physics Communications*, vol. 196, pp. 36–44, 2015.

[74] http://www.quantum-simulation.org/potentials/sg15_oncv/.

[75] A. Dal Corso, “Pseudopotentials periodic table: From h to pu,” *Computational Materials Science*, vol. 95, pp. 337–350, Dec. 2014.

[76] https://dalcorso.github.io/pslibrary/.

[77] N. Marzari, D. Vanderbilt, A. De Vita, and M. C. Payne, “Thermal contraction and disordering of the al(110) surface,” *Physical Review Letters*, vol. 82, pp. 3296–3299, Apr. 1999.

[78] A. A. Mostofi, J. R. Yates, G. Pizzi, Y.-S. Lee, I. Souza, D. Vanderbilt, and N. Marzari, “An updated version of wannier90: A tool for obtaining maximally-localised wannier functions,” *Computer Physics Communications*, vol. 185, pp. 2309–2310, Aug. 2014.

[79] D. Sakabe, Z. Liu, K. Suenaga, K. Nakatsugawa, and S. Tanda, “Direct observation of mono-layer, bi-layer, and tri-layer charge density waves in 1t-tas$_2$ by transmission electron microscopy without a substrate,” *npj Quantum Materials*, vol. 2, no. 1, p. 22, 2017.

[80] C. E. Sanders, M. Dendzik, A. S. Ngankeu, A. Eich, A. Bruix, M. Bianchi, J. A. Miwa, B. Hammer, A. A. Khajetoorians, and P. Hofmann, “Crystalline and electronic structure of single-layer tas$_2$,” *Phys. Rev. B*, vol. 94, p. 081404, Aug 2016.

[81] F. J. Di Salvo and J. E. Graebner, “The low temperature electrical properties of 1t-tas$_2$,” *Solid State Communications*, vol. 23, pp. 825–828, Sept. 1977.

[82] B. Sipos, A. F. Kusmartseva, A. Akrap, H. Berger, L. Forró, and E. Tutiš, “From mott state to superconductivity in 1t-tas$_2$,” *Nature Materials*, vol. 7, p. 960, Dec. 2008.

[83] C. Chen, H.-S. Kim, A. S. Admasu, S.-W. Cheong, K. Haule, D. Vanderbilt, and W. Wu, "Trimer bonding states on the surface of transition-metal dichalcogenide tate2," *arXiv preprint arXiv:1807.02597*, 2018.

[84] X. Xi, Z. Wang, W. Zhao, J.-H. Park, K. T. Law, H. Berger, L. Forró, J. Shan, and K. F. Mak, "Ising pairing in superconducting nbse$_2$ atomic layers," *Nature Physics*, vol. 12, pp. 139–143, Feb. 2016.

[85] K. Sugawara, Y. Nakata, R. Shimizu, P. Han, T. Hitosugi, T. Sato, and T. Takahashi, "Unconventional charge-density-wave transition in monolayer 1t-tise$_2$," *ACS nano*, vol. 10, no. 1, pp. 1341–1345, 2015.

[86] J. A. Wilson, F. Di Salvo, and S. Mahajan, "Charge-density waves and superlattices in the metallic layered transition metal dichalcogenides," *Advances in Physics*, vol. 24, no. 2, pp. 117–201, 1975.

[87] K. Rossnagel, "On the origin of charge-density waves in select layered transition-metal dichalcogenides," *Journal of Physics: Condensed Matter*, vol. 23, no. 21, p. 213001, 2011.

[88] A. H. Castro Neto, "Charge density wave, superconductivity, and anomalous metallic behavior in 2d transition metal dichalcogenides," *Physical Review Letters*, vol. 86, pp. 4382–4385, May 2001.

[89] E. G. van Loon, M. Rösner, G. Schönhoff, M. I. Katsnelson, and T. O. Wehling, "Competing coulomb and electron-phonon interactions in nbs$_2$," *npj Quantum Materials*, vol. 3, no. 1, p. 32, 2018.

[90] F. Güller, V. L. Vildosola, and A. M. Llois, "Spin density wave instabilities in the nbs$_2$ monolayer," *Phys. Rev. B*, vol. 93, p. 094434, Mar 2016.

[91] M. Calandra, "Phonon-assisted magnetic mott-insulating state in the charge density wave phase of single-layer $1t$-nbse$_2$," *Phys. Rev. Lett.*, vol. 121, p. 026401, Jul 2018.

[92] J. B. Goodenough, "Band model for transition-metal chalcogenides having layer structures with occupied trigonal-bipyramidal sites," *Materials Research Bulletin*, vol. 3, no. 5, pp. 409–415, 1968.

[93] J. A. Wilson, F. J. D. Salvo, and S. Mahajan, "Charge-density waves and superlattices in the metallic layered transition metal dichalcogenides," *Advances in Physics*, vol. 24, pp. 117–201, Mar. 1975.

[94] J. C. Wildervanck and F. Jellinek, "The dichalcogenides of technetium and rhenium," *Journal of the Less Common Metals*, vol. 24, no. 1, pp. 73 – 81, 1971.

[95] M. D. Johannes and I. I. Mazin, "Fermi surface nesting and the origin of charge density waves in metals," *Physical Review B*, vol. 77, p. 165135, Apr. 2008.

[96] X. Zhu, Y. Cao, J. Zhang, E. W. Plummer, and J. Guo, “Classification of charge density waves based on their nature,” *Proceedings of the National Academy of Sciences*, vol. 112, pp. 2367–2371, Feb. 2015.

[97] S. Yi, Z. Zhang, and J.-H. Cho, “Coupling of charge, lattice, orbital, and spin degrees of freedom in charge density waves in $1t\text{tas}_2$,” *Phys. Rev. B*, vol. 97, p. 041413, Jan 2018.

[98] M. Calandra, I. I. Mazin, and F. Mauri, “Effect of dimensionality on the charge-density wave in few-layer $2H$-NbSe$_2$,” *Phys. Rev. B*, vol. 80, p. 241108, Dec 2009.

[99] Y. Ge and A. Y. Liu, “Effect of dimensionality and spin-orbit coupling on charge-density-wave transition in 2h-tase$_2$,” *Phys. Rev. B*, vol. 86, p. 104101, Sep 2012.

[100] F. Weber, S. Rosenkranz, J.-P. Castellan, R. Osborn, R. Hott, R. Heid, K.-P. Bohnen, T. Egami, A. H. Said, and D. Reznik, “Extended phonon collapse and the origin of the charge-density wave in $2h-\text{nbse}_2$,” *Phys. Rev. Lett.*, vol. 107, p. 107403, Sep 2011.

[101] X. Xi, L. Zhao, Z. Wang, H. Berger, L. Forró, J. Shan, and K. F. Mak, “Strongly enhanced charge-density-wave order in monolayer nbse 2,” *Nature nanotechnology*, vol. 10, no. 9, p. 765, 2015.

[102] J. Á. Silva-Guillén, P. Ordejón, F. Guinea, and E. Canadell, “Electronic structure of 2h-nbse2 single-layers in the cdw state,” *2D Materials*, vol. 3, no. 3, p. 035028, 2016.

[103] O. R. Albertini, A. Y. Liu, and M. Calandra, “Effect of electron doping on lattice instabilities in single-layer $1h-\text{tas}_2$,” *Phys. Rev. B*, vol. 95, p. 235121, Jun 2017.

[104] C. Battaglia, H. Cercellier, F. Clerc, L. Despont, M. G. Garnier, C. Koitzsch, P. Aebi, H. Berger, L. Forró, and C. Ambrosch-Draxl, “Fermi-surface-induced lattice distortion in Nbte$_2$,” *Phys. Rev. B*, vol. 72, p. 195114, Nov 2005.

[105] A. Y. Liu, “Electron-phonon coupling in compressed $1t$-tas$_2$: Stability and superconductivity from first principles,” *Phys. Rev. B*, vol. 79, p. 220515, Jun 2009.

[106] Y. Ge and A. Y. Liu, “First-principles investigation of the charge-density-wave instability in $1t$-tase$_2$,” *Phys. Rev. B*, vol. 82, p. 155133, Oct 2010.

[107] Q. Zhang, L.-Y. Gan, Y. Cheng, and U. Schwingenschlögl, “Spin polarization driven by a charge-density wave in monolayer $1t-\text{tas}_2$,” *Phys. Rev. B*, vol. 90, p. 081103, Aug 2014.

[108] Y. Yu, F. Yang, X. F. Lu, Y. J. Yan, Y.-H. Cho, L. Ma, X. Niu, S. Kim, Y.-W. Son, D. Feng, *et al.*, “Gate-tunable phase transitions in thin flakes of 1t-tas 2,” *Nature nanotechnology*, vol. 10, no. 3, p. 270, 2015.

[109] X. M. Chen, A. J. Miller, C. Nugroho, G. A. de la Peña, Y. I. Joe, A. Kogar, J. D. Brock, J. Geck, G. J. MacDougall, S. L. Cooper, E. Fradkin, D. J. Van Harlingen, and P. Abbamonte, “Influence of ti doping on the incommensurate charge density wave in $1t-\text{tas}_2$,” *Phys. Rev. B*, vol. 91, p. 245113, Jun 2015.

[110] D. F. Shao, R. C. Xiao, W. J. Lu, H. Y. Lv, J. Y. Li, X. B. Zhu, and Y. P. Sun, "Manipulating charge density waves in $1t-\mathrm{tas}_2$ by charge-carrier doping: A first-principles investigation," *Phys. Rev. B*, vol. 94, p. 125126, Sep 2016.

[111] D. C. Miller, S. D. Mahanti, and P. M. Duxbury, "Charge density wave states in tantalum dichalcogenides," *Phys. Rev. B*, vol. 97, p. 045133, Jan 2018.

[112] E. Kamil, J. Berges, G. Schönhoff, M. Rösner, M. Schüler, G. Sangiovanni, and T. Wehling, "Electronic structure of single layer 1t-nbse2: interplay of lattice distortions, non-local exchange, and mott–hubbard correlations," *Journal of Physics: Condensed Matter*, vol. 30, no. 32, p. 325601, 2018.

[113] D. Pasquier and O. V. Yazyev, "Charge density wave phase, mottness, and ferromagnetism in monolayer $1t-\mathrm{nbse}_2$," *Phys. Rev. B*, vol. 98, p. 045114, Jul 2018.

[114] Á. Pásztor, A. Scarfato, C. Barreteau, E. Giannini, and C. Renner, "Dimensional crossover of the charge density wave transition in thin exfoliated vse2," *2D Materials*, vol. 4, no. 4, p. 041005, 2017.

[115] D. Zhang, J. Ha, H. Baek, Y.-H. Chan, F. D. Natterer, A. F. Myers, J. D. Schumacher, W. G. Cullen, A. V. Davydov, Y. Kuk, M. Y. Chou, N. B. Zhitenev, and J. A. Stroscio, "Strain engineering a $4a \times \sqrt{3}a$ charge-density-wave phase in transition-metal dichalcogenide $1\mathrm{T}-\mathrm{VSe}_2$," *Phys. Rev. Materials*, vol. 1, p. 024005, Jul 2017.

[116] Y. Umemoto, K. Sugawara, Y. Nakata, T. Takahashi, and T. Sato, "Pseudogap, Fermi arc, and Peierls-insulating phase induced by 3d–2d crossover in monolayer VSe2," *Nano Research*, Sept. 2018.

[117] M. Mulazzi, A. Chainani, N. Katayama, R. Eguchi, M. Matsunami, H. Ohashi, Y. Senba, M. Nohara, M. Uchida, H. Takagi, and S. Shin, "Absence of nesting in the charge-density-wave system $1\mathrm{t}\text{-}\mathrm{vs}_2$ as seen by photoelectron spectroscopy," *Phys. Rev. B*, vol. 82, p. 075130, Aug 2010.

[118] D. H. Keum, S. Cho, J. H. Kim, D.-H. Choe, H.-J. Sung, M. Kan, H. Kang, J.-Y. Hwang, S. W. Kim, H. Yang, K. J. Chang, and Y. H. Lee, "Bandgap opening in few-layered monoclinic MoTe2," *Nature Physics*, vol. 11, p. 482, May 2015.

[119] S. N. Shirodkar and U. V. Waghmare, "Emergence of ferroelectricity at a metal-semiconductor transition in a $1t$ monolayer of mos_2," *Phys. Rev. Lett.*, vol. 112, p. 157601, Apr 2014.

[120] S. V. Streltsov and D. I. Khomskii, "Covalent bonds against magnetism in transition metal compounds," *Proceedings of the National Academy of Sciences*, vol. 113, no. 38, pp. 10491–10496, 2016.

[121] C. Heil, H. Sormann, L. Boeri, M. Aichhorn, and W. von der Linden, "Accurate bare susceptibilities from full-potential ab initio calculations," *Phys. Rev. B*, vol. 90, p. 115143, Sep 2014.

[122] F. J. Di Salvo, J. A. Wilson, B. G. Bagley, and J. V. Waszczak, "Effects of doping on charge-density waves in layer compounds," *Phys. Rev. B*, vol. 12, pp. 2220–2235, Sep 1975.

[123] O. R. Albertini, R. Zhao, R. L. McCann, S. Feng, M. Terrones, J. K. Freericks, J. A. Robinson, and A. Y. Liu, "Zone-center phonons of bulk, few-layer, and monolayer $1t-\mathrm{tas}_2$: Detection of commensurate charge density wave phase through raman scattering," *Phys. Rev. B*, vol. 93, p. 214109, Jun 2016.

[124] W. L. McMillan, "Landau theory of charge-density waves in transition-metal dichalcogenides," *Physical Review B*, vol. 12, pp. 1187–1196, Aug. 1975.

[125] W. L. McMillan, "Theory of discommensurations and the commensurate-incommensurate charge-density-wave phase transition," *Phys. Rev. B*, vol. 14, pp. 1496–1502, Aug 1976.

[126] A. A. Soluyanov, D. Gresch, Z. Wang, Q. Wu, M. Troyer, X. Dai, and B. A. Bernevig, "Type-ii weyl semimetals," *Nature*, vol. 527, p. 495, Nov. 2015.

[127] N. F. Q. Yuan, K. F. Mak, and K. Law, "Possible topological superconducting phases of mos_2," *Physical Review Letters*, vol. 113, p. 097001, Aug. 2014.

[128] Y. Saito, Y. Nakamura, M. S. Bahramy, Y. Kohama, J. Ye, Y. Kasahara, Y. Nakagawa, M. Onga, M. Tokunaga, T. Nojima, Y. Yanase, and Y. Iwasa, "Superconductivity protected by spin–valley locking in ion-gated mos_2," *Nature Physics*, vol. 12, p. 144, Feb. 2016.

[129] P. Darancet, A. J. Millis, and C. A. Marianetti, "Three-dimensional metallic and two-dimensional insulating behavior in octahedral tantalum dichalcogenides," *Physical Review B*, vol. 90, p. 045134, July 2014.

[130] T. Ritschel, J. Trinckauf, K. Koepernik, B. Büchner, M. v. Zimmermann, H. Berger, Y. I. Joe, P. Abbamonte, and J. Geck, "Orbital textures and charge density waves in transition metal dichalcogenides," *Nature Physics*, vol. 11, p. 328, Apr. 2015.

[131] A. Mielke, "Ferromagnetic ground states for the hubbard model on line graphs," *Journal of Physics A: Mathematical and General*, vol. 24, no. 2, p. L73, 1991.

[132] A. Mielke, "Exact ground states for the hubbard model on the kagome lattice," *Journal of Physics A: Mathematical and General*, vol. 25, no. 16, p. 4335, 1992.

[133] A. Mielke and H. Tasaki, "Ferromagnetism in the hubbard model," *Communications in Mathematical Physics*, vol. 158, pp. 341–371, Nov. 1993.

[134] H. Tasaki, "Ferromagnetism in the hubbard models with degenerate single-electron ground states," *Physical Review Letters*, vol. 69, pp. 1608–1611, Sept. 1992.

[135] H. Tasaki, "From nagaoka's ferromagnetism to flat-band ferromagnetism and beyond: An introduction to ferromagnetism in the hubbard model," *Progress of Theoretical Physics*, vol. 99, pp. 489–548, Apr. 1998.

[136] M. Ichimura, K. Kusakabe, S. Watanabe, and T. Onogi, “Flat-band ferromagnetism in extended δ-chain hubbard models,” *Physical Review B*, vol. 58, pp. 9595–9598, Oct. 1998.

[137] S. Watanabe, M. Ichimura, T. Onogi, Y. A. Ono, T. Hashizume, and Y. Wada, “Theoretical study of ga adsorbates around dangling-bond wires on an h-terminated si surface: Possibility of atomic-scale ferromagnets,” *Japanese Journal of Applied Physics*, vol. 36, p. L929, July 1997.

[138] K. Penc, H. Shiba, F. Mila, and T. Tsukagoshi, “Ferromagnetism in multiband hubbard models: From weak to strong coulomb repulsion,” *Physical Review B*, vol. 54, pp. 4056–4067, Aug. 1996.

[139] http://people.sissa.it/~dalcorso/pslibrary/index.html.

[140] A. Georges, G. Kotliar, W. Krauth, and M. J. Rozenberg, “Dynamical mean-field theory of strongly correlated fermion systems and the limit of infinite dimensions,” *Reviews of Modern Physics*, vol. 68, pp. 13–125, Jan. 1996.

[141] http://amulet-code.org/.

[142] E. Gull, A. J. Millis, A. I. Lichtenstein, A. N. Rubtsov, M. Troyer, and P. Werner, “Continuous-time monte carlo methods for quantum impurity models,” *Reviews of Modern Physics*, vol. 83, pp. 349–404, May 2011.

[143] M. Pizzochero and O. V. Yazyev, “Point defects in the $1T^{'}$ and $2h$ phases of single-layer mos$_2$: A comparative first-principles study,” *Phys. Rev. B*, vol. 96, p. 245402, Dec 2017.

[144] A. M. Woolley and G. Wexler, “Band structures and fermi surfaces for 1t-tas$_2$, 1t-tase$_2$ and 1t-vse$_2$,” *Journal of Physics C: Solid State Physics*, vol. 10, no. 14, p. 2601, 1977.

[145] M. Itoh, M. Tsuchiya, H. Tanaka, and K. Motoya, “Orbital ordering and local magnetic properties of mott-hubbard insulators ytio$_3$ and latio$_3$: Nmr study,” *Journal of the Physical Society of Japan*, vol. 68, no. 8, pp. 2783–2789, 1999.

[146] A. S. Erickson, S. Misra, G. J. Miller, R. R. Gupta, Z. Schlesinger, W. A. Harrison, J. M. Kim, and I. R. Fisher, “Ferromagnetism in the mott insulator ba$_2$naoso$_6$,” *Physical Review Letters*, vol. 99, p. 016404, July 2007.

[147] F. Pollmann, P. Fulde, and K. Shtengel, “Kinetic ferromagnetism on a kagome lattice,” *Physical Review Letters*, vol. 100, p. 136404, Apr. 2008.

[148] A. Tanaka and H. Ueda, “Stability of ferromagnetism in the hubbard model on the kagome lattice,” *Physical Review Letters*, vol. 90, p. 067204, Feb. 2003.

[149] R. Chisnell, J. Helton, D. Freedman, D. Singh, R. Bewley, D. Nocera, and Y. Lee, “Topological magnon bands in a kagome lattice ferromagnet,” *Physical Review Letters*, vol. 115, p. 147201, Sept. 2015.

[150] X.-L. Yu, D.-Y. Liu, Y.-M. Quan, J. Wu, H.-Q. Lin, K. Chang, and L.-J. Zou, "Electronic correlation effects and orbital density wave in the layered compound $1t$-tas$_2$," *Physical Review B*, vol. 96, p. 125138, Sept. 2017.

[151] A. S. Ngankeu, S. K. Mahatha, K. Guilloy, M. Bianchi, C. E. Sanders, K. Hanff, K. Rossnagel, J. A. Miwa, C. Breth Nielsen, M. Bremholm, and P. Hofmann, "Quasi-one-dimensional metallic band dispersion in the commensurate charge density wave of $1t$-tas$_2$," *Physical Review B*, vol. 96, p. 195147, Nov. 2017.

[152] A. Ribak, I. Silber, C. Baines, K. Chashka, Z. Salman, Y. Dagan, and A. Kanigel, "Gapless excitations in the ground state of $1t$-tas$_2$," *Physical Review B*, vol. 96, p. 195131, Nov. 2017.

[153] Y. Iqbal, W.-J. Hu, R. Thomale, D. Poilblanc, and F. Becca, "Spin liquid nature in the heisenberg $j_1 - j_2$ triangular antiferromagnet," *Physical Review B*, vol. 93, p. 144411, Apr. 2016.

[154] D. Pasquier and O. V. Yazyev, "Excitonic effects in two-dimensional tise _2 from hybrid density functional theory," *arXiv preprint arXiv:1805.11560*, 2018.

[155] D. Ovchinnikov, F. Gargiulo, A. Allain, D. J. Pasquier, D. Dumcenco, C.-H. Ho, O. V. Yazyev, and A. Kis, "Disorder engineering and conductivity dome in res 2 with electrolyte gating," *Nature communications*, vol. 7, p. 12391, 2016.

[156] P. Chen, Y.-H. Chan, X.-Y. Fang, Y. Zhang, M.-Y. Chou, S.-K. Mo, Z. Hussain, A.-V. Fedorov, and T.-C. Chiang, "Charge density wave transition in single-layer titanium diselenide," *Nature communications*, vol. 6, p. 8943, 2015.

[157] P. Chen, Y.-H. Chan, M.-H. Wong, X.-Y. Fang, M. Y. Chou, S.-K. Mo, Z. Hussain, A.-V. Fedorov, and T.-C. Chiang, "Dimensional effects on the charge density waves in ultrathin films of tise2," *Nano Letters*, vol. 16, no. 10, pp. 6331–6336, 2016.

[158] J. A. Wilson, "Concerning the semimetallic characters of tis2 and tise2," *Solid State Communications*, vol. 22, no. 9, pp. 551–553, 1977.

[159] J. Wilson, "Modelling the contrasting semimetallic characters of tis2 and tise2," *physica status solidi (b)*, vol. 86, no. 1, pp. 11–36, 1978.

[160] K. Rossnagel, L. Kipp, and M. Skibowski, "Charge-density-wave phase transition in $1t-$ tise$_2$: excitonic insulator versus band-type jahn-teller mechanism," *Phys. Rev. B*, vol. 65, p. 235101, May 2002.

[161] H. Cercellier, C. Monney, F. Clerc, C. Battaglia, L. Despont, M. G. Garnier, H. Beck, P. Aebi, L. Patthey, H. Berger, and L. Forró, "Evidence for an excitonic insulator phase in $1t-$tise$_2$," *Phys. Rev. Lett.*, vol. 99, p. 146403, Oct 2007.

[162] J. van Wezel, P. Nahai-Williamson, and S. S. Saxena, "Exciton-phonon-driven charge density wave in tise$_2$," *Phys. Rev. B*, vol. 81, p. 165109, Apr 2010.

[163] C. Monney, G. Monney, P. Aebi, and H. Beck, “Electron–hole instability in 1t-tise2,” *New Journal of Physics*, vol. 14, no. 7, p. 075026, 2012.

[164] T. Kaneko, Y. Ohta, and S. Yunoki, “Exciton-phonon cooperative mechanism of the triple-q charge-density-wave and antiferroelectric electron polarization in tise$_2$,” *Phys. Rev. B*, vol. 97, p. 155131, Apr 2018.

[165] D. Varsano, S. Sorella, D. Sangalli, M. Barborini, S. Corni, E. Molinari, and M. Rontani, “Carbon nanotubes as excitonic insulators,” *Nature Communications*, vol. 8, no. 1, p. 1461, 2017.

[166] Y. Wakisaka, T. Sudayama, K. Takubo, T. Mizokawa, M. Arita, H. Namatame, M. Taniguchi, N. Katayama, M. Nohara, and H. Takagi, “Excitonic insulator state in ta$_2$nise$_5$ probed by photoemission spectroscopy,” *Phys. Rev. Lett.*, vol. 103, p. 026402, Jul 2009.

[167] T. Kaneko, T. Toriyama, T. Konishi, and Y. Ohta, “Orthorhombic-to-monoclinic phase transition of ta$_2$nise$_5$ induced by the bose-einstein condensation of excitons,” *Phys. Rev. B*, vol. 87, p. 035121, Jan 2013.

[168] C. Monney, C. Battaglia, H. Cercellier, P. Aebi, and H. Beck, “Exciton condensation driving the periodic lattice distortion of $1t-$tise$_2$,” *Phys. Rev. Lett.*, vol. 106, p. 106404, Mar 2011.

[169] R. Fernandes, A. Chubukov, and J. Schmalian, “What drives nematic order in iron-based superconductors?,” *Nature physics*, vol. 10, no. 2, p. 97, 2014.

[170] S. Vig, A. Kogar, M. Mitrano, A. A. Husain, V. Mishra, M. S. Rak, L. Venema, P. D. Johnson, G. D. Gu, E. Fradkin, M. R. Norman, and P. Abbamonte, “Measurement of the dynamic charge response of materials using low-energy, momentum-resolved electron energy-loss spectroscopy (M-EELS),” *SciPost Phys.*, vol. 3, p. 026, 2017.

[171] A. Kogar, M. S. Rak, S. Vig, A. A. Husain, F. Flicker, Y. I. Joe, L. Venema, G. J. MacDougall, T. C. Chiang, E. Fradkin, J. van Wezel, and P. Abbamonte, “Signatures of exciton condensation in a transition metal dichalcogenide,” *Science*, vol. 358, no. 6368, pp. 1314–1317, 2017.

[172] M. Calandra and F. Mauri, “Charge-density wave and superconducting dome in tise$_2$ from electron-phonon interaction,” *Physical Review Letters*, vol. 106, p. 196406, May 2011.

[173] R. Bianco, M. Calandra, and F. Mauri, “Electronic and vibrational properties of tise$_2$ in the charge-density-wave phase from first principles,” *Phys. Rev. B*, vol. 92, p. 094107, Sep 2015.

[174] M. Hellgren, J. Baima, R. Bianco, M. Calandra, F. Mauri, and L. Wirtz, “Critical role of the exchange interaction for the electronic structure and charge-density-wave formation in tise$_2$,” *Phys. Rev. Lett.*, vol. 119, p. 176401, Oct 2017.

[175] S. Albrecht, L. Reining, R. Del Sole, and G. Onida, “Ab initio calculation of excitonic effects in the optical spectra of semiconductors,” *Phys. Rev. Lett.*, vol. 80, pp. 4510–4513, May 1998.

[176] P. E. Blöchl, "Projector augmented-wave method," *Physical review B*, vol. 50, no. 24, p. 17953, 1994.

[177] X.-Y. Fang, H. Hong, P. Chen, and T.-C. Chiang, "X-ray study of the charge-density-wave transition in single-layer TiSe_2," *Phys. Rev. B*, vol. 95, p. 201409, May 2017.

[178] P. Haas, F. Tran, and P. Blaha, "Calculation of the lattice constant of solids with semilocal functionals," *Phys. Rev. B*, vol. 79, p. 085104, Feb 2009.

[179] B. Singh, C.-H. Hsu, W.-F. Tsai, V. M. Pereira, and H. Lin, "Stable charge density wave phase in a $1t$–tise_2 monolayer," *Phys. Rev. B*, vol. 95, p. 245136, Jun 2017.

[180] M. J. Wei, W. J. Lu, R. C. Xiao, H. Y. Lv, P. Tong, W. H. Song, and Y. P. Sun, "Manipulating charge density wave order in monolayer $1t - \mathrm{tise}_2$ by strain and charge doping: A first-principles investigation," *Phys. Rev. B*, vol. 96, p. 165404, Oct 2017.

[181] I. B. Guster, E. Canadell, M. Pruneda, and P. Ordejon, "First principles analysis of the cdw instability of single-layer 1t-tise 2 and its evolution with charge carrier density," *2D Materials*, 2018.

[182] K. Dolui and S. Sanvito, "Dimensionality-driven phonon softening and incipient charge density wave instability in tis2," *EPL (Europhysics Letters)*, vol. 115, no. 4, p. 47001, 2016.

[183] S. Suga, C. Tusche, Y.-i. Matsushita, M. Ellguth, A. Irizawa, and J. Kirschner, "Momentum microscopy of the layered semiconductor tis2 and ni intercalated ni1/3tis2," *New Journal of Physics*, vol. 17, no. 8, p. 083010, 2015.

[184] G. Kresse and D. Joubert, "From ultrasoft pseudopotentials to the projector augmented-wave method," *Phys. Rev. B*, vol. 59, pp. 1758–1775, Jan 1999.

[185] S. Kolekar, M. Bonilla, Y. Ma, H. C. Diaz, and M. Batzill, "Layer-and substrate-dependent charge density wave criticality in 1t–tise2," *2D Materials*, vol. 5, no. 1, p. 015006, 2017.

[186] P. E. Blöchl, O. Jepsen, and O. K. Andersen, "Improved tetrahedron method for brillouin-zone integrations," *Phys. Rev. B*, vol. 49, pp. 16223–16233, Jun 1994.

[187] F. H. da Jornada, D. Y. Qiu, and S. G. Louie, "Nonuniform sampling schemes of the brillouin zone for many-electron perturbation-theory calculations in reduced dimensionality," *Phys. Rev. B*, vol. 95, p. 035109, Jan 2017.

Diego Pasquier

Personal data

Diego José Pasquier, 28 years old, swiss & belgian, single.

Education

2012–2014	**Master of Science Msc**, *EPFL*, Lausanne, Physics.
2009–2012	**Bachelor of Science Bsc**, *EPFL*, Lausanne, Physics.
2004–2007	**Maturité gymnasiale**, *Lycée Denis-de-Rougemont*, Neuchâtel, Biology and Chemistry.

Master thesis

Title	*Running couplings in the νMSM*
Supervisor	Dr. Alexander Monin
Description	Studied the critical behavior of the Neutrino Minimal Standard Model (νMSM), an extension of the Standard Model of particle physics with three light right-handed neutrinos and a scalar dilaton field.

Doctoral thesis

Title	*Crystalline and correlated phases in two-dimensional transition metal dichalcogenides*
Supervisor	Prof. Oleg V. Yazyev
Description	Studied various aspects of the electronic structure of two-dimensional transition metal dichalcogenides using a combination of *ab initio* and many-body techniques.

Experience

Vocational

12/2014–now	**PhD Candidate in Physics**, EPFL, Chair of Computational Condensed Matter Physics.
03/2014–05/2014	**Research Assistant**, EPFL, Laboratory of Particle Physics and Cosmology.
07/2009–08/2009	**Intern**, *EM Microelectronic*, Marin, R&D Management.

Student jobs

2011–2013	**Teaching Assistant**, EPFL.
2009–2011	**Pollster**, *Jeko Market Research*. Performed customer satisfaction surveys in supermarkets.

Volunteering

09/2016-06/2017	**Press attaché**, *Balélec Festival*, Contacts with the medias, writing of promotional texts, press conference management.

Languages

French	Mother tongue
English	Professional working proficiency, two months of courses in the UK (2009).
German	Very good, one month of courses in Germany (2010).

Computer skills

Experience with Microsoft office, Matlab, Mathematica, Latex, C++, Fortran, Bash, and *ab inito* simulation packages (in particular Quantum ESPRESSO and VASP).

List of conference contributions

[1] "Understanding transition metal dichalcogenides from first-principles calculations", talk given at the Graphene Flagship Work Package 1 Workshop "Advances in the synthesis of graphene", January 18-22, 2016, Fuerteventura, Spain.

[2] "Periodic lattice distortion and electronic structure of monolayer ReS$_2$", poster presentation at the 18th International Workshop on Computational Physics and Materials Science: Total Energy and Force Methods,, January 12-14, 2017, Trieste, Italy.

[3] "Lattice instabilities in metallic transition metal dichalcogenides", talk given at the Joint Annual Meeting of the Swiss Physical Society and Austrian Physical Society, August 21-25, 2017, Geneva, Switzerland.

[4] "Understanding the charge density wave in monolayer NbSe$_2$ from first principles", talk given at the APS March Meeting 2018, March 5-9, 2018, Los Angeles, USA.

[5] "Excitonic effects in two-dimensional TiSe$_2$ from hybrid density functional theory", poster presentation at the 2DSPM conference, June 25-29, 2018, San Sebastian, Spain.

List of publications

[1] Ovchinnikov, D., Gargiulo, F., Allain, A.,**Pasquier, D.**, Dumcenco, D., Ching-Hwa, H., Yazyev, OV., Kis, A. "Disorder engineering and conductivity dome in ReS$_2$ with electrolyte gating". Nature communications 7, 12391 (2016).

[2] Manzeli, S., Ovchinnikov, D., **Pasquier, D.**, Yazyev, OV, Kis, A. "2D transition metal dichalcogenides". Nature Reviews Materials 2 (8), 17033 (2017).

[3] **Pasquier, D.**, Yazyev, OV. "Charge density wave phase, Mottness, and ferromagnetism in monolayer $1T$-NbSe$_2$". Physical Review B 98 (4), 045114 (2018).

[4] **Pasquier, D.**, Yazyev, OV. "Excitonic effects in two-dimensional TiSe$_2$ from hybrid density functional theory". Accepted in Physical Review B. arXiv preprint arXiv:1805.11560.

[5] **Pasquier, D.**, Yazyev, OV. "Crystal field, ligand field, and interorbital effects in two-dimensional transition metal dichalcogenides across the periodic table". Submitted to 2D materials. arXiv preprint arXiv:1810.01302.

[6] **Pasquier, D.**, Yazyev, OV. "A unified picture for lattice instabilities in metallic octahedral transition metal dichalcogenides". To be submitted

Ce document a été imprimé au Centre d’impression EPFL,
imprimerie climatiquement neutre, certifiée myClimate.